THE NORDIC CONCRETE FEDERATION 1/2016 PUBLICATION NO. 54

Nordic Concrete Research

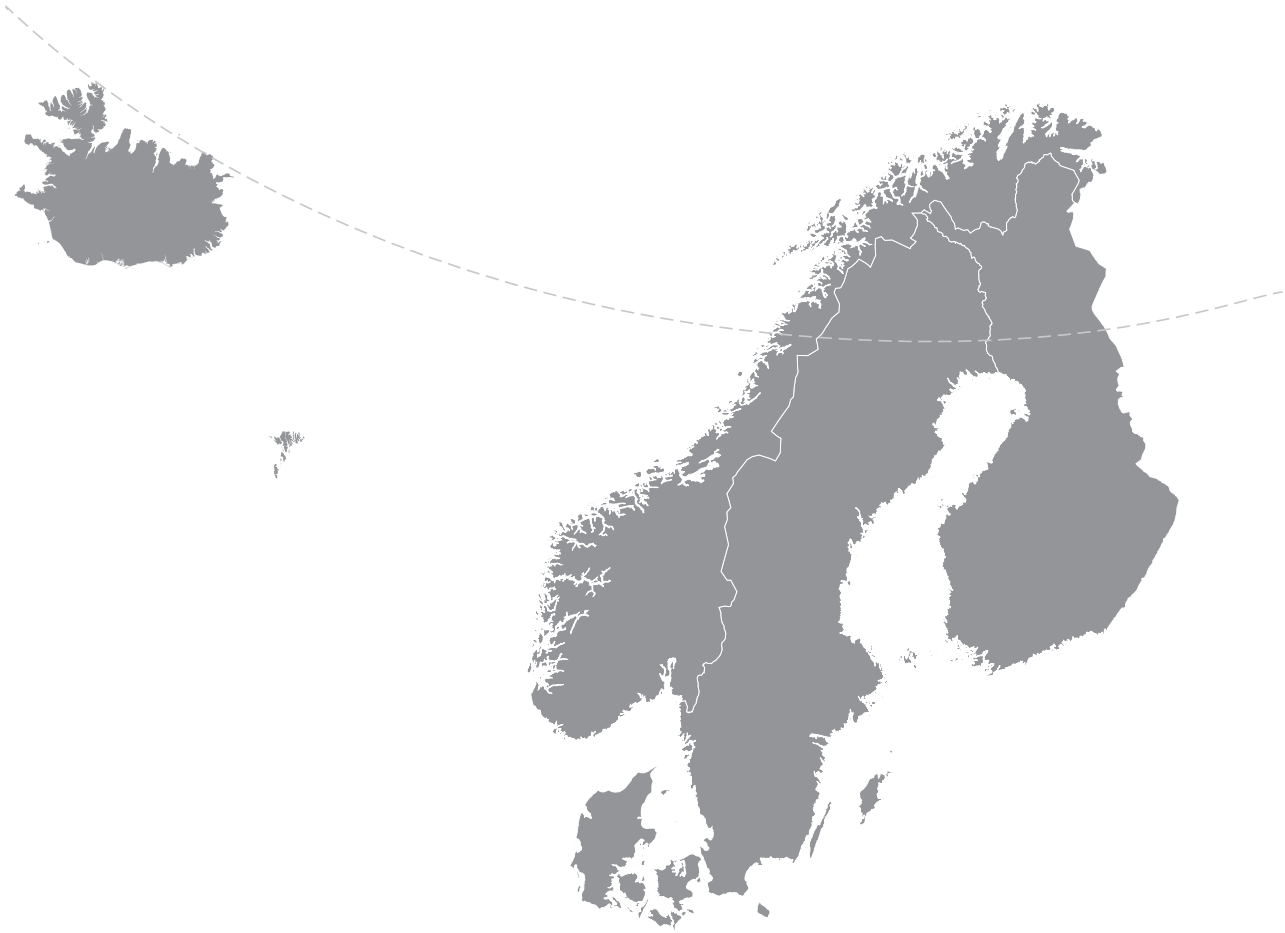

Nordic Concrete Federation

PUBLICATION NO. 54 1/2016

NORDIC CONCRETE RESEARCH

EDITED BY
THE NORDIC CONCRETE FEDERATION

CONCRETE ASSOCIATIONS OF: DENMARK
FINLAND
ICELAND
NORWAY
SWEDEN

PUBLISHER: NORSK BETONGFORENING
POSTBOKS 2312, SOLLI
N - 0201 OSLO
NORWAY

BREVIK/OSLO, MAY 2016

Preface

Since 1982, *Nordic Concrete Research* has been the leading scientific journal concerning concrete research in the five Nordic countries, e.g., Denmark, Finland, Iceland, Norway and Sweden. The content of Nordic Concrete Research reflects the major trends in the concrete research.

Since 1982, well over 400 papers have been published in the journal. Since 1994 the abstracts and from 1998 both the abstracts and the full papers can be found on the Nordic Concrete Federation's homepage: www.nordicconcrete.net. The journal thus contributes to dissemination of Nordic concrete research, both within the Nordic countries and internationally. The abstracts and papers can be downloaded for free. Proceedings from miniseminars and the proceedings from the Research Symposia are about to be published on the homepage as well.

Nordic Concrete Research is published by the Nordic Concrete Federation which also organizes the Nordic Concrete Research Symposia, a continuous series of conferences since its first onset in 1953 in Stockholm.

The XXIII Nordic Concrete Research Symposium will be organised in Aalborg, Denmark, on August 21rst – 23rd, 2017. We do look forward to seeing you there.

The high quality of the papers in NCR is ensured by the group of reviewers. Most papers are assessed by two reviewers, selected according to their individual expertise.

Currently we are exploring the possibility to have NCR published by a larger international publisher, in order increase the number of readers, and to have NCR accepted by international scientific databases. More information will be published on our homepage in due time.

Since 1975, in the range of 80 Nordic Miniseminars were organized. It is the experience of the Research Council of the Nordic Concrete Federation, that these Miniseminars have a substantial influence on concrete research in the Nordic countries. In some cases, the information gathered during such Miniseminars has also been used as Nordic input to CEN activities.

Brevik/Oslo, May 2016

Terje F. Rønning
Temporary editor, Nordic Concrete Research

PUBLICATION NO. 54 1/2016

CONTENTS

Designing concrete durability by coupling limit states of corrosion initiation and corrosion induced cracking of concrete cover

Miguel Ferreira
M.Sc, Ph.D.
VTT Technical Research Institute of Finland Ltd.
Kemistintie 3, P.O. Box 1000
FIN-02044, Espoo, Finland
miguel.ferreira@vtt.fi

Edgar Bohner
M.Sc, Dr. -Ing.
VTT Technical Research Institute of Finland Ltd.
Kemistintie 3, P.O. Box 1000
FIN-02044, Espoo, Finland
edgar.bohner@vtt.fi

Olli Saarela
M.Sc, Ph.D.
VTT Technical Research Institute of Finland Ltd.
Kemistintie 3, P.O. Box 1000
FIN-02044, Espoo, Finland
olli.saarela@vtt.fi

ABSTRACT

The successful durability design of reinforced concrete structures requires models capable of reliably describing both mechanisms of damage and its progression over time. In a chloride laden environment, most models used typically disregard the actual damage, i.e. the corrosion of the reinforcing steel. Common service life design practice only considers the end of the initiation phase of the degradation process as a critical limit state. In this paper, a holistic approach is presented that couples models used for determining the time to depassivation and the time to cover cracking as a result of reinforcement corrosion in a single limit state calculation.

Key words: Corrosion, cracking, service life, deterioration, modelling, concrete cover, chloride ingress, serviceability limit state.

1. INTRODUCTION

Time-dependent reliability analyses provides valuable support to the decision making process, whether for design, or for defining maintenance and repair strategies [1]. The service life prediction of deteriorating structures is affected by the uncertainties associated with material

properties, mechanical and environmental loads, damage occurrence and propagation models [2]. Therefore, estimation of service life requires probabilistic models and methods to account for the uncertainties that govern the deterioration processes. The service life design of reinforced concrete structures requires material models capable of reliably describing both mechanisms of damage and the general progression of damage over time. However, most models that are currently being used only capture the process of carbonation and chloride penetration into the uncracked concrete that is at the initial phase of degradation. Typically, these models disregard the actual damage, i.e. the corrosion of the reinforcing steel. As a result, the service life design established to date only considers the end of the initiation phase of the degradation process, i.e. the onset of damage (time of depassivation or onset of corrosion) as a critical limit state. The corrosion of the reinforcement and its consequences, i.e. the crack formation and spalling of concrete, are not considered, which may lead to a substantially shorter estimated service life of the structures. There are two distinct phases the in corrosion induced deterioration process of concrete.

The first phase (initiation) is defined as the time necessary for chloride ions to reach a critical concentration at the depth of the reinforcement to cause its depassivation. Typically diffusion controls the process. This instant is defined as corrosion initiation. The second phase (propagation) is defined as the period of time that follows the initiation of corrosion. It can be separated in different deterioration phases, of which the first is cracking of concrete cover. Typically corrosion rate controls the process at the outset. After the appearance of the first crack, the continuous volume expansion due to rust formation as a consequence of the proceeding corrosion leads to crack propagation resulting in the spalling of the concrete cover. In practice, it has been observed that time dependent reliability models do not consider the causational relationship between serviceability limit states, dealing with each limit state independently. As an example, corrosion initiation and propagation are usually dealt with independently, ignoring the dependency between them. Commonly the propagation phase is ignored, i.e. considered to be on the safe side (conservative approach). This might stem from the lack of models, and confidence in models for this phase. As a consequence, design decisions based upon independent time-dependent reliability models will not produce optimal outcomes. Comprehensive investigations were recently undertaken on the depassivation of steel reinforcement and on crack formation in concrete which have resulted in an analytical model for corrosion-induced cracking occurring in the surface zones of structural components [3].

An attempt to bridge this gap is made with a basic methodology for the probabilistic determination of service life, combining both corrosion initiation and propagation phase models is proposed. The approach takes into account the time dependency of the individual phenomena, and the relationship between both phases. The quantitative prediction of the time to cracking is needed in the development of a holistic deterioration model for the prediction of service life. A probabilistic methodology is presented based on theoretical physical models for corrosion initiation and time-to-cracking, and the causational relationship between them, i.e. time-to-cracking depends on the time to corrosion initiation. Based on the methodology, it is demonstrated how the models influence the estimated time to corrosion cracking considering both deterioration mechanisms involved. This approach helps to improve the prediction of durability for new or to define optimal repair strategies for existing concrete structures. The time from corrosion initiation to cracking of the concrete cover (time-to-cracking), is a critical period for modelling the time to repair, rehabilitate, and replace reinforced concrete structures.

This paper presents a probabilistic design procedure which combines the calculation of two independent limit states for concrete deterioration: chloride induced corrosion initiation, and

corrosion induced cracking of concrete. By combining the limit states, the outcome of the service life calculation is the probability of time to corrosion induced cracking, at any time starting after construction.

2. RELIABILITY ANALYSIS

2.1 Basic reliability analysis

In general, engineering design consists of proportioning the elements of a reinforced concrete structure (RCS) so that it satisfies various criteria of performance, safety, serviceability, and durability under various loadings. A reliability analysis can be used to calculate the probability of failure of a limit state at any instant in time during the RCS's service life. The objective of durability design is to keep the probability of failure throughout the service life period below a certain requirement that depends on the consequences of failure. The limit state defines the conditions beyond which a specified requirement for a structure (or component) is no longer met for a certain degree of reliability [4]. Limit states are represented by the limit state equations, generally of the form $g(R,S) = 0$. A limit state violation (or failure) occurs when an undesirable condition for the structure is reached. The probability of occurrence of a limit state violation is a numerical measure of the chances of its occurrence, based on long term observations or subjective estimates.

The basic reliability problem considers only one load effect S resisted by one resistance R. Both R and S are described by known probability density functions (PDF), $f_R(r)$ and $f_S(s)$ respectively, where any uncertainty concerning a variable is explicitly taken into account. For convenience, it is considered R and S are not functions of time. If R and S have known PDF's $f_R(r)$ and $f_S(s)$ respectively, and are expressed in the same units, then

$$p_f = P(R - S \le 0) \quad \text{or} \quad P\{g(R,S) \le 0\} \tag{1}$$

where $g(x)$ is termed the limit state function, and the probability of failure is synonymous to the probability of limit state violation. The probability of failure of the joint (bivariate) density $f_{RS}(r,s)$ is given by

$$p_f = P(R - S \le 0) = \iint_D f_{RS}(r,s)\,dr\,ds \tag{2}$$

If R and S are independent, then

$$f_{RS}(r,s) = f_R(r).f_S(s) \tag{3}$$

which leads to

$$p_f = P(R - S \le 0) = \int_{-\infty}^{\infty}\int_{-\infty}^{s \ge r} f_R(r).f_S(s)\,dr\,ds \tag{4}$$

For a random variable X, the cumulative distribution function is given by

$$F_X(x) = P(X \le x) = \int_{-\infty}^{x} f_X(y)\,dy \tag{5}$$

If R and S are independent, and if $x \le y$, the solution of the probability of failure for bivariate

density functions can be written in a single integral form known as the convolution integral:

$$p_f = P(R - S \le 0) = \int_{-\infty}^{\infty} F_R(x).f_S(x)dx \quad (6)$$

$F_R(x)$ is the probability $R \le x$ of the probability that the actual resistance R of the member is less than some value x, representing failure. The term $f_S(x)$ represents the probability that the load effect S acting on the element has a value between x and $x + \Delta x$ in the limit as $\Delta x \to 0$. By calculating the integral over all x, the total failure probability is obtained.

A reliability analysis can be performed by numerical integration, Monte Carlo simulation, or using approximate methods such as First Order and Second Order Reliability Methods (FORM/ SORM). The numerical integration was not preferred in this case because of the large dimension and the complexity of this problem. The reliability analysis in this study was performed using Monte Carlo simulation. Even for the computing of small probabilities, the development of variance reduction techniques such as importance sampling [5], and the evolution of computing power has reduced dramatically this once time consuming process. The theoretical description of this method is given in many references [6, 7].

2.2 Reliability analysis – combination of two limit states

A methodology is presented which contributes to the development of reliability-based approaches for the durability design and service life prediction of RCS that combines the probabilistic determination of two limit states (corrosion initiation and corrosion induced cracking) in a single analysis, thus removing the need for one of the limit states. By combining initiation with propagation until cracking, the combined service life covers the period from $t = 0$ until the time for the first crack with a width of a minimum of 0.05 mm to appear on the surface of the concrete. The combination includes both the processes described in Sections 3.2 and 3.3. Assuming that corrosion is initiated at some time τ, for cracking to take place at time t, the corrosion process has a duration of τ-t. Consequently, the combined probability distribution of the time of cracking is

$$f_{i,p}(t) = \int_{-\infty}^{\infty} f_p(t - \tau \,|\, T_i = \tau)\; f_i(\tau)\, d\tau \quad (7)$$

where $f_{i,p}$ = probability of failure; $f_p(t)$ = PDF of the propagation model; and $f_i(t)$ = PDF of the initiation model.

The start of corrosion propagation process depends on the corrosion initiation process, however the mechanisms that describe each of these processes are independent of each other. Therefore the modelling and computation of this distribution can be simplified by replacing the conditional PDF with corresponding marginal probability distribution,

$$f_{i,p}(t) \approx \int_{-\infty}^{\infty} f_p(t - \tau)\; f_i(\tau)\, d\tau \quad (8)$$

The model assumes chloride ingress starts at the time of construction ($t = 0$), and that the corrosion process starts when chloride has reached a critical threshold value at the depth of the reinforcement. Consequently,

$$f_p(t) = f_i(t) = 0 \quad \forall \ t < 0 \tag{9}$$

allowing the integration interval to be shortened. For $t \geq 0$

$$f_{i,\,p}(t) \approx \int_0^t f_p(t-\tau)\ f_i(\tau)\, d\tau \tag{10}$$

A consequence of this approach is that there is no need to establish a limit state requirement for corrosion initiation, and another for cracking. By combining the calculations, only one requirement for the outcome of both needs be defined. Furthermore, the uncertainties related to both processes, as modelled in the PDF's, are properly combined.

3. DETERIORATION MODELS

A reliability analysis begins with the formulation of a limit state function, which represents the performance of a structure or an element, in terms of a number of basic random variables. The model parameters are characterised by PDFs. Even the uncertainties associated with the model and the tests used should typically be considered. It is an assumption that the models for corrosion initiation and propagation are sufficiently validated in order to provide realistic and representative results. Conformity is checked by verifying that the specified reliability is unsurpassed in the verification of the limit state function over the service life of the structure.

The limit state function for time to corrosion initiation is defined by:

$$g_i(x,t) > 0 \Leftrightarrow C_{crit} - C(x,t) > 0 \tag{11}$$

where $g_i\ (x,t)$ = limit state function for corrosion initiation; C_{crit} = critical chloride content leading to depassivation [%/weight of cement or concrete]; and $C(x,t)$ = chloride concentration at depth x and time t [%/weight of cement or concrete]; and described in section 3.1

The limit state function for time to corrosion induced concrete cracking is given by:

$$g_p(x,t) > 0 \Leftrightarrow \Delta r_{crack}(t) - \Delta r_{corr}(t_{corr}) > 0 \tag{12}$$

where $g_p\ (x,t)$ = limit state function for corrosion induced concrete cracking; Δr_{corr} = increase of rebar radius due to corrosion [mm]; Δr_{crack} = critical increase of rebar radius due to corrosion at time of cracking [mm]; t_{corr} = time of corrosion [years]; and described in section 3.3.

3.1 Limit state requirements

Designers must define the criteria for which the limit state is evaluated. There is still considerable debate as to what are the appropriate values for durability related limit states. With regards to reinforcement corrosion, this is in part due to the difficulty in practice to define a precise instant when corrosion actually starts. Values based on experience or set by conventions are required. When defining the requirement for probability of failure – *pf* (or reliability index – β), the criteria that should be taken into account are: the type of limit state (initiation of deterioration, SLS – serviceability limit state or ULS – ultimate limit state); the service life for new structures or reference period for existing structures; the consequences of failure; and, the cost of safety measures. Typical values suggested for structural design for pf/β are for a period of 50 years $10^{-1}/1.28$ for a serviceability limit states, and $\approx 10^{-4}/3.72$ for ultimate limit states [8].

In the fib Model Code for Service Life Design [9], β = 1.3 is presented as a "recommended minimum value" for exposure class XS independent of the RC of the structure. According to the LNEC E-465 [10], the reliability index varies according to the RC from 1.2 to 2.0 for the RC1 and RC3 class, respectively. These β–values correspond to failure probabilities of approximately 12 % and 2 %, respectively. There is yet no consensus as to which should be the appropriate values for the reliability index, when considering limit states associated with durability [11,12].

3.2 Time to corrosion initiation

The model is based on the fib Model Code for Service Life Design [8] approach, which is based on the classical solution of Fick's second law with semi-infinite boundary and constant surface concentration. This model includes a time dependent apparent diffusion coefficient.

$$C(x,t) = C_0 + (C_S - C_0) \cdot \left(1 - erf \frac{c}{2\sqrt{D_{ap} \cdot t}}\right) \tag{13}$$

$$D_{ap} = D_0 \cdot \exp\left(be\left(\frac{1}{T_{ref}} - \frac{1}{T_{real}}\right)\right) \cdot k_t \cdot \left(\frac{t_0}{t}\right)^{\alpha} \tag{14}$$

where C_0 = initial chloride concentration in the concrete [%/weight of cement or concrete]; C_S = surface chloride concentration [%/weight of cement or concrete]; c = cover depth [mm]; D_{ap} = apparent diffusion coefficient [m^2/s]; D_0 = diffusion coefficient at t_0 [m^2/s]; α = ageing factor of diffusion coefficient [-]; t_0 = reference time [years]; t = life time [years]; T_{real} = temperature of the water/air in contact with concrete [K]; T_{ref} = reference temperature [K]; be = Arrhenius Slope [-]; kt = transfer parameter [-].

Although widely used, the model has not been calibrated for periods longer than 30 years and has several limitations and sources of uncertainty [11]. Equation (13) provides an estimate of the chloride profile for a specific period of exposure time. It is applicable for 1-D situations, and not suitable for small columns and beams, especially in the regions near the edges. The model also includes a number of implicit assumptions: exposure to chloride starts at $t = 0$, i.e. immediately after casting; C_s is constant over time; and D_{ap} varies with time and temperature only, until $t = \infty$ according to Eq.(14).

3.3 Time from corrosion initiation to concrete cracking

In order to describe the action S, which represents the propagation of corrosion, the increase of reinforcement bar (rebar) radius Δr_{corr} has to be defined. This increase is dependent on the time of corrosion and results from the reduction of the reinforcement bar radius due to corrosion in combination with the expansion of the occurred corrosion products (Eq. 15). The reduction of the rebar radius is based on the corrosion rate $\dot{x}_{corr}$. The corrosion rate can be either determined experimentally or it can be calculated by means of models, such as that of Osterminski & Schießl [13]. The expansion factor, also known as volume ratio λ, is calculated by the quotient of the volume of rust and the volume of the steel [14].

$$\Delta r_{corr}(t_{corr}) = t_{corr} \cdot \dot{x}_{corr}(t_{corr}) \cdot (\lambda - 1) - d_{por}(t_{corr}) \tag{15}$$

where Δr_{corr} = increase of rebar radius due to corrosion [mm]; $\dot{x}_{corr}$ = corrosion rate [mm/a]; λ = volume ratio [-]; d_{por} = function to take account of rust migration into concrete pores [mm].

Experimental investigations have shown that the initial radius increase of the corroding rebar is weakened by the migration of corrosion products into the surrounding voids and pores of the concrete [14 - 17]. This results in a time delay of the development of corrosion-induced stresses. Stress levels that are able to cause concrete cracking occur not until a certain saturation of the pores in the transition zone around the steel surface has taken place. By means of a continuous function (Eq. 16), which was derived based on physical considerations; the migration of rust into the concrete pores can be considered as:

$$d_{por}(t_{corr}) = p \cdot d_{tz} \cdot \tanh\left(\frac{\dot{x}_{corr}(t_{corr}) \cdot (\lambda - 1)}{p \cdot d_{tz}} \cdot t_{corr} \right) \tag{16}$$

where p = porosity of the transition zone accessible for corrosion products [-], valid $0 \leq p < 1$; d_{tz} = thickness of the transition zone accessible for corrosion products [mm].

The action S (increase of rebar radius due to corrosion) encounters a resistance R that derives from the concrete surrounding the rebar. It can be defined as the critical increase of rebar radius due to corrosion at the time of cracking (see Eq. 17). This threshold value depends on concrete age, concrete properties, size and shape of rebar and concrete cover thickness. Its derivation is based on the linear elastic theory assuming linear viscoelastic behaviour of the concrete [3]:

$$\Delta r_{crack}(t) = \frac{f_{ct}(t)}{E_{c,eff,D}} \cdot \frac{d_s + 2c(1 + c/d_s)(1+\nu)}{1 + \left(\frac{3d_s + 6c}{3d_s + 4c} \right)^2} \cdot k_{nonlin} \cdot k_{local} \cdot k_{\mu} \tag{17}$$

where Δr_{crack} = critical increase of rebar radius due to corrosion at time of cracking [mm]; t = concrete age [a]; f_{ct} = tensile strength of concrete [MPa]; $E_{c,eff,D}$ = effective modulus of elasticity of concrete (influence of creep, relaxation and degradation, [18] [MPa]; ν = Poisson's ratio of concrete [-]; d_s = rebar diameter [mm]; c = concrete cover [mm]; k_{nonlin} = factor for consideration of plasticity and cracking of concrete [-]; k_{local} = factor for consideration of a localisation of corrosion (pitting corrosion) [-]; k_{μ} = factor for consideration of percentage of reinforcement [-].

The model assumes that the corrosion instantly appears as uniform corrosion, covering the entire circumference of the reinforcement bar. A distinct pitting corrosion can be taken into account by assigning a value to the factor k_{local}. The complex time-dependent stress-induced deformation behaviour of concrete and its characteristic tension softening during cracking have a significant influence on the duration of the deterioration process. They are considered based on simplifying or adjunct functions, as e.g. the effective modulus of elasticity for concrete creep or the factor k_{nonlin} for taking into account the quasi-brittle cracking behaviour of concrete. For a detailed discussion of Eq. (15) to (17) and further information on the factors k_{nonlin}, k_{local} and k_{μ} including the development of the model based on elastic theory for a thick-wall cylinder and its verification with experiments, see [3].

4. RELIABILITY ANALYSIS - EXAMPLE

4.1 Parameter distribution and values

In the following example, a hypothetical semi-infinite reinforced concrete wall located in a XS3 environment (tidal/splash zone) according to the EN 206-1 [19] is considered. This scenario enables the use of a 1-D analysis and diffusion being the main form of chloride transport in the concrete (convection zone not considered in this study).

To illustrate the procedure described in Section 2.2, service life calculations have been performed considering two distinct concrete qualities: a CEM I 42.5 N with w/b ratio 0.50, and a CEM III/A 42.5 R with w/b ratio 0.55. Both concretes have similar mechanical performance, but differ significantly from a chloride ingress perspective, where CEM III out performs CEM I. For each parameter, distribution type and values used are presented in Table 1 for the corrosion initiation model. For the corrosion propagation model, three distinct corrosion rates were chosen to simulate varying speeds of corrosion: 5.0 μA/cm^2, 1.0 μA/cm^2 and 0.5 μA/cm^2. Corrosion rate is defined by a lognormal distribution (CoV = 0.3) with varying average values of 0.0525 mm/year, 0.0105 mm/year and 0.00525 mm/year, respectively. The remaining parameters are presented in Table 1.

Table 1 – Parameter values/distributions for time to corrosion initiation, and time to concrete cracking

Param.	Units	CEM I	CEM III
C_{crit}	%/wt.c	B[0.65, 0.13, 0.2, 2]	
C_0	%/wt.c	N[0.10, 0.005]	
C_S	%/wt.c	LN[2.0, 0.60]	
c	mm	LN[55.0, 6.25]	
$D_{RCM,0}$	10^{-12} ·m^2/s	LN[12.0,4.8]	LN[3.0,1.25]
k_t	–	C[1.0]	
b_e	K	N[4800, 500]	
T_{ref}	°C	C[20.0]	
T_{real}	°C	N[18.3, 1.55]	
α	–	B[0.3, 0.03, 0.0, 1.0]	B[0.45,0.045, 0.0, 1.0]
t_0	years	C[0.0767]	
Δc	mm	N[3.87, 0.71]	
T_e	days	C[14]	
T_n	years	C[10]	C[12]

Param.	Units	CEM I	CEM III
λ	–	C[2.1]	
p	–	N[0.14, 0.02]	N[0.16, 0.02]
d_{tz}	mm	LN[0.18,0.05]	LN[0.20,0.05]
d_s	mm	C[20.0]	
c	mm	LN[55.0, 10.0]	
$f_{ct}(t)$	MPa	N[3.10,0.31]	N[2.90,0.29]
E_c	MPa	N[29300, 2000]	N[28300, 2000]
ν	–	C[0.20]	
k_{nonlin}	–	C[2.3]	
k_{local}	–	C[0.70]	
k_μ	–	C[1.0]	
D	–	C[0.0]	
φ	–	C[0.70]	
ρ	–	C[0.80]	

Distribution types: LN – lognormal; N –Normal; B – Beta; C - Constant

4.2 Results

The calculation of the limit states for both initiation and propagation models individually were performed with a direct Monte Carlo simulation based on 10^4 determinations for each time step. The results are presented in Figure 1 for CEM I type concrete, and in Figure 2 for CEM III type concrete, for all three corrosion rates, representing fast, moderate and moderately slow corrosion.

The probability density function in Equation 10 was computed with trapezoidal numerical quadrature, as described by [20]. The service life obtained by combining the two individual service life calculations depends on both the quality of concrete and the corrosion rate. However, it is clear that the quality of concrete, mostly determining the time to corrosion initiation, dominates as it is the precursor for the corrosion propagation phase.

Assuming a defined probability for the limit state failure for corrosion initiation, it is normal to expect that the probability for the limit state failure for corrosion propagation should be lower since the consequences are more severe, and already damage inducing. The combination of both limit states should then be judged by the requirement for the second limit state since it is the phenomenon being observed, i.e. first cracking. However, due to lack of understanding and consensus as to what criteria should be used for these limit states, and for the purpose of demonstrating this methodology, an identical value of 10% is assumed for the limit state for corrosion propagation, and the coupled limit state for the sake of the following analyses.

The service life obtained for the initiation model is 4.1 years and 37.8 years, for CEM I and CEM III concrete, respectively. This means that, based on the model used and the parameters chosen, it took 4.1 years (CEM I) for the probability, that the chloride content at the depth of the reinforcement was greater than the critical chloride content, to exceed 10 %. The service lives obtained for the propagation models varied between 0.8 years and 8.2 years for CEM I concrete, and between 0.9 years and 8.8 years for CEM III concrete, for the chosen corrosion rates. This means that, for the CEM I concrete and based on the model used and the parameters chosen, it took between 0.8 years and 8.2 years for the probability, that a crack with a width of 0.05 mm had appeared on the concrete surface due to reinforcement corrosion, to exceed 10 %. The effect of corrosion rate is clearly seen in Figs. 1 and 2, where for the moderately slow corrosion (0.5 $\mu A/cm^2$) the coupled service life is extended approximately by 12 – 15 years when compared to the initiation service life, for CEM I and CEM III concretes, respectively. In the case of fast corrosion (5.0 $\mu A/cm^2$), the increase in service life is less than 2 years for both concrete types. This result shows how the rate of corrosion is a crucial parameter to consider when determining the service life of a reinforced concrete structure. In situations where fast corrosion can be expected (poor concrete quality and/or aggressive environment), the propagation model does not extend the initiation phase model service life significantly. However, when slower corrosion rates are expected, this can impact positively the service life by extending significantly the initiation phase model service life. In Table 2, the values for each service life calculation are presented.

These results show that, when coupling corrosion initiation and corrosion propagation, the corrosion rate has a significant influence in the extension of the service life. Cairns & Law [21] suggest that the limit state for propagation could be identical to that of the initiation because the appearance of the first crack does not affect the mechanical performance of the reinforced

concrete structures. In this case, a combination of limit state would always result in an extension of the service life of the reinforced concrete structures.

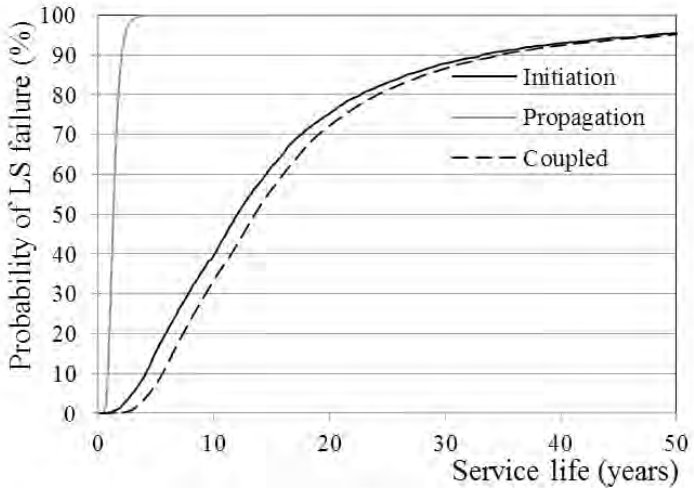

(a)

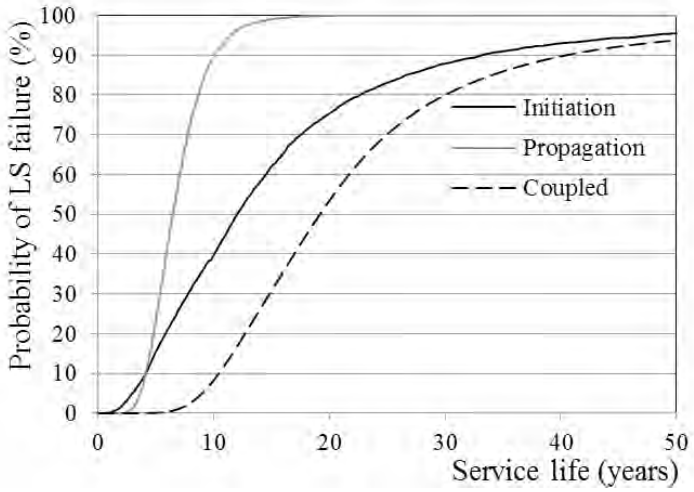

(b)

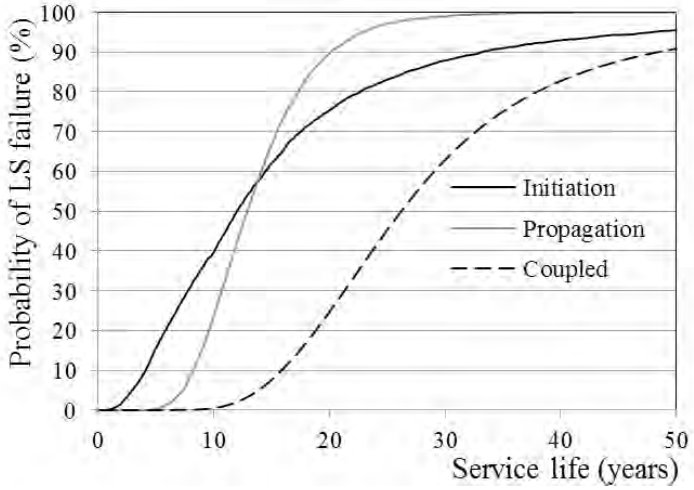

(c)

Figure 1 – Probability of limit state failure for corrosion initiation, corrosion propagation, and coupled corrosion for concrete produced with CEM I cement, and for varying corrosion rates: (a) 0.0525 mm/year, (b) 0.0105 mm/year, and (c) 0.00525 mm/year.

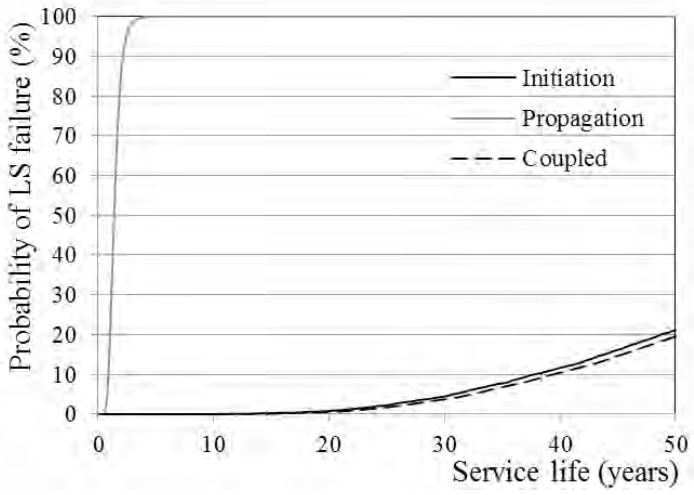

(a)

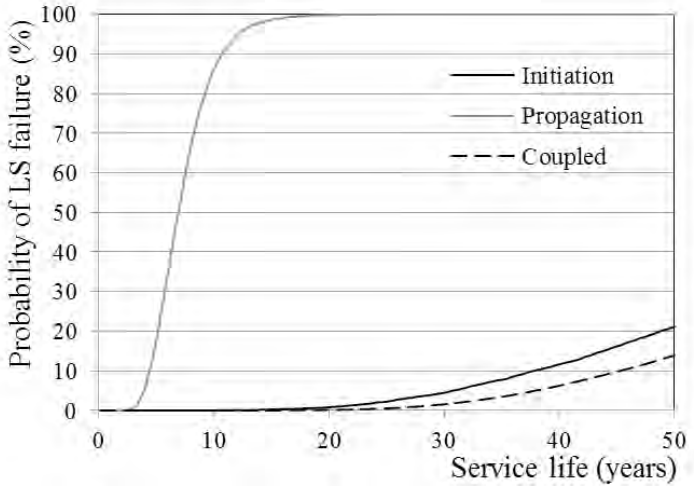

(b)

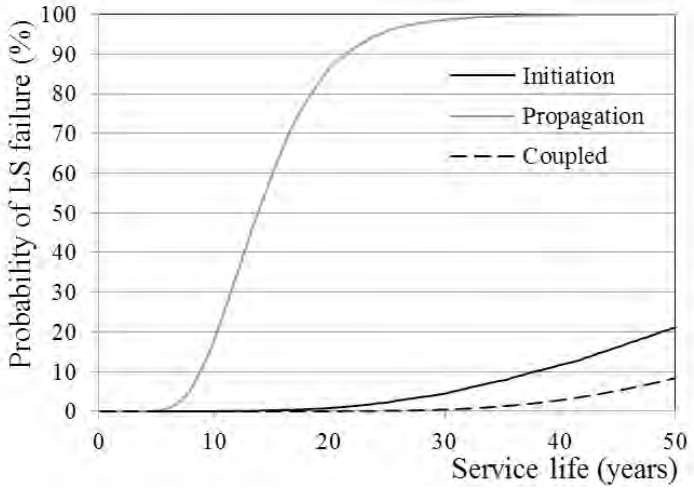

(c)

Figure 1 – Probability of limit state failure for corrosion initiation, corrosion propagation, and coupled corrosion for concrete produced with CEM III cement, and for varying corrosion rates: (a) 0.0525 mm/year, (b) 0.0105 mm/year, and (c) 0.00525 mm/year.

Table 2 – Time (years) until the criteria of 10% has been exceeded for the initiation, propagation and coupled limit state calculations.

CEM I	Fast	Medium	Slow
Initiation	4.1	4.1	4.1
Propagation	0.8	4.1	8.2
Coupled	5.6	10.5	15.9
SL extension	1.5	6.4	11.8

CEM III	Fast	Medium	Slow
Initiation	37.8	37.8	37.8
Propagation	0.9	4.4	8.8
Coupled	39.5	45.3	52.1
SL extension	1.7	7.5	14.3

With regards to the criteria chosen for the limit state, while assumed constant in this analysis, it must be mentioned that there is currently not enough background information to understand the consequences of certain values, and while many values are being put forward based on those used in structural design, they do not necessarily represent adequately the complexity of the deterioration mechanism and the economic consequences of limit state failure. The choice of limit state requirement is still relatively subjective.

5. CONCLUSIONS

This paper presents a probabilistic design procedure which combines the calculation of two independent limit states for concrete deterioration: chloride induced corrosion initiation and corrosion induced cover cracking of concrete. By combining these two limit states, the outcome of the service life calculation is the probability of time to corrosion induced cracking, at any time starting after construction. The design procedure is exemplified with two qualities of concrete (CEM I and CEM III) and three corrosion rates (slow, moderate and moderately slow). This study quantifies the impact that the propagation phase can have on the entire design service life of a RCS.

While in the past propagation models have had limitations (empirical nature, assumptions, simplifications, difficult handling, etc.), which call into question the outcome of the modelling, now the certainty behind the modelling is renewed. This is based on a new analytical time-to-cracking model [3] that allows for a realistic and quantitative description as well as a reliable prediction of the evolution of the damage process.

Simulation results show that the corrosion rate is a major factor to consider when determining the service life of a reinforced concrete structure. In situations where fast corrosion can be expected, either due to poor concrete quality and/or an aggressive environment, the propagation model, when coupled to the initiation model, does not extend the service life calculation significantly (< 2 years for the cases studied). However, when moderately slow corrosion rates are expected, this can impact positively the service life calculation by extending significantly the initiation phase model service life (up to almost 15 years for the given example).

The difficulty in this analysis resides in the definition of the limit state requirement (reliability index or probability of limit state failure). There is currently not enough background information to understand the consequences of certain values, and while many values are being put forward based on those used in structural design they do not necessarily represent adequately the complexity of the deterioration mechanism and the economic consequences of limit state failure.

This research has shown the benefit of using a coupled limit state analysis until the time to first corrosion induced crack to appear. The coupled limit state is of interest especially to the owners

of reinforced concrete structures. Joint consideration of corrosion initiation and propagation describes the damaging mechanism more realistically and facilitates an extension of the service life of the structures. More accurate assessment of the performance capacity of the reinforced concrete structures allows better optimised resource management.

REFERENCES

1. Stewart, M.G., Rosowsky, D.V., Dimitri, V.V., 2001, Reliability-based bridge assessment using risk-ranking decision analysis. Structural Safety 23 397–405.
2. Kim, S., Frangopol, D.M., Soliman, M. 2013. Generalized Probabilistic Framework for Optimum Inspection and Maintenance Planning. J. Struct. Eng. 139. pp. 435-447
3. Bohner, E. 2013. Concrete cracking due to reinforcement corrosion. Doctoral Dissertation, Karlsruhe Institute of Technology (KIT)
4. ISO/FDIS 16204:2012 Durability – Service life design of concrete structures. ISO. p 40.
5. Thoft-Christensen P, Baker M.J. 1982. Structural reliability theory and its applications. Springer-Verlag: Berlin, Heidelberg
6. Rubinstein, R.Y. 1981. Simulation and monte carlo method. John Wiley & Sons, New York.
7. CSEP. Introduction to Monte Carlo methods. Computational Science Projects, ORNL. 1995.
8. EN 1990:2002. Eurocode - Basis of structural design. CEN, Brussels.
9. fib Bulletin 34. 2006. Model Code for Service Life Design. International Federation for Structural Concrete, 206 p.
10. LNEC E 465:2007. Betões. Metodologia para estimar as propriedades de desempenho betão que permitem satisfazer a vida útil de projecto de estruturas de betão armado ou pré-esforçado sob as exposições ambientais XC e XS.. LNEC Laboratório Nacional de Engenharia Civil, Lisboa. p 24.
11. Gulikers, J. 2006. Critical issues in the interpretation of results of probabilistic service life calculations. in International RILEM Workshop on Integral Service Life Modelling of Concrete Structures. Univ. Minho, Guimarães, Portugal, ISBN 972-99179-2-2. 195-204.
12. Ferreira, R.M., Gulikers, J. 2008. Critical considerations on the assessment of the durability (serviceability) limit state of reinforced concrete structures. Pro.11th DBMC, Istanbul, 11-14 May. 1425-1432.
13. Osterminski, K., Schießl, P., 2011. Full probabilistic modelling of reinforcement corrosion: An approach to durability design. Final report of subproject D of the DFG research unit 537 “Modelling reinforcement corrosion”, , Centrum Baustoffe und Materialprüfung, Technische Universität München, 2011.
14. Bohner, E., Müller, H. S. 2012. Analytical prediction model for concrete cover cracking due to reinforcement corrosion. In: Life-Cycle and Sustainability of Civil Infrastructure Systems, Strauss, Frangopol und Bergmeister (ed.), Taylor and Francis Group, London, p. 442-448
15. Allan, M. L. 1995. Probability of corrosion induced cracking in reinforced concrete. In: Cement and Concrete Research 25, No. 6, pp. 1179-1190
16. Liu, Y., Weyers, R. 1998. Modeling the time-to-corrosion cracking in chloride contaminated reinforced concrete structures. In: ACI Materials Journal 95, No. 6, pp. 675-681
17. Pantazopoulou, S. J., Papoulia, K. D. 2001, Modeling cover-cracking due to reinforcement corrosion in RC structures. In: Journal of Engineering Mechanics 127, No. 4
18. Müller, H. S., Kvitsel, V., 2002. Creep and shrinkage of concrete. Basics of the new

standard DIN 1045 and approaches to building practise. In: Beton- und Stahlbetonbau. 97-1. 209-19.
19. EN 206-1:2000. Concrete. Specification, performance, production and conformity. CEN, Brussels.
20. Stoer, J., Bulirsch, R. 1980. Introduction to numerical analysis. Springer-Verlag: Berlin.
21. Cairns, J., Law, D., 2003. Prediction of the ultimate limit state of degradation of concrete structures. ILCDES 2003: Integrated Lifetime Engineering of Buildings and Civil Infrastructures. Rotterdam. 6p.

Chemical changes of cement pastes due to the effect of combined carbonation and chloride penetration

Fahim Al-Neshawy
D.Sc (Tech.)
Aalto University, School of Engineering
Department of Civil and Structural Engineering, Espoo
P.O.Box 12100
FIN-00076 Aalto, Finland
E-mail: fahim.al-neshawy@aalto.fi

ABSTRACT

Carbonation of concrete is often the cause of corrosion of steel reinforcement, which is actually one of the main causes for the degradation of concrete structures. The degradation might be more significant in the case of chloride penetration. Carbon dioxide (CO_2) in the air can penetrate into the concrete; dissolve in the pore solution, and react with calcium hydroxide, leading to water formation and calcium carbonate precipitation. Carbonation is a diffusion based phenomenon, where the carbonation front moves inwards at a rate proportional to square root of time. The rate of reaction of hardened cement pastes with CO_2 is known to depend strongly on the water cement ratio (w/c) of concrete, mixture composition, pore structure, temperature and curing conditions of concrete and its internal humidity.

When concrete is in contact with a chloride solution, chloride ions diffuse in the pore solution. They appear in concrete both as free Cl-ions (meaning water-soluble ions) in the pore interstitial solution and as chemically bound component of hydrate phases (e.g., Friedel's salt $Ca_2Al(OH)_6Cl•2H_2O$]), as well as physically adsorbed on CSH. Free chloride ions are the most dangerous due to their capacity to diffuse towards the steel bars

The objective of this paper is to determine the relationship between the chemical changes of hardened cement pastes and accelerated carbonation using different CO_2 concentrations with the presence of chloride ions. The chemical changes of the cement pastes were analyzed using X-Ray diffractometry and thermal analysis.

According to the results of the XRD-analysis all the sample pastes were partly amorphous and, thus, contained only limited amounts of crystalline compounds. The thermal decomposition of the paste samples exposed with sodium chloride NaCl was somewhat different from the behaviour of the other paste samples.

Key words: cement paste, carbonation, chloride, X-Ray diffractometry, thermal analysis (TG/DTA).

INTRODUCTION

Carbonation and chloride attacks are two main factors initiating corrosion of reinforcement in concrete structures. In normal circumstances when the carbon dioxide or sufficient chloride (i.e. critical chloride concentration) reaches the reinforced steel, the depassivation of the steel occurs and the steel reinforcement starts to corrode.

Carbon dioxide (CO_2) in the air can penetrate into the concrete; dissolve in the pore solution, and react with calcium hydroxide, leading to water formation and calcium carbonate precipitation. The carbonation is a diffusion based phenomenon, where the carbonation front moves inwards the concrete at a rate proportional to the square root of time. The rate of the reaction of the hardened cement pastes with CO_2 is known to depend strongly on the w/c of concrete, mixture composition, pore structure, temperature and curing conditions of concrete and its internal humidity. [1]

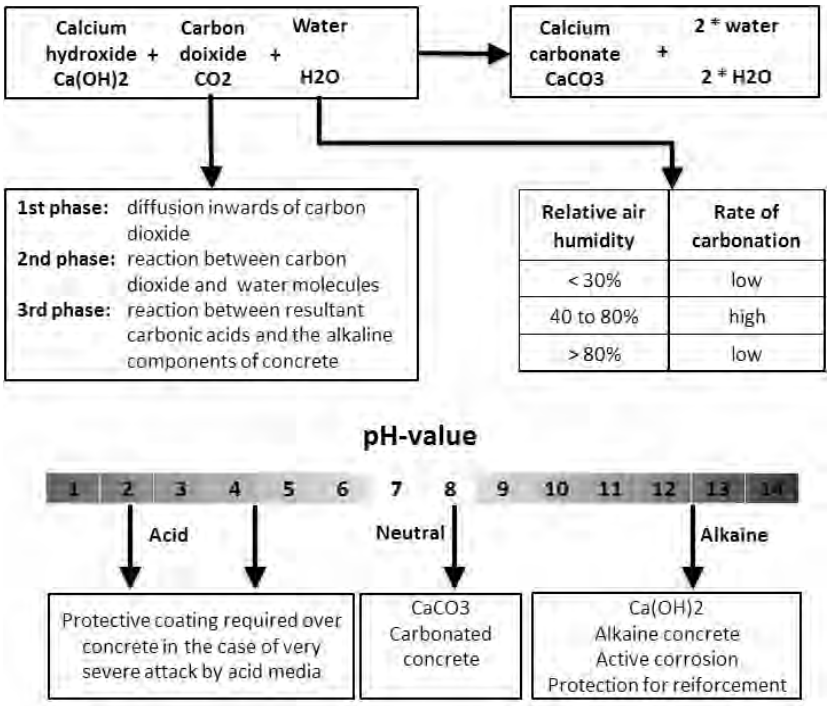

Figure 1. Schematic diagram showing the carbonation process on concrete.

Carbonation of hydrated cement compounds, i.e. essentially calcium hydroxide ($Ca(OH)_2$) and calcium silicate hydrate (C-S-H) is a chemical reaction of neutralisation of bases by an acid, the carbon dioxide in the air, which can be represented by the simple equations (1) and (2):

$$Ca(OH)_2 + CO_2 \rightarrow CaCO_3 + H_2O \quad (1)$$

$$\text{C-S-H (high C/S)} + CO_2 \rightarrow CaCO_3 + \text{C-S-H (low C/S)} + H_2O \quad (2)$$

These reactions take place in solution and the reactants have to dissolve before reacting. The solubility of calcium hydroxide is reduced by sodium and potassium hydroxides. These reactions induce a reduction of the pH of the pore solution. The normal pH-value of concrete is above 13 and the pH-value of fully carbonated concrete is below 9. Once the carbonation

process reaches the reinforcement, and the pH-value drops below 13 the passive “film” on the steel bars will deteriorate and corrosion will initiate. [2]

When concrete is in contact with a chloride solution, chloride ions diffuse in the pore solution. They appear in concrete both as free Cl^- ions (meaning water-soluble ions) in the pore interstitial solution and as chemically bound component of hydrate phases (e.g., Friedel’s salt $Ca_2Al(OH)_6Cl \cdot 2H_2O$]). Free chloride ions are the most dangerous because of their capacity to diffuse towards the steel bars [3].The penetration of chloride ion in concrete is accelerated when carbonation is interacted. This can be explained by the growing diffusivity of chloride ion caused by increased concentration gradient of chloride ion due to the crystallization of Friedel’s salt in the carbonated zone. [4]. Chlorides can also physically adsorb on the high surface of CSH.

The aim of this study was to get laboratory testing data on the effect of chloride penetration on carbonation and to determine the relationship between the chemical changes of the hardened cement pastes and accelerated carbonation using different CO_2 concentrations with the presence of chloride ions.

The results of the study would be beneficial for understanding the interacted effect of the carbonation and chloride penetration on the durability of concrete.

MATERIALS AND TEST PROCEDURE

Cement paste samples were prepared by mixing the cement with water at a water cement ratio (w/c) of 0.5. The cement use was a Rapid cement type CEM II/A -LL 42.5 R, produced by Finnsementti OY. The chemical analysis of the cement is shown in Table 1.

Table 1 Chemical analysis of the type I cement used in this study

CaO	SiO_2	Al_2O_3	Fe_2O_3	C_3S	C_2S	C_3A	C_4AF	MgO
65 %	19.7 %	5,3 %	3,1 %	68 %	9 %	9 %	10 %	2,7%

The cement paste was filled into 8 plastic bottles, which were sealed then rotated for 8 hours and allowed to cure for 28 days at room temperature (22°C). The procedure of preparing the cement paste samples is shown in Figure 2.

Paste mixer

2.5 dl plastic bottle

Luckhamin CM 2000 mixer

Hardened cement paste

crushing of paste samples

Figure 2. Preparation of the cement paste samples

After curing, the specimens were demoulded. One reference sample was kept sealed to avoid carbonation. As shown in Figure 3, samples were exposed either to a combination of 4% CO_2-concentration and 10%-NaCl solution or pure carbonation at 1%, 4% or normal CO_2-

concentrations. One sample was exposed to 10%-NaCl solution only. The relative humidity during carbonations was kept at a 65%.

The chemical changes of the cement paste were analysed by using X-Ray diffractometry and thermal analysis. The XRD analyses were performed with a Philips PW 1710 –diffractometer by using CuK_{α}-radiation. The spectrums between 5º-65º (2θ) were produced with a voltage of 50 kV and a current strength of 20 mA. The TG/DTA analyses were performed with a Mettler TGA 851e –thermobalance. The analytical parameters were the following:

Atmosphere	nitrogen, 100 ml/min
Crucible	Al_2O_3, 150 µl
Heating rate	5°C/min
Maximum temperature	1000°C

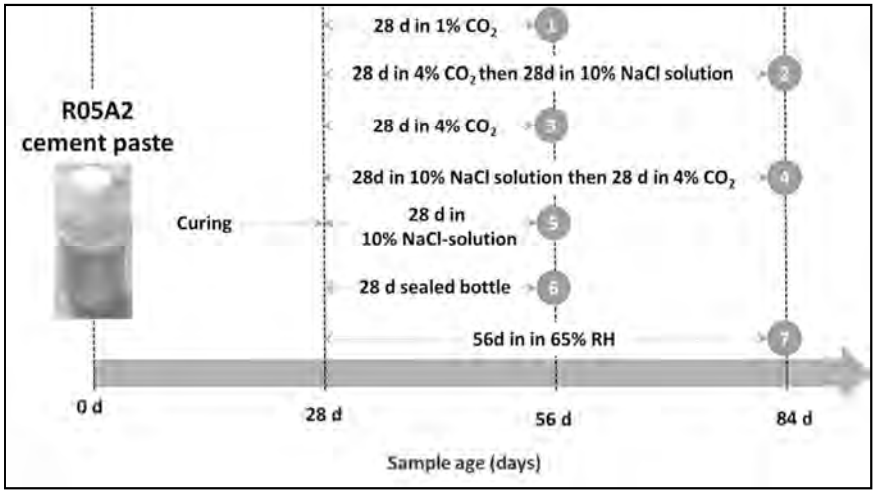

Figure 3. Test procedure for the cement paste samples

Seven paste samples, each composing of a small batch, about 100 g, of fine-grained, light-grey powder were prepared for chemical analysis. The samples are identified in Table 2.

Table 2. Cement paste samples referring to Fig. 3.

No.	Sample code	Environment
1	1% CO_2	28 days in accelerated 1% CO_2, 60% RH and temperature 20±2 °C
2	4% CO_2 + NaCl	28 days in accelerated 4% CO_2, 60% RH and temperature 20±2 °C, then stored in 10% NaCl for 28 days
3	4% CO_2	28 days in accelerated 4% CO_2, 60% RH and temperature 20±2 °C
4	NaCl + 4% CO_2	Stored in 10% NaCl for 28 days, then 28 days in accelerated 4% CO_2, 60% RH and temperature 20±2 °C
5	NaCl	Stored in 10% NaCl for 28 days
6	bottle	Sample stored in a sealed plastic bottle for 28 days
7	RH 65%	Stored in RH 65% for 56 days

RESULTS AND DISCUSSION

X-Ray Diffractometry

According to the XRD results all the paste samples were partly amorphous and contained only limited amounts of crystalline compounds. The amorphous phase forming a noticeable part of the samples composed most likely of calcium silicate hydrate gel resulting from the hydration reactions of cement with water. According to the XRD diagrams the proportion of amorphous matter seemed to be exceptionally high (> 50%) in sample 6 (bottle). Also in samples 5 (NaCl) and 4 (NaCl + 4% CO_2) it was probably a little higher than in the remaining four samples.

Calcite, i.e. calcium carbonate $CaCO_3$, was the main crystalline compound in samples 1, 2, 3, 4, 5 and 7. Obviously, most of the calcite content was formed in the carbonation reactions of the hydration products during the curing and storing processes of the samples.

All samples excluding sample 6 (bottle) contained some aragonite in addition to calcite. Aragonite is a calcium carbonate mineral with an orthorhombic crystal structure instead of the hexagonal structure, which forms the crystal system of calcite. The amount of aragonite seemed to be the highest in sample 4 (NaCl + 4% CO_2). In addition, the presence of small amounts of even a third carbonate mineral, i.e. vaterite, the so-called μ-phase of hexagonal calcium carbonate, cannot be excluded. X-ray reflections referring to vaterite were observed in all the other samples except samples 6 (bottle) and 5 (NaCl).

The main crystalline compound of sample 6 (bottle) was portlandite, i.e. calcium hydroxide $Ca(OH)_2$. It was also detected in samples 1 (1% CO_2), 3 (4% CO_2), 5(NaCl) and 7 (RH65%). According to the XRD diagrams, the samples 2 (4% CO_2 + NaCl) and 4 (NaCl + 4% CO_2) did not contain portlandite.

All the samples contained small amounts of unhydrated cement minerals. It is probable that most of those composed of dicalcium silicate (C_2S). On the other hand, also traces of tetracalcium aluminate ferrite, brownmillerite, (C_4AF) could be detected in the samples.

All the samples except for sample 2 (4% CO_2 + NaCl) contained small amounts of the so-called AFt-phase, i.e. ettringite $Ca_6Al_2(OH)_{12}(SO_4)_3 \cdot 26H_2O$. Gypsum, $CaSO_4 \cdot 2H_2O$, was observed in samples 6 (bottle) and 2 (4% CO_2 + NaCl).

Halite, i.e. sodium chloride NaCl, was observed in samples 2 (4% CO_2 + NaCl), 5 (NaCl) and 4 (NaCl + 4% CO_2). Especially in sample 2 (4% CO_2 + NaCl) the content of halite was considerably high.

Table 3. The content of the crystalline compounds in the cement pastes (XRD).

No.	**1**	**2**	**3**	**4**	**5**	**6**	**7**
Sample	1% CO_2	4% CO_2 + NaCl	4% CO_2	NaCl + 4% CO_2	NaCl	bottle	RH 65%
Calcite	+++++	+++++	+++++	+++++	+++++	++++	+++++
Aragonite	++	++	++	++	++	-	+++
Vaterite	++	++	++	++	-	-	++
Portlandite	++	-	++	-	+++	+++++	+++
Dicalcium silicate	+++	++	++	+++	++	(+)	+++
$C_4AF^{(1)}$	(+)	(+)	(+)	(+)	(+)	(+)	(+)
Ettringite	++	-	+	+	++	+++	+
Gypsum	-	++	-	-	-	+++	-
Halite	-	+++++	-	+++	++	-	-

+++++	very high	+++	medium	+	very low
++++	high	++	low	-	not detected

(1) C4AF = Calcium Ferro Aluminate

The summary of the contents of the crystalline compounds in the samples is presented in Table 3. The estimates presented for the amounts of the minerals are based on the relative intensities of the reflections observed in the XRD diagrams of the samples. Thus, they are only valid for each sample separately, and the estimates cannot be compared with each other. The XRD diagrams of the cement pastes are shown in Figure 4.

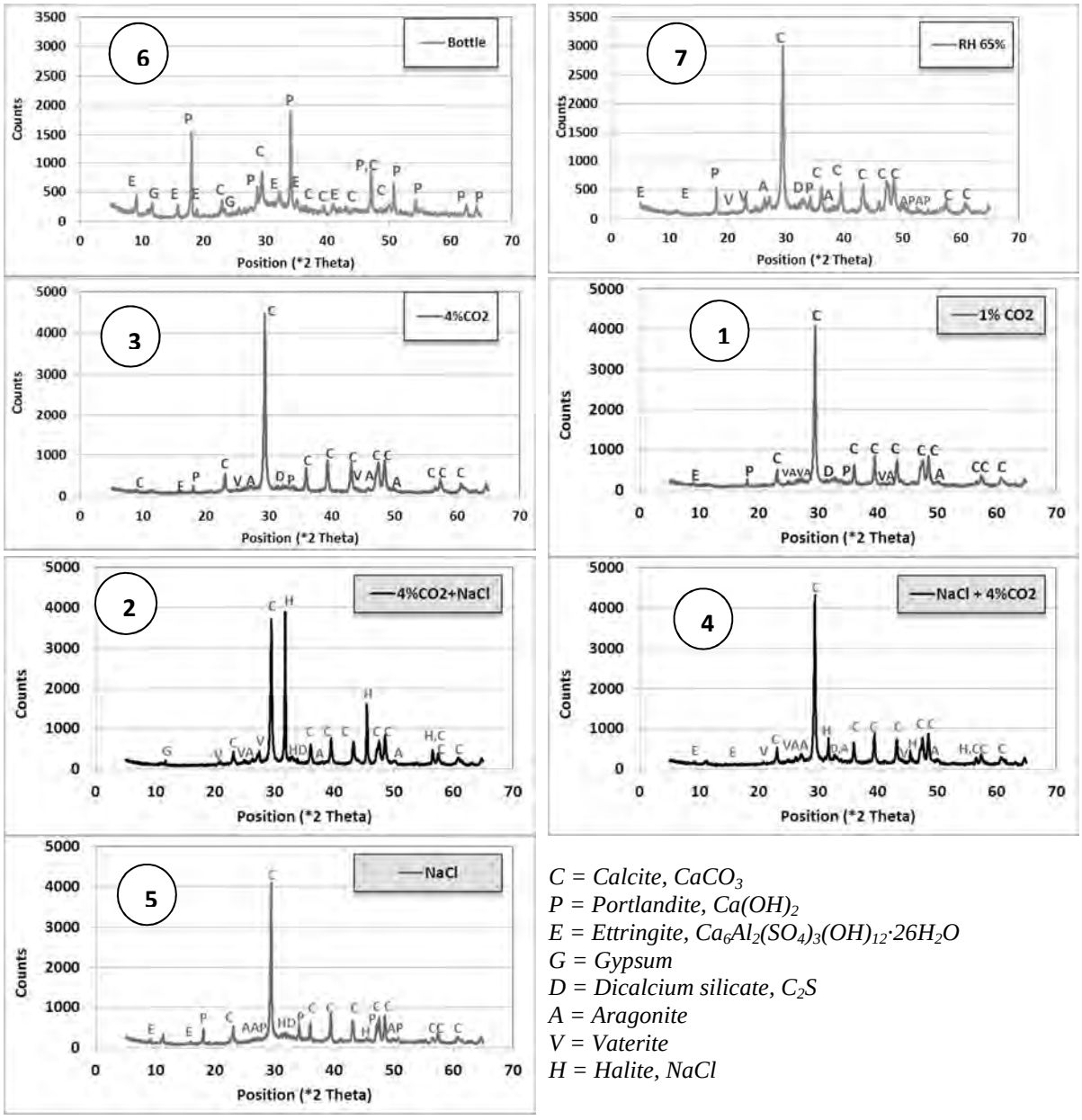

Figure 4. X-ray diffraction diagrams for the samples analyzed.

Thermal Analysis (TG/DTA)

The thermal decomposition of paste samples 6 (bottle), 1 (1% CO_2), 3 (4% CO_2) and 7 (RH 65%) was similar. It could be divided into eight successive phases (seven in the sample (bottle))

during which degradation reactions causing mass loss were detected. The temperature areas of the various phases and the mass losses registered are presented in Table 4.

The thermal behavior of paste samples 2 (4% CO_2 + NaCl), 5 (NaCl) and 4 (NaCl + 4% CO_2) was somewhat different from the behavior of the four other paste samples. However, their behavior could also be divided into eight (nine in the sample (NaCl)) successive phases during which decomposition reactions causing mass loss were detected. The temperature areas of the various phases and the mass losses registered are presented in Table 5. The thermal curves of the cement pastes are shown in Figure 5.

Table 4. Temperature ranges for thermal decomposition of cement pastes 6 (bottle), 1(1% CO_2), 3 (4% CO_2) and 7 (RH 65.

Phase	**Temperature [ºC]**	**Mass loss / wt-%**			
		6 (bottle)	**1 (1%CO_2)**	**3 (4%CO_2)**	**7 (RH 65%)**
I	25 – 165	21.93	8.23	8.43	6.87
II	165 – 215	1.36	1.21	1.15	1.52
III	215 – 305	2.11	1.54	1.34	1.32
IV	305 – 405	1.90	1.38	1.63	1.78
V	405 – 470	4.26	0.84	1.52	2.15
VI	470 – 630		9.33	8.17	8.15
VII	630 – 770	2.33	12.71	14.50	12.45
VIII	770 – 980	0.47	0.82	0.72	0.99
		34.36	36.06	37.46	35.23

Table 5. Temperature ranges for thermal decomposition of cement pastes 2 (4% CO_2 + NaCl), 5 (NaCl) and 4 (NaCl + 4% CO_2).

Phase	**Temperature [ºC]**	**Mass loss / wt-%**		
		2 (4% CO_2 + NaCl)	**5 (NaCl)**	**4 (NaCl + 4% CO_2)**
I	25 – 160	8.40	14.22	12.76
II	160 – 250	1.51	1.78	1.84
III	250 – 370	1.57	3.04	2.12
IV	370 – 460		1.51	
V	460 – 535	5.98	1.03	6.53
VI	535 – 645	6.57	3.32	5.86
VII	645 – 725	6.82	6.51	7.13
VIII	725 – 770	2.15	2.08	2.17
IX	770 – 990	7.63	4.49	5.19
		40.63	37.98	43.60

The first degradation phase of all the cement pastes presented in Tables 4 and 5 was caused by the volatilization of chemically bound water resulting from the disintegration of the C-S-H gel and the sulphate minerals ettringite and gypsum. On the other hand, it seems probable that at least part of the mass loss during the first phase resulted from the evaporation of free moisture the samples still contained.

The phases II-V were also due to the disintegration of the hydration products of cement, i.e. C-S-H and C-A-H compounds, leading to the evaporation of chemically bound water. The fifth phase of the samples S1, S2, S3/28d and S6 and the fourth phase of the sample S5/28d were especially connected to the degradation of calcium hydroxide these samples contained.

The phases VI-VII in samples 6 (bottle), 1 (1% CO_2), 3 (4% CO_2) and 7 (RH 65%) and the phases VI-VIII in samples 2 (4% CO_2 + NaCl), 5 (NaCl) and 4 (NaCl + 4% CO_2) resulted from the decomposition of calcium carbonate minerals, calcite, aragonite and, possibly, vaterite, and the subsequent evaporation of carbon dioxide from the samples. It is noteworthy that in the three samples 2 (4% CO_2 + NaCl), 5 (NaCl) and 4 (NaCl + 4% CO_2) the carbonate decomposition was divided into three distinct sub-reactions whereas in the four other samples only two reactions were observed (only one in sample 6 (bottle)).
The last mass loss phase (VIII/IX) of the cement paste samples was most probably connected to the vaporization of easily volatile components like alkali salts. This was evident especially in the samples that had been treated with sodium chloride, i.e. in samples 2 (4% CO_2 + NaCl), 5 (NaCl) and 4 (NaCl + 4% CO_2).
The summary of the results of the thermal analyses performed is presented in Table 6. The total mass losses, Δm_T, of the paste samples were divided into five parts in the following way:

Δm_1 = the amount of chemically bound water in C-S-H/C-A-H gel and sulphates evaporating at low (<160°C) temperatures (possibly some free moisture included)
Δm_2 = the amount of chemically bound water in C-S-H/C-A-H gel evaporating at higher (>160°C) temperatures
Δm_3 = the amount of chemically bound water in calcium hydroxide
Δm_4 = the amount of chemically bound carbon dioxide in carbonate minerals
Δm_5 = the amount of volatile components at high temperatures (>770°C)

Table 6. The summary of the results of the thermal analyses of the cement pastes.

No	**6**	**1**	**3**	**2**	**5**	**4**	**7**
Sample	**bottle**	**1%CO_2**	**4%CO_2**	**4% CO_2 + NaCl**	**NaCl**	**NaCl + 4% CO_2**	**RH 65%**
	wt-%	wt-%	wt-%	wt-%	wt-%	wt-%	wt-%
Δm_1	21.93	8.23	8.43	8.40	14.22	12.76	6.87
Δm_2	5.37	4.13	4.12	9.06	5.85	10.49	4.62
Δm_3	4.26	0.84	1.52	-	1.51	-	2.15
Δm_4	2.33	22.04	22.67	15.54	11.91	15.16	20.60
Δm_5	0.47	0.82	0.72	7.63	4.49	5.19	0.99
Δm_{Total}	34.36	36.06	37.46	40.63	37.98	43.60	35.23

Table 7 contains the amounts of calcium hydroxide and calcium carbonate in the samples. The amount of calcium hydroxide was calculated by assuming that all the mass loss during the fifth phase of the samples (bottle), (1%CO_2), (4%CO_2) and (RH 65%) and during the fourth phase of the sample (NaCl) resulted from the decomposition of calcium hydroxide leading to the evaporation of the hydroxide water. It is probable, however, that some of the mass loss of the phases mentioned was caused by other factors, e.g. by degradation of C-S-H gel. Thus, the values presented for calcium hydroxide in Table 7 are probably a little too high.

Table 7. The amounts of calcium hydroxide and calcium carbonate in the cement pastes.

No	**Sample**	**Calcium hydroxide wt-%**	**Calcium carbonate wt-%**
1	1% CO_2	3.45	50.12
2	4% CO_2 + NaCl	-	35.34
3	4% CO_2	6.25	51.56
4	NaCl + 4% CO_2	-	34.48

5	NaCl	6.21	27.09
6	bottle	17.52	5.30
7	RH 65%	8.84	46.85

The amount of calcium carbonate was calculated correspondingly, i.e. by assuming that all the mass loss during the phases VI-VII of samples 6 (bottle), 1 (1% CO_2), 3 (4% CO_2) and 7 (RH 65%) and during the phases VI-VIII of the samples 2 (4% CO_2 + NaCl), 5 (NaCl) and 4 (NaCl + 4% CO_2) resulted from the decomposition of the various calcium carbonates.

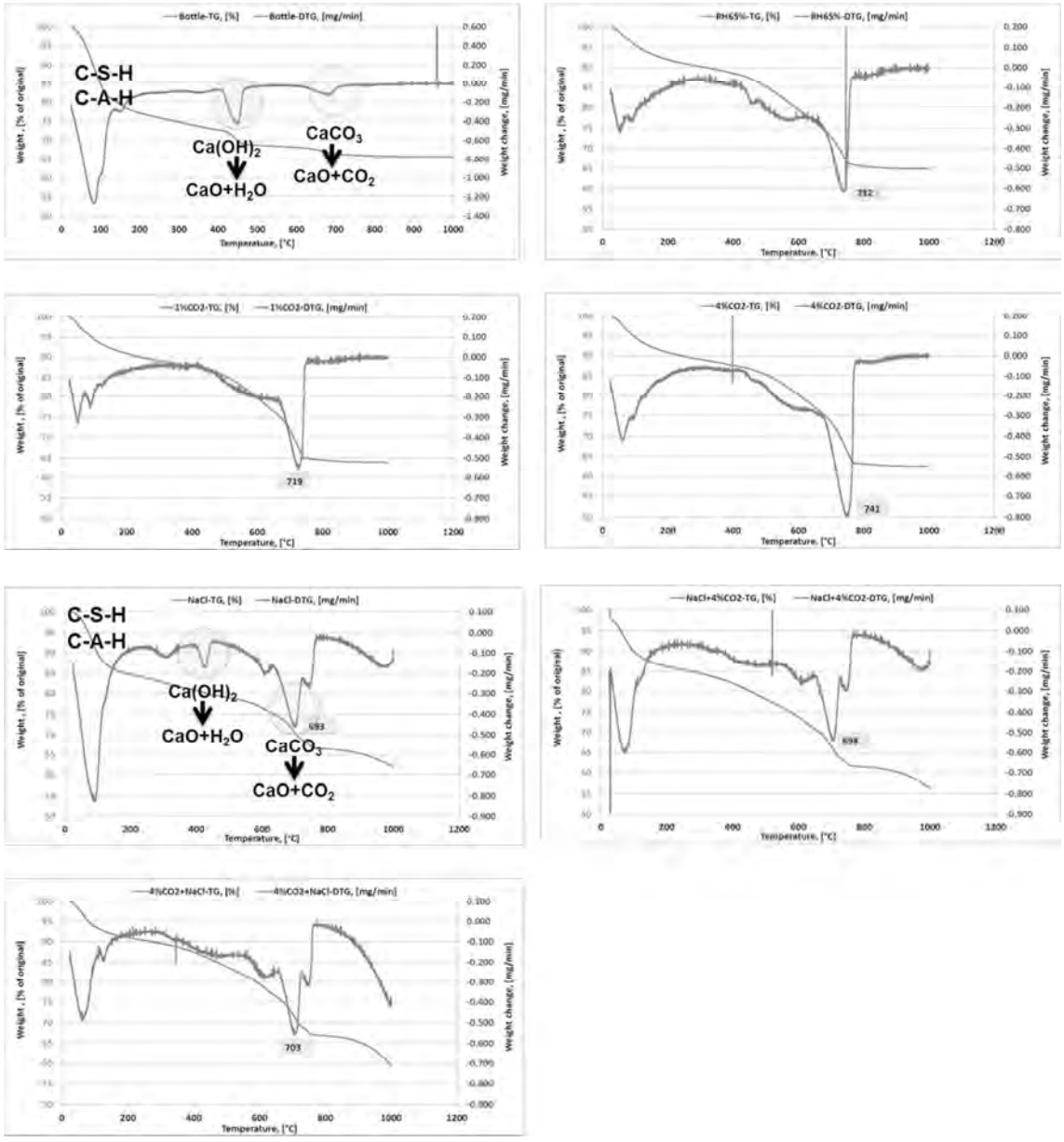

Figure 5 TG and DTG curves for the different samples

CONCLUSION

In this paper, a study on the chemical changes and phase analysis of cement paste due to accelerated carbonation and chloride penetration has been carried out by XRD and thermogravimetric analysis

The results indicate that the content of the crystalline compounds and the thermal decomposition of cement paste were similar for all samples exposed to accelerated carbonation regardless of the CO_2-concentration. The chloride penetration caused a difference in the content of the crystalline compounds and the thermal decomposition of the cement paste.

REFERENCES

22. Castellote, M., Fernandez, L., Andrade C. and Alonso C. (2008). Chemical changes and phase analysis of OPC pastes carbonated at different CO2 concentrations. RILEM, Materials and Structures, Volume 42, Number 4, pp. 515-525.
23. Houst, Y. F. (1996). The role of moisture in the carbonation of cementitious materials. International journal for restoration of buildings and monuments, Volume 2, pp. 49-66.
24. Barberona, F., Baroghel-Bounya, V., Zannib, H., Bressonc, B., Cailleriec, J-B., Malosseb, L. and Gan, Z. (2005). Interactions between chloride and cement-paste materials. Elsavier, Magnetic Resonance Imaging 23, pp. 267–272
25. Sang-Hwa, J., Young-Jun, C., Bong-Chun, L. (2007). Influence of carbonation on the chloride diffusion in concrete. Proceedings of the International Conference on Sustainable Building Asia, 27-29 June 2007, Seoul, Korea. Online at: http://www.irbnet.de/daten/iconda/CIB8265.pdf [Accessed 24.5.2016].
26. Bertos, M.F., Simons, S.J.R., Hills, C.D. and Carey, P.J. (2004). A review of accelerated carbonation technology in the treatment of cement-based materials and sequestration of CO2. Elsevier, Journal of Hazardous Materials B112. pp. 193–205.

Climate change effect on wind-driven rain on facades

Toni A. Pakkala
M.Sc., PhD Student
Tampere University of Technology
P.O. Box 600
FI-33101 Tampere
E-mail: toni.pakkala@tut.fi

Antti-Matti Lemberg
B.Sc.
Tampere University of Technology
P.O. Box 600
FI-33101 Tampere
E-mail: antti-matti.lemberg@student.tut.fi

Jukka Lahdensivu
D.Sc., Adjunct Professor
Tampere University of Technology
P.O. Box 600
FI-33101 Tampere
E-mail: jukka.lahdensivu@tut.fi

Matti Pentti
D.Sc., Professor
Tampere University of Technology
P.O. Box 600
FI-33101 Tampere
E-mail: matti.pentti@tut.fi

ABSTRACT

It has been shown that the wind-driven rain has a major effect on all of the most significant concrete degradation mechanism in Finland and the degradation rate depends significantly on both location and orientation of outdoor concrete surface, e.g. façade. In this study, the amount of wind-driven rain and the effect of climate change on it has been studied at four different locations. As a result, it was found that at present the climatically most stressed façade orientations at the most stressed areas, the coastal and southern Finland areas, will face significantly more wind-driven rain in the future climate.

Keywords: concrete; wind-driven rain; durability; climate change

1 INTRODUCTION

More than 60 % of the Finnish building stock has been built in the 1960's or later. There are a total of 1.2 million apartments in the Finnish block of flat stock, of which 50% has been built during 1960-1979 [1]. Despite of young age of Finnish block of flats a considerable number of envelopes of the precast concrete buildings erected in that era have come near the end of the service life largely due to degradation.

Based on the latest research conducted at Tampere University of Technology (TUT), the durability properties of existing concrete façades and balconies have been found to be poor [2,3,4]. The material properties related to freeze-thaw resistance of concrete and cover depth of reinforcement rarely fulfil the requirements of national building codes. According to these studies, in 59.2% of Finnish concrete facades have been local corrosion damage and in 42.7% freeze-thaw damage. On the other hand, the protective pore ratio is less than 0.15 in about 70% of existing concrete facades and balconies. However, despite the insufficient durability properties of concrete, wide spread damage that can be seen visually are relative rare, less than 7%.

Moisture behaviour and environmental stress conditions have a strong impact on frost damage of concrete. For instance, the stress on concrete facade depends on the existence of proper waterproofing and prevailing wind direction during raining. Visual damage of concrete façades and balconies has a strong correlation with precipitation, wind directions during the rain and freeze-thaw cycles directly after the rain events [3,4,5].

The increasing amount of precipitation has been shown to have a strong correlation with the rate of the two most important deterioration mechanisms of Finnish outdoor concrete structures: freeze-thaw deterioration and carbonation induced corrosion of reinforcement [4,6]. In the present climate incipient freeze-thaw damage takes 22 years in average in non-frost resistant concrete [3]. Thus, it is important to explore the possible climate change scenarios considering their effect on critical outdoor conditions for deterioration of structures, for the repair need of existing building stock and for the timing of repair actions.

1.1 Research objective

Because it has been shown that the wind-driven rain (WDR) has a major effect on all of the most significant concrete degradation mechanism in Finland, in this paper the effect of climate change on the amount of the WDR on concrete facades is studied to assess the differences of climatic loads at variable locations and façade orientation. The climate data projections made by FMI are studied to estimate the possible changes on the amount of WDR on variable façade orientations at different locations in Finland.

2 BACKGROUND

2.1 Finnish concrete facades

Since 1970s almost all prefabricated concrete structures in Finland are based on the Concrete Element System [7]. That open system defines, for instance, the recommended floor-to-floor

height and the types of prefabricated panels used. In principle, the system allows using the prefabricated panels made by all manufacturers in any single multi-storey building.

Until 1980s dominant surface of the prefabricated concrete facades were exposed aggregate, brushed painted and painted form-finish concrete. Also brick tile and ceramic tile finishing were popular. Since 1990s white concrete and coloured white concrete have penetrated the market. [3]

2.2 Quality of concrete

The concrete grade used for concrete facade panels and most structural members of balconies has been C30/37 since the late 1980's in Finland based on the guidelines for durability and service life of concrete. Earlier the grade was C20/25. The cement used for concrete panels is mostly CEM I (42.5 N) (ordinary Portland cement) because of the good early strength it gives to concrete which allows rapid formwork rotation at the precast panel plant. White cement, CEM I (52.5 R), is also used in facade panels if necessary, but its share of total use is marginal.

The freeze-thaw resistance of the concrete is conducted by air-entrainment of fresh concrete and it can be determined by testing a protective pore ratio (p_r). In 1976 Concrete Codes started to recommend the protective pore ratio of 0.15 which means that at least 15 % of all pores are never filled by capillary water. At the Concrete Code 1989, the protective pore ratio was lifted to reach at least 0.20. Protective pore ratio $p_r < 0.10$ can be considered to make concrete non-freeze-thaw-resistant in Finnish outdoor climate [3].

The success of air-entrainment of concrete used in facades and balconies have been studied by Lahdensivu [3] from the thin section analysis results of the samples in the BeKo database (buildings built 1960-1995). Based on the study the freeze-thaw resistance differs considerably between various surface types of facades. Pakkala et al. [4] studied buildings built after the requirement of protective pore ratio of 0.20 has been demanded and presented that only approx. 50 % of the precast panels have met the freeze-thaw resistance requirements.

Lahdensivu [3] presented that visually observable reinforcement corrosion damage existed in 59% of the examined facades. 54 % of damage was local and extensive corrosion was found only in 5.7% of the facades. The corrosion damage was almost solely due to carbonation.

2.3 Deterioration rate of Finnish concrete facades

The deterioration rate and need for repair of existing outdoor concrete structures, especially concrete facades and balconies, have been monitored by systematic condition assessments over 20 years. Lahdensivu [3] studied in his doctoral thesis the deterioration of prefabricated concrete element buildings at present climate. His studies were based on 947 condition assessment reports made on buildings built 1960 – 1996 [2]. He studied the changes on quality requirements, dominating deterioration mechanisms, their progress on present climate based on climate data produced by the Finnish Meteorological Institute (FMI) and effect of a geographical distribution on them. The most essential results were:

- There is a significant lack of quality with concrete structures, also with structures made according to current concrete code,
- The most significant deterioration mechanisms have been carbonation induced corrosion and freeze-thaw weathering,
- The most significant climatic causes for damage have been wind-driven rain and freeze-thaw cycles within few days after the rain events,
- The deterioration rate has been faster in coastal areas than in inland.

Two recent studies by Pakkala et al. [4] and Köliö et al. [6] studied rates of freeze-thaw weathering of concrete facades and carbonation induced corrosion of concrete reinforcement, respectively, at the projected future climate. Köliö et al. presented that the increase of precipitation decelerates the carbonation rate and thus the initiation phase of reinforcement corrosion while the increase in CO2 level has a greater opposite impact. On the other hand, the increase of precipitation amount and temperature accelerate the active corrosion phase. Pakkala et al. concluded e.g.:

- Amount of precipitation will increase significantly until the end of the century and relatively more at inland than at coastal areas,
- Amount of freeze-thaw cycles after rain events will decrease significantly after 2050's at southern Finland but remains almost at the same level at inland,
- The amount of precipitation is almost the same at coastal areas and inland but at coastal areas the rate of freeze-thaw weathering is higher because of the annual average wind speed is higher, thus more of the precipitation will shower the vertical surfaces,
- The wind-driven rain load is both at present and at future significantly concentrated on south-west, south and south-east orientated facades and its relative increase is greater than the increase of precipitation because of the higher wind speed during the rain,
- Concrete can be durable in the Nordic climate if it has been properly air-entrained.

3 CLIMATIC STRESS ON OUTDOOR STRUCTURES

3.1 Modelling of wind-driven rain

The wind-driven rain (WDR) striking building facades has been the focus of several studies in the last decades as mentioned by Blocken & Carmeliet [8]. The moisture load resulting from driving rain depends not only on rainfall intensity and wind speed, but also on raindrop trajectories around buildings. That increases the complexity of the phenomenon greatly. According to Jerling and Schechninger [9], the upper parts and corners of facades get more rainfall than lower and central parts. Prevailing wind directions and wind speeds also have a strong influence on the distribution of rainfall across a building. Winds are stronger at higher levels of buildings than close to ground level which naturally leads to upper sections of high buildings receiving more rain and sleet stress than lower buildings, and lower sections of buildings in general. [10]

Experimental, numerical and semi-empirical methods have been developed and employed for the estimation of parameters related to driving rain against building facades [11]. The annual driving rain index (aDRI) that is calculated on the basis of average annual wind speed and average amount of total annual rainfall is proportional to the amount of water on a windward

vertical [12]. Based on the classification proposed by Lacy (sheltered areas, moderately exposed areas, severely exposed areas), driving rain maps have been produced for several countries including Sweden, United Kingdom, Canada, China, India, Nigeria, Turkey, Greece and Spain [11].

Differences in the time resolutions of climatic data sets may result in large discrepancies in the calculated indices. In most cases hourly data are considered to have adequate time resolution. Given that in many cases hourly data covering adequate periods of time are not available, some methods for the derivation of directional driving rain indices on the basis of synoptic data have been formulated [13,14,15]. However, the driving rain indices cannot be used for direct estimation of the driving rain load on building components at site. Quantification of the amount and intensity of this load (formation of the wind pressure field around each building) is a complex task. The building's geometry and the position of the area under study on the building's vertical surface (height, middle part of the surface or near the edges) influence the resulting load [11,16,17,18,19,20,21]. Example calculations of quantitative parameters related to driving rain (e.g. intensity) for specific sites are found in several studies, e.g. [22,23,24].

The standard SFS-EN ISO 15927-3 [25] presents a factor I_{WA} (Wall annual index) which can be used to estimate amount of precipitation collected by a free-standing driving-rain gauge in flat open country to present the amounts of precipitation that impacts on a real wall. The wall annual index is highly simplified simulation for assessing the WDR against building facades. There are other methods to model the WDR as is mentioned by Blocken and Carmeliet [8,26], e.g. CFD model. It takes into account more precisely the distribution of the WDR in different areas of the facades. Although the wall annual index is simplified method, it gives adequate results for e.g. comparing different locational effects on the amount of wind driven rain on facades. Compared to CFD modelling it underestimates the amount of wind driven rain near the top of the façade but overestimates the amount on the top 2.5 metres with high buildings and low rain intensity. The higher the rain intensity the more it underestimates the amount of wind driven rain. The underestimation increases near the edges of the building. With rain intensities from 10 mm/h to 30 mm/h the wall annual index gives adequately corresponding results with CFD modelling in the vertical middle line with high and low rise vertical buildings and tower buildings. [27]

3.2 Climate change projections

Climate change as such has been studied worldwide for a long time. In this context, climate change refers to global warming caused by an increase in greenhouse gases, especially carbon dioxide (CO_2). Climate change will affect the geographic and seasonal distribution of precipitation, wind conditions, cloudiness, air humidity and solar radiation. Modelling of future climate is based on alternative scenarios of greenhouse gas and aerosol particle emissions. In the scenarios, different assumptions are made about the future development of population growth, economic development, energy production modes, etc.

The ACCLIM [28] and FRAME [29] projects have shown that future climate conditions in Finland are likely to get worse in terms of durability of facades and other structures exposed to climate. According to the data of the ACCLIM project, precipitation during the winter season is also going to increase while the form of precipitation is going to be increasingly water and sleet. At the same time, the conditions for drying are going to get worse. Thus, the deterioration rate of structures will accelerate in most of Finland if maintenance and protection actions are neglected. [3]

The Finnish Meteorological Institute (FMI) examined in the ACCLIM project the different climate models and built models for observing Finnish climatic conditions and adaptation to climate change. In all greenhouse gas emission scenarios, based on three IPCC [30] scenarios for the evolution of greenhouse gas and aerosol particle emissions, the average temperature rises at a constant rate until 2040. Differences between the scenarios start to emerge only after the middle of the century, see figure 1. [31]

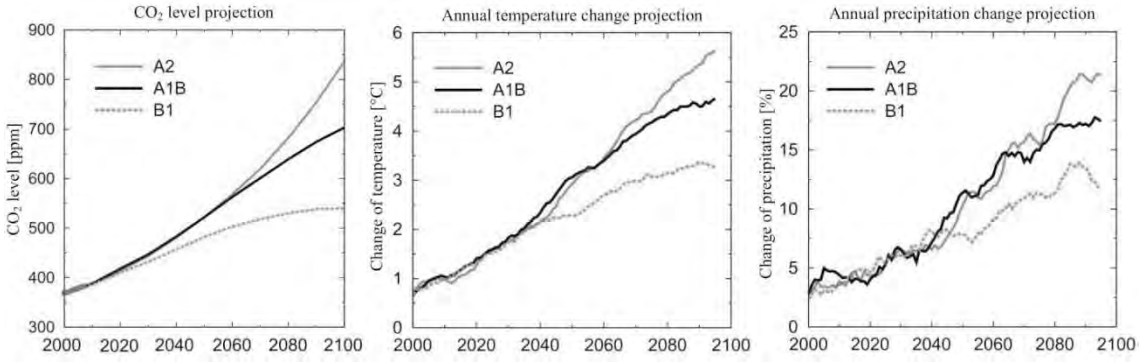

Figure 1 – Projections for (a) CO2 level, (b) annual mean temperature and (c) precipitation change in 2000–2100, in relation to the mean of the reference period 1971–2000. The curves depict 11 year running means, averaged over Finland and the responses of 19 global climate models [31]. Projections are given separately for the three greenhouse gas scenarios A2, A1B and B1 [30].

The FMI has extensive weather data since 1961 in digital form from several meteorological stations covering all of Finland. The data consist of temperature, relative humidity, rain intensity, wind speed and direction, solar radiation variables, etc. These observations have been collected at least daily and three times a day at best. In the REFI-B project [31] the FMI also forecast the climates of the four regions (coastal area, southern Finland, inland, Lapland) in three periods (2030, 2050 and 2100). The forecasts are based on an average of 19 different models which are all based on greenhouse gas emission scenario A2. The A2 scenario involves a situation where greenhouse gases are assumed to increase significantly − it is a sort of worst-case scenario. The FMI also has other significant greenhouse gas emission scenarios: A1B (quite large emissions) and B1 (small emissions). [31]

3.3 Climatic conditions in Finland

Although Finnish climate is relatively steady considering the latitudes, it still varies significantly from the mild and relatively rainy coastal area to the drier inland. However, the Finnish building stock is mainly concentrated in the few biggest cities and surrounding growth areas. Finland can be divided into four main areas based on climatic differences and concentration of population: the coastal area, southern Finland, inland and Lapland, see figure 2. [4]

Figure 2 – Finland can be divided into four main areas based on climate and concentrations of population. [4]

Pakkala et al. [4] presented that both the amount of precipitation and the amount of the WDR are highly concentrated on west to south-east directions and will be even more concentrated on future climate. The same phenomenon has been noted in condition assessment studies where the most deterioration has been observed on south-facing facades and balconies.

4 MATERIAL AND METHODS

4.1 Climate data

Present and future climate projections and their effects on weather conditions critical to concrete degradation have been prepared by the Finnish Meteorological Institute (FMI). The data used in this study are hourly interpolated observations of temperature, wind speed, wind direction and amount of precipitation over 30 years (1980–2009). The data of amount of precipitation, the wind speed and the wind direction were collected every three hours and interpolated to hourly data.

The future climate projections, based on the A2 scenario, were calculated by FMI to represent hourly data for a similar period in 2050 and 2100. The calculations of this study focus on all four locations presented in the Figure 2: coastal area, southern Finland, inland and Lapland.

4.2 Typical Finnish suburb

The locations of the buildings used in this study are set to the same areas as the climate data mentioned above. Imaginary Finnish suburban city blocks, shown in the figure 3, are located at

the coastal area, southern Finland, inland and Lapland. Two types of building were studied, both represented typical Finnish multi-storey residential building of 1970's with 2 staircases. The other one was 4- and the other 8-storey, see figures 4 and 5.

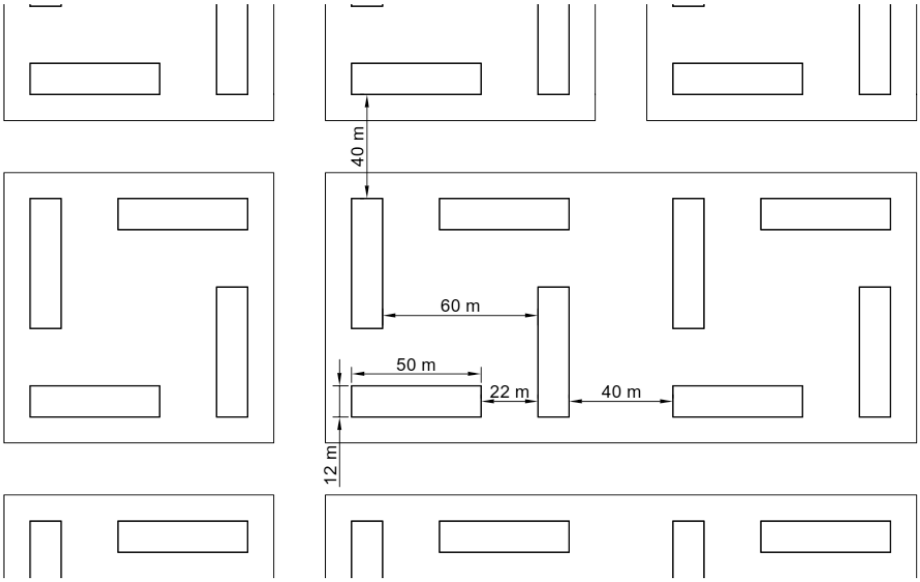

Figure 3 – Simplified Finnish suburban street plan with repetitive blocks.

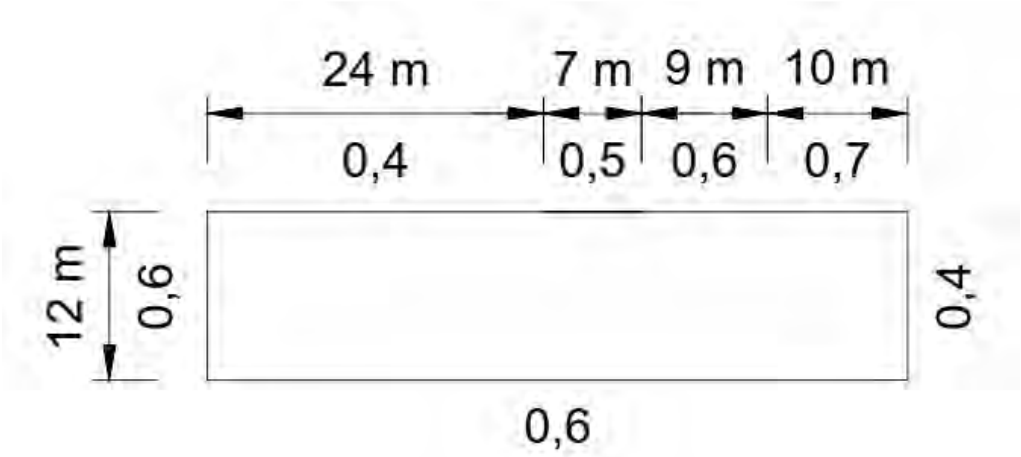

Figure 4 – The dimensions of studied building and the obstruction factor, see section 4.3, based on the suburban street plan presented at Figure 3.

Figure 5 Typical Finnish suburban precast concrete buildings.

4.3 Modelling of wind-driven rain

The Wall annual index I_{WA} is presented at the standard SFS-EN ISO 15927-3 [25] as follows:

$$I_{WA} = I_A C_R C_T O W \quad (1)$$

, where I_A is the airfield annual index, C_R is a terrain roughness coefficient, C_T is a topography coefficient, O is an obstruction factor and W is a wall factor. The airfield annual index I_A is defined as:

$$I_A = \frac{2}{9}\frac{\sum v r^{\frac{8}{9}} \cos(D-\theta)}{N} \quad (2)$$

, where v is an hourly mean wind speed [m/s], r is an hourly rainfall total [mm], D is an hourly mean wind direction from north [°], θ is a wall orientation relative to north [°], N is a number of years for which data is available and the summation is taken over all hours for which $\cos(D - \theta)$ is positive.

The roughness coefficient depends on the height above the ground and the roughness of the terrain in the direction from which the wind is coming, i.e. is there an open sea, a farm land, a suburban area or an urban area in the upwind direction. The coefficient C_R at height z is calculated as follows:

$$C_R(z) = K_R \ln(\frac{z}{z_0}) \qquad \text{for } z \geq z_{min} \quad (3)$$

$$C_R(z) = C_R(z_{min}) \qquad \text{for } z < z_{min} \quad (4)$$

This study uses only the terrain category *III*, see table 1, because typical Finnish suburban is usually located at considerably sheltered locations and is often surrounded by sector of forest.

Table 1 – Terrain categories and related parameters. [25]

Terrain category	Description	K_R	z_0	z_{min}
I	Rough open sea; lake shore with at least 5 km open water upwind and smooth flat country without obstacles	0.17	0.01	2
II	Farm land with boundary hedges, occasional small farm structures, houses or trees	0.19	0.05	4
III	Suburban or industrial areas and permanent forest	0.22	0.3	8
IV	Urban areas in which at least 15 % of the surface is covered with buildings of average height exceeding 15 m	0.24	1	16

The topography coefficient takes into account the increase of mean wind speed over isolated hills and escarpments near the building subjected to the study. In this research the studied buildings are consider to locate at flat surroundings when the topography coefficient $C_T = 1$.

The obstruction factor depends on the horizontal distance to the nearest obstacle which is at least as high as the wall subjected to the study, see table 2. The obstacle is taken into account when it is located at the line of sight from the horizontal view away from the wall, i.e. over a sector spanning 25° either side of the normal to the wall. The wall factor is, in the case of flat roof multi-storey building, 0.5 for the top 2.5 m of the wall and 0.2 for remainder.

Table 2 – Obstruction factor. [25]

Distance of obstruction from wall [m]	4 – 8	8 – 15	15 – 25	25 – 40	40 – 60	60 – 80	80 – 100	100 – 120	over 120
Obstruction factor O	0.2	0.3	0.4	0.5	0.6	0.7	0.8	0.9	1.0

Limitations of using the standard SFS-EN ISO 15927-3
Using the standard requires data from at least 10 years and preferably 30 years of hourly values of wind speed, wind direction and rainfall. The data, referred in this study as present, is collected from 1980 to 2009. The climate change projections are also made to represent 30 years' data and the studied periods are from 2035 to 2064 (referred in this study as 2050), and from 2085 to 2114 (referred in this study as 2100).

As mentioned before, the used data is collected in every three hours and interpolated to hourly values. The interpolation effects mostly on the rain intensity and mildly also the wind speed and direction during the rain event. However, it is considered to meet the aim of this study to compere different locations and climate change projections with each other.

In addition, there are three other limiting terms when the standard does not apply as mentioned in the standard: (1) mountainous areas, (2) areas in which 25% of the annual rainfall comes from severe storms and (3) areas and periods when a significant proportion of precipitation is made up of snow and hail.

The term (1) is met because Finnish landscape is flat except the most north-western part where the population is extremely low. The term (2) is also met because 6-7% (0-8 days) of the raining days in Finland are the ones when the rain intensity is thought to be quite severe, over 20 mm per day. [32]

Meeting the term (3) is the most questionable. At south-western part of Finland 30% of the precipitation is in the form of snow and on the other parts between 40-50%. The standard does not specify the "significant proportion" but it can be assumed that the kind of amounts are a significant proportion and thus, the data cannot be applied as it is. For meeting the term, in this study only the rain events when temperature is over 0 °C during and two hours before the events are taken into account.

5 RESULTS AND DISCUSSION

As has been noted before WDR is highly concentrated between west to south-east directions at every studied location in Finland. As a result of it and because of higher wind speeds during the rain events, at coastal area and southern Finland the Airfield annual index (I_A), see equation 2, is 3.5 and 2.9 times higher, respectively, from southern compared northern direction, see table 3 and figure 6. As a consequence of a more uniform distribution of wind direction and wind speed during the rain events the same figures are 1.8 and 1.5 at inland and Lapland, respectively.

Table 3 – Amount of average annual Airfield annual index I_A *from different wind directions at present climate and future climate projections.*

Wind direction	Coastal [mm/year]			Southern Finland [mm/year]			Inland [mm/year]			Lapland [mm/year]		
[° from north]	Present	2050	2100	Present	2050	2100	Present	2050	2100	Present	2050	2100
0	70	82	96	63	73	85	67	79	96	54	63	78
30	76	88	97	69	79	85	59	69	81	56	65	78
60	88	102	107	78	89	90	59	70	78	57	66	79
90	115	134	137	93	104	103	77	94	104	61	72	90
120	160	190	200	121	136	136	105	128	147	71	86	112
150	217	256	285	160	181	191	122	149	175	80	99	130
180	247	289	335	183	209	235	120	146	176	79	99	130
210	233	270	323	178	207	245	102	123	152	68	85	110
240	184	211	259	149	175	218	81	96	121	52	65	83
270	123	140	174	105	125	163	72	85	107	41	50	64
300	79	92	113	72	87	113	74	87	109	40	49	63
330	68	80	97	63	74	91	73	87	107	48	57	72

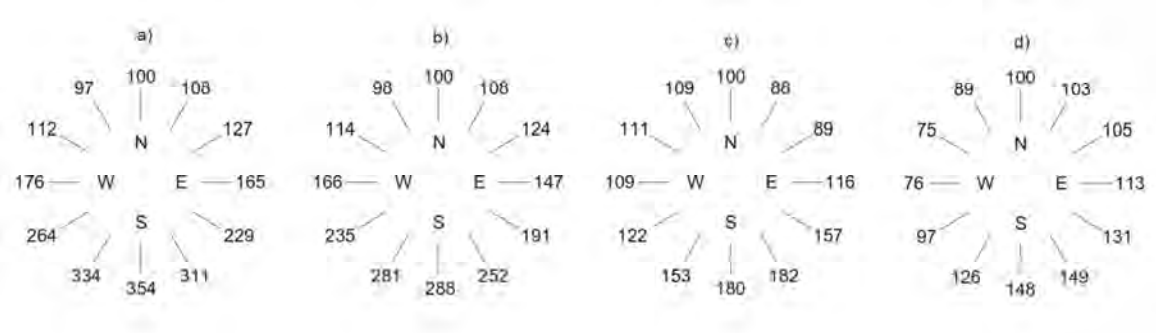

Figure 6 – Relative amount of I_A *compared to* I_A *from north direction at present climate from different wind directions at a) coastal area, b) southern Finland, c) inland and d) Lapland.*

At coastal area the I_A is at present climate on average 24%, 64%, 135% higher than at southern Finland, inland and Lapland, respectively, while the amount of precipitation is only 12%, 20% and 68% higher. The difference is a consequence of higher wind speed at coastal areas. At the coastal area 74% of precipitation hits a vertical wall while at inland the share is 66%, at southern Finland 54% and at Lapland 53%.

Depending of the façade orientation the I_A is at present climate 8 – 36% higher at the coastal area compared to southern Finland. The highest difference is from southern directions and the lowest from northern. At future climates the difference decreases from northern directions yet increases from southern directions, e.g. at 2100 climate I_A is 49% higher from south-east. At inland and Lapland, the I_A is significantly lower from southern directions at present climate, e.g. 2.3 and 3.5 times lower, respectively, from south-west direction. At future climates the

difference decreases at both locations, e.g. from south-west direction at 2100 climate the I_A is 2.1 and 3.0 times lower, respectively, compared to the coastal area.

Figure 7 shows wind direction related relative change of the I_A compared to present climate.

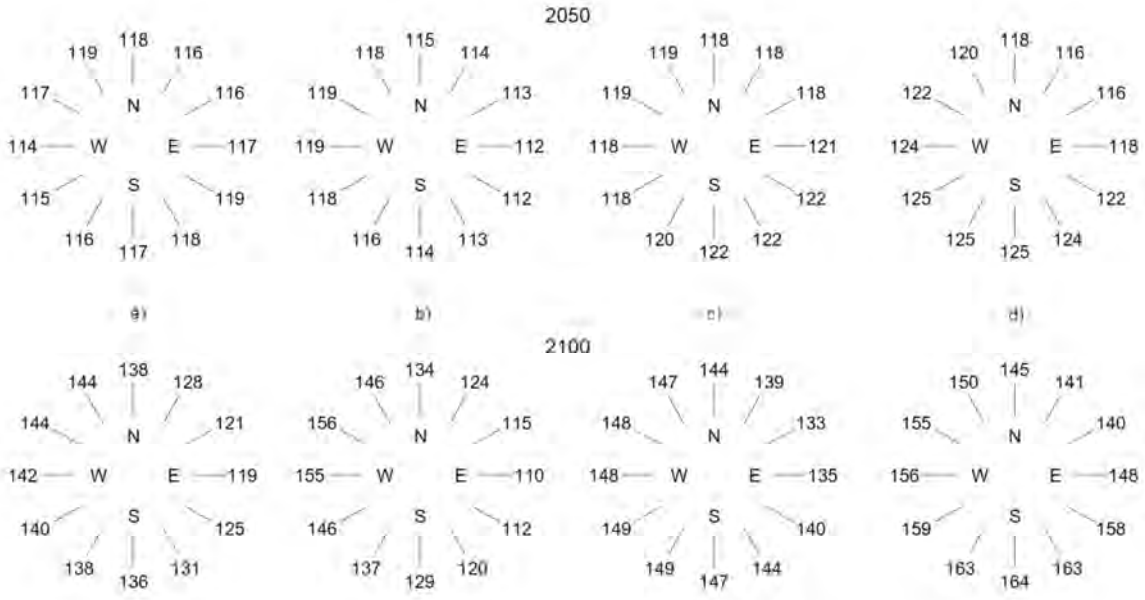

Figure 7 – Relative change of I_A *at 2050 and 2100 projected climate compared to the present climate from different wind directions at a) coastal area, b) southern Finland, c) inland and d) Lapland.*

The I_A will increase on average 34% at coastal area, 31% at southern Finland, at inland 44% and at Lapland 54% by the end of the century. At the same time the amount of precipitation increases 34%, 33%, 47% and 58%, respectively, which indicates that the wind speed during the rain events is not increasing significantly at any location. At coastal area and southern Finland, the increase of I_A concentrates southern, western and northern winds. At inland and Lapland, the I_A will increase quite evenly from all direction. As a result, south-west, south and south-east facing facades will face the most of the raining events still at future climate.

The study showed that the height of the building does not have significant impact on the amount of the Wall annual index (I_{WA}), see equation 1. At the top 2.5 m of 8-storey building an increase of the I_{WA} compared to 4-storey building is 19%. At the lower parts of the facades the I_{WA} is in practice the same.

The figures 8, 9, 10 and 11 present the I_{WA} on facades at typical Finnish suburban surroundings. The figure 8 presents the effect of variable locations on the I_{WA} on southern facades. As can be seen, at the most stressed point at the top corner of façade at Lapland, the I_{WA} level is almost at the same level (23 mm) as it is at the least stressed point at coastal area (15 mm). At coastal area, southern Finland and inland the most stressed points are facing annually WDR 70 mm, 52 mm and 34 mm, respectively. The figures also show that the lower parts of facades at inland and Lapland will face less than 10 mm of WDR annually.

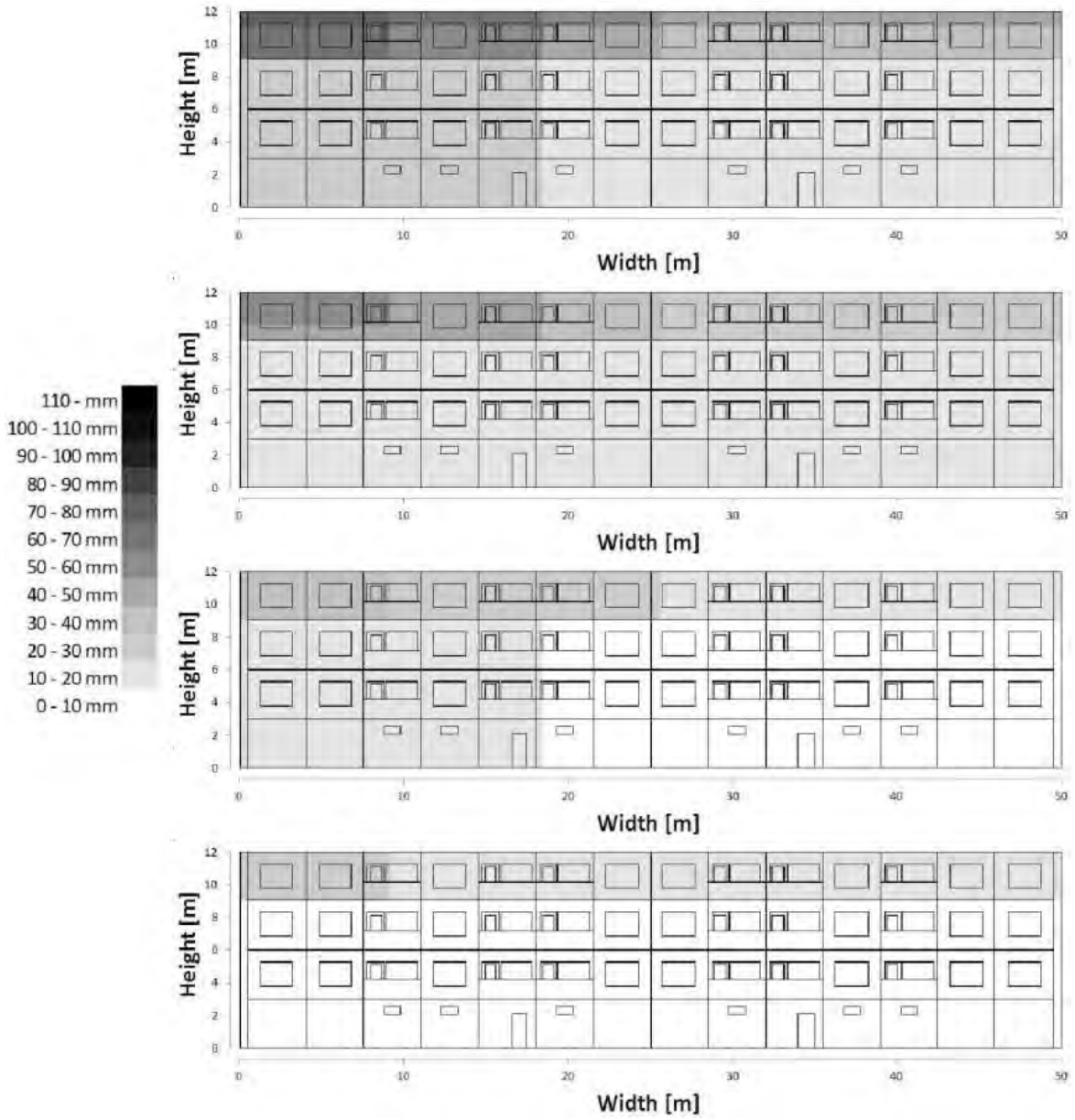

Figure 8 – The I_{WA} *on southern facades at current climate at coastal area, southern Finland, inland and Lapland.*

The figure 9 presents the effect of variable climate projections on the I_{WA}. As can be seen, at the most stressed point at the top corner of façade the I_{WA} is increasing while at the other parts of the façade the increase of the I_{WA} is not equally notable. The increase at the top part of the façade is 15 to 25 mm reaching maximum value of 95 mm while at lower parts the increase is 5 to 10 mm.

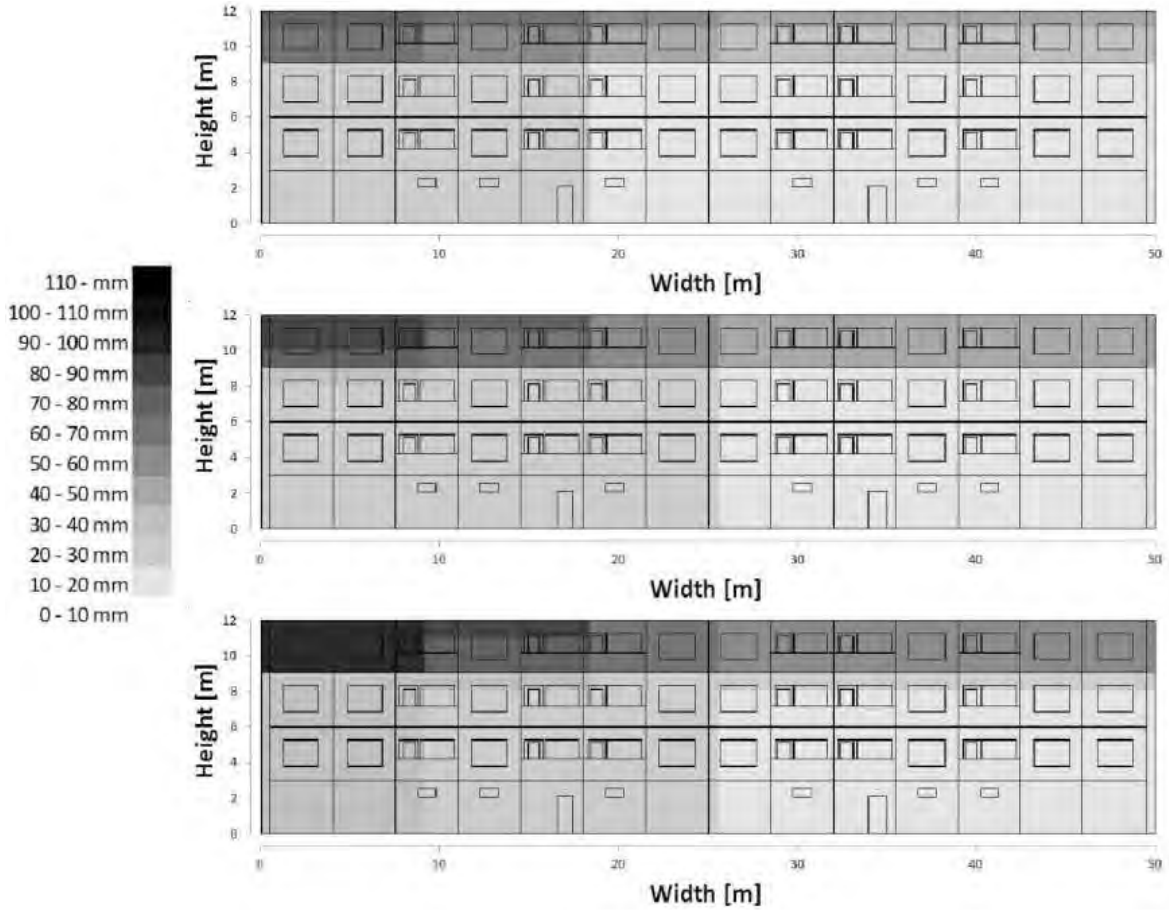

Figure 9 – The I_{WA} *on southern facades at coastal area at present, 2050 and 2100 climates.*

The figures 10 and 11 presents the effect of variable façade orientations on the I_{WA} at present and 2100 climates, respectively, at coastal area. As can be seen, even at coastal area the I_{WA} is at present almost negligible at lower parts of the northern façade and also most of the eastern and western facades. Still at 2100 the lower parts of the northern and eastern façades will face very small amounts of wind-driven rain. At the most stressed parts, i.e. at the top corners of all the facades, the I_{WA} stress level will increase quite evenly in the future climates.

At all studied climate projections the I_{WA} on the southern façade at Lapland and eastern and western facades at inland are quite similar to the northern façade at coastal area.

If the studied suburban area is thought to be by the sea or at lake shore and thus the terrain category, see table 1, is lifted to the category *I*, the increase of the I_{WA} is 48% at the top part of the façade, 57% at 8 metres from the ground and 25% at the lower parts of the facade.

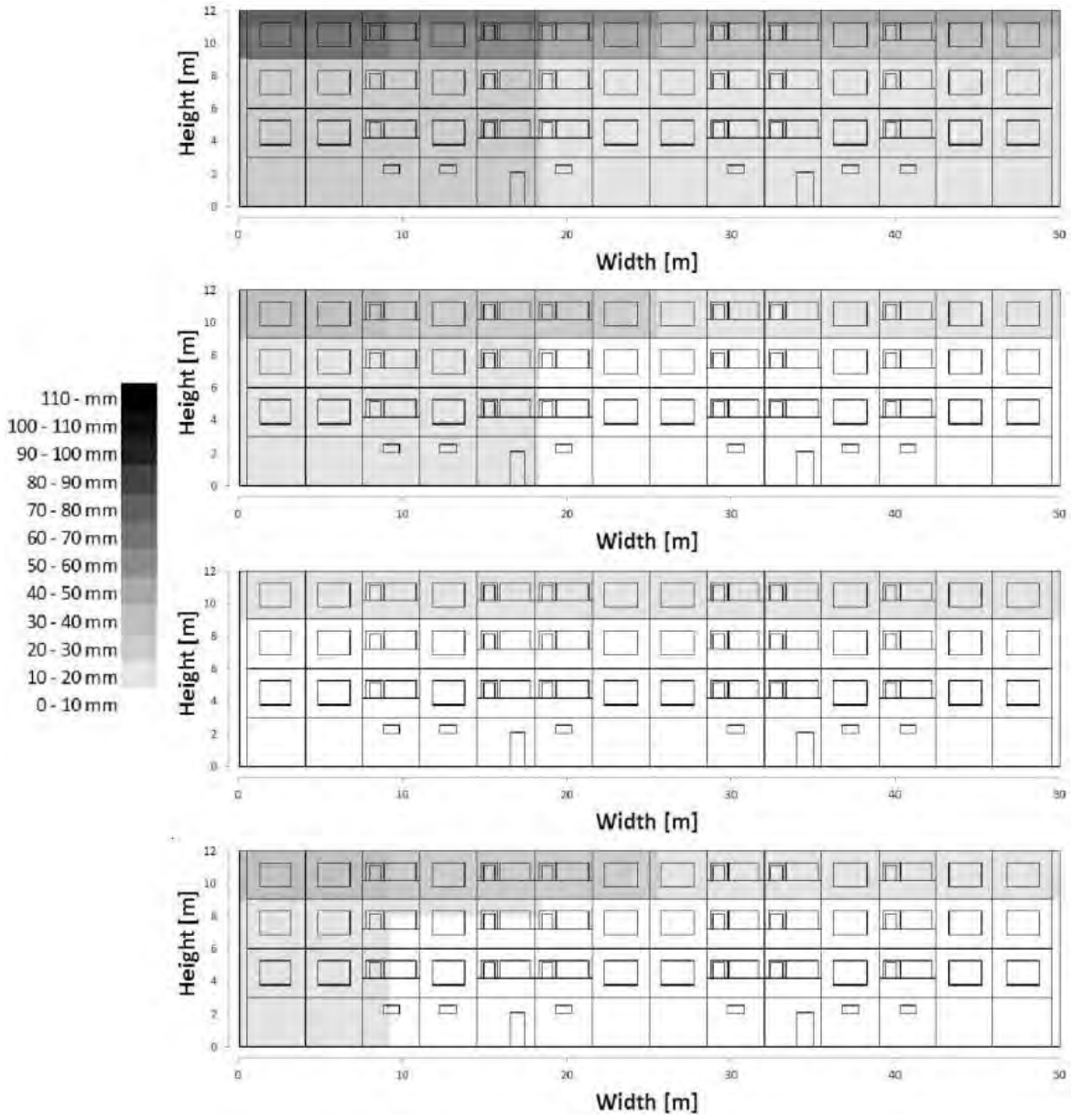

Figure 10 – The I_{WA} *on southern, western, northern and eastern facades at coastal area at present climate.*

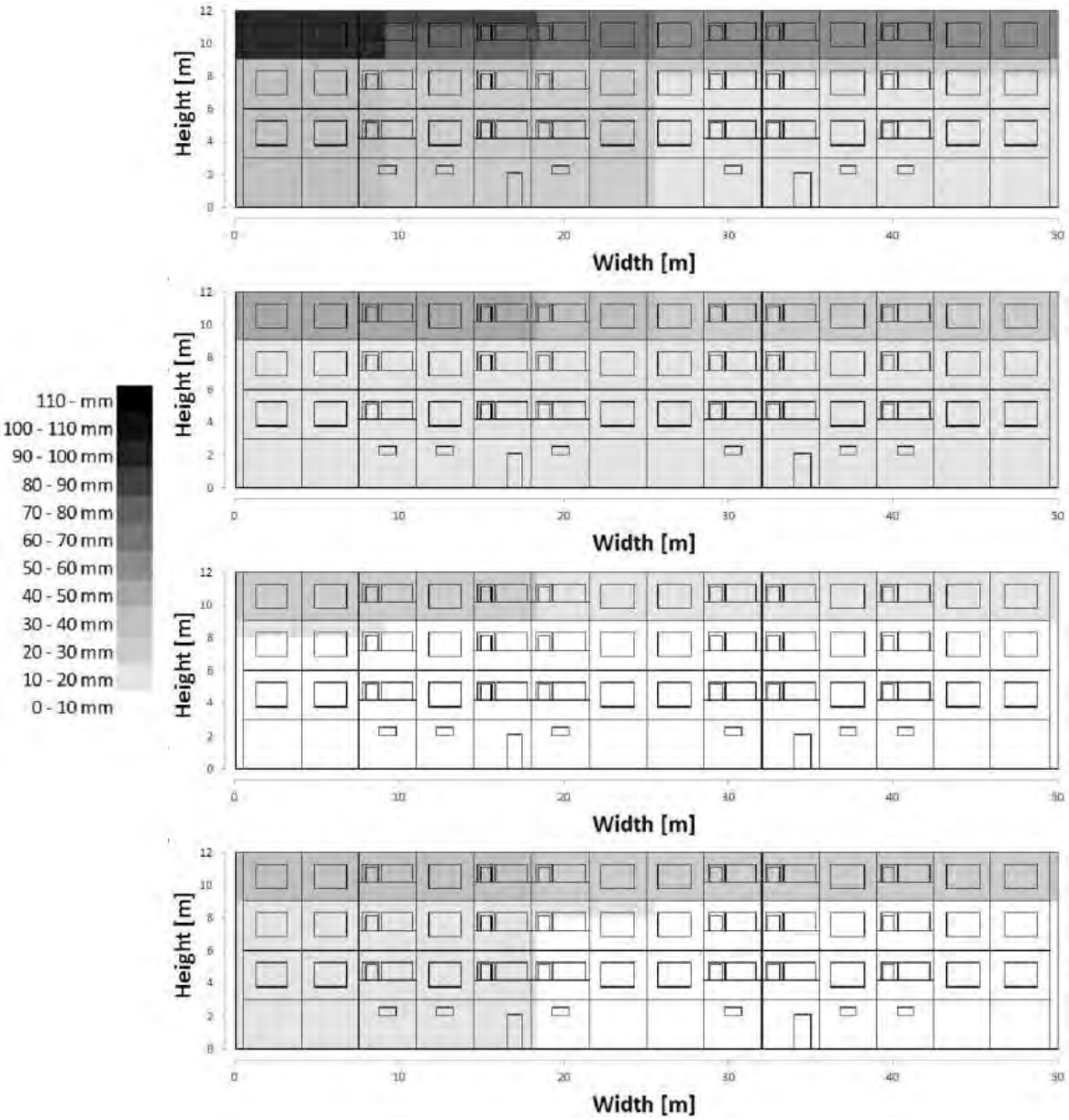

Figure 11 – The I_{WA} *on southern, western, northern and eastern facades at coastal area at 2100 climate.*

6 CONCLUSIONS

Wind-driven rain (WDR) has been noted to have a major effect on most of deterioration mechanisms of outdoor concrete structures. This study focused on determining the effect of location and climate change on the amount of the WDR on concrete façades at Finland. The calculations were based on the factors the Airfield annual index I_A and the Wall annual index I_{WA} presented at the standard SFS-EN ISO 15927 [25] at four different locations: coastal area, southern Finland, inland and Lapland. However, it should be noted that a substantial part of the Finnish building stock is located at coastal and southern Finland areas.

In Finland a direction of the WDR is highly orientated at southern wind directions depending only slightly on the location. However, a magnitude of the I_A and its dependence of the wind direction are highly connected to the location. The I_A at coastal area is 24% higher than at

southern Finland, 64% higher when compared to inland and 135% higher when compared to Lapland. At the same time the I_A is at coastal area is 354% higher from south than north while e.g. at Lapland the difference is 148%. The difference of amount of precipitation at different locations is not significantly differing but the higher wind speed during rain events causes considerable higher I_A at coastal area.

Based on the future climate projections, the I_A will increase significantly at every location and from every direction. At coastal area and southern Finland, the increase is the highest from already highly stressed directions from west to south. At inland and Lapland, the increase is quite even from every direction. By the end of the century, increase will be 34% at coastal area, 31% at southern Finland, 44% at inland and 54% at Lapland.

In addition to the I_A, the I_{WA} which takes into account also e.g. the surrounding terrain, topography and obstacles. When studying a type of a typical Finnish suburban multi-storey residential building at quite sheltered location, the I_{WA} is very low at northern facades at every location. Evidently most stressed parts of the facades are the top corners of the southern facades where the I_{WA} can be over 10 times higher than at the northern facades.

The wall annual index is highly simplified simulation for assessing the WDR against building facades. However, it gives adequate results for e.g. comparing different locational effects on the amount of wind driven rain on facades. Compared to e.g. CFD modelling it underestimates the amount of wind driven rain near the top of the façade and near the edges of the building but overestimates the amount on the top 2.5 metres with high buildings and low rain intensity.

The aim of this research was to study the orientation and location dependence of WDR and the effect of climate change on the amount of WDR. The results will be used to consider what are the possible actions to take the WDR and its orientation dependence into account at design process and whether the possible changes should be taken into account on Finnish building codes, e.g. increasing need for sheltering or better material properties.

7 ACKNOWLEDGEMENTS

The authors would like to thank the researchers at the Finnish Meteorological Institute for preparing the future climate projections.

REFERENCES

1. OSF, Official Statistics of Finland: www.tilastokeskus.fi (in Finnish), Reference date May 2nd 2016.
2. Lahdensivu, J., Varjonen, S and Köliö, A.: “Repair Strategies of Concrete Facades and Balconies” (in Finnish), Research report 148, Tampere University of Technology, Department of Civil Engineering, 2010.
3. Lahdensivu, J.: “Durability Properties and Actual Deterioration of Finnish Facades and Balconies”, Tampere University of Technology, Faculty of Built Environment, Tampere, Publication 1028, 2012, 117 p. 37 app.
4. Pakkala, T.A., Köliö, A., Lahdensivu, J. and Kiviste, M.: ”Durability demands related to frost attack for Finnish concrete buildings in changing climate”, *Building and Environment*, 82, (2014), Pp. 27–41.

5. Lahdensivu, J., Tietäväinen, H. and Pirinen, P.: ”Durability properties and deterioration of concrete facades made of insufficient frost resistant concrete”, *Nordic Concrete Research*, Publication no. 44, 2011, Pp. 175-188.
6. Köliö, A., Pakkala, T.A., Lahdensivu, J. and Kiviste, M.: “Durability demands related to carbonation induced corrosion for Finnish concrete buildings in changing climate”, *Engineering Structures* 62-63 (2014), Pp. 42–52.
7. Seppänen, M. and Koivu, T. (editors): ”BES – Development of open concrete element system” (in Finnish), Research report, Suomen Betoniteollisuuden Keskusjärjestö ry, 1970, 88 p.
8. Blocken, B. and Carmeliet, J.: “A review of wind-driven rain research in building science”, *Journal of Wind Engineering and Industrial Aerodynamics*, Volume 92, Issue 13 (2004), Pp. 1079–1130.
9. Jerling, A. and Schechninger, B.: “Fogars beständighet. Byggforskningrådet” (in Swedish), Rapport R89:1083, Stockholm, 1983, 172 p.
10. Lahdensivu, J., Mäkelä, H. and Pirinen, P.: ”Durability properties and deterioration of concrete balconies of inadequate frost resistance”, *International Journal of Sustainable Building Technology and Urban Development*, 4:2 (2013), Pp. 160–169.
11. Blocken, B. and Carmeliet, J.: “High-resolution wind-driven rain measurements on a low-rise building – experimental data for model development and model validation”, *Journal of Wind Engineering and Industrial Aerodynamics*, Volume 93, Issue 12 (2005), Pp. 905–928.
12. Lacy, R.E. and Shellard, H.C.: “An index of driving rain”, *Meteorological Magazine 91*, 1962, Pp. 177–184.
13. Rydock, J.P., Lisø, K.R., Førland, E.J., Nore, K. and Thue, J.V.: “A driving rain exposure index for Norway”, *Building and Environment* 40 (11), 2005, Pp. 1450–1458.
14. Rydock, J.P.: “A framework for using a present weather observation method to calculate a driving rain wall factor at any location”, *Building and Environment* 42 (2007), Pp. 1229–1235.
15. Pérez, J.M., Domínguez, B., del Coz, J.J. and Cano, E.: “Optimised method for estimating directional driving rain from synoptic observation data”, *Journal of Wind Engineering and Industrial Aerodynamics*, Volume 113, 2013, Pp. 1–11.
16. Choi, E.C.C.: “Parameters affecting the intensity of wind driven rain on the front face of a building”, *Journal of Wind Engineering and Industrial Aerodynamics*, Volume 53, 1994, Pp. 1–17.
17. Künzel, H.M.: “Bestimmung der Schlagregenbelastung von Fassadenfläschen” (in German), IBP Mitteilung 21, Nr. 263, 1994, Fraunhofer Institute für Bauphysik.
18. Karagiozis, A., Hadjisophocleous, G. and Cao, S.: “Wind driven rain distributions on two buildings”, *Journal of Wind Engineering and Industrial Aerodynamics*, Volume 67 and 68, 1997, Pp. 559–572.
19. Choi, E.C.C.: “Wind driven rain on building faces and the driving-rain index”, *Journal of Wind Engineering and Industrial Aerodynamics*, Volume 79, 1999, Pp. 105–122.
20. van Mook, F.J.R.: “Driving Rain on Building Envelopes”, Eindhoven University of Technology, Eindhoven, the Netherlands, PhD Thesis, 2003, 198 p.
21. Nore, K., Blocken, B., Jelle, B.P., Thue, J.V. and Carmeliet, J.: “A data set of wind driven rain measurements on low-rise test building in Norway”, *Building and Environment* 42 (2007), Pp. 2150–2165.
22. Zhu, D., Mallidi, S.R. and Fazio, P.: “Quantitative driving rain exposure on vertical wall at various Canadian cities”, *Building and Environment* 30 (1995), Pp. 533–544.
23. Fazio, P., Mallidi, S.R. and Zhu, D.: “A quantitative study for the measurement of driving rain exposure in the Montreal region”, *Building and Environment* 30 (1995), Pp. 1–11.

24. Rydock, J.P.: “A look at driving rain intensities at five cities”, *Building and Environment* 41 (2006), Pp. 1860–1866.
25. SFS-EN ISO 15927-3:2009: “Hygrothermal performance of buildings. Calculation and presentation of climatic data. Part 3: Calculation of a driving rain index for vertical surfaces from hourly wind and rain data”, Finnish Standards Association SFS, Helsinki.
26. Blocken, B. and Carmeliet, J.: “Overview of three state-of-the-art wind-driven rain assessment models and comparison based on model theory”, *Building and Environment*, Volume 45 (2010), Pp. 691–703.
27. Blocken, B., Dezsö, G., van Beeck, J. and Carmeliet, J.: “Comparison of calculation models for wind-driven rain deposition on building facades”, *Atmospheric Environment*, Volume 44 (2010). Pp. 1714–1725.
28. Jylhä, K., Ruosteenoja, K., Räisänen, J., Venäläinen, A., Tuomenvirta, H., Ruokolainen, L., Saku, S., Seitola, T.: ”The changing climate in Finland: estimates for adaption studies. ACCLIM project report 2009” (in Finnish, extended English abstract), Finnish Meteorological Institute, Reports 2009:4, Helsinki. 78 p. 36 app.
29. Vinha, J., Laukkarinen, A., Mäkitalo, M., Nurmi, S., Huttunen, P., Pakkanen, T., Kero, P., Manelius, E., Lahdensivu, J., Köliö, A., Lähdesmäki, K., Piironen, J., Kuhno, V., Pirinen, M., Aaltonen, A., Suonketo, J., Jokisalo, J., Teriö, O., Koskenvesa, A. and Palolahti, T.: ”Effects of Climate Change and Increasing of Thermal Insulation on Moisture Performance of Envelope Assemblies and Energy Consumption of Buildings” (in Finnish), Tampere University of Technology, Department of Civil Engineering, Research report 159, 2013, 354 p. + 43 app.
30. IPCC: “Climate Change 2007: The physical science basis. Contribution of Working Group I to the Fourth Assessment Report of the Intergovernmental Panel on Climate Change”. Cambridge University Press, Cambridge, U.K., 2007, 996 p.
31. Ruosteenoja, K., Jylhä, K., Mäkelä, H., Hyvönen, R., Pirinen, P. and Lehtonen, I.: “Weather data for building physics test years in the observed and projected future climate” (in Finnish), Reports No. 2013:1, Finnish Meteorological Institute, Helsinki, 2013, 36 p. 9 app.
32. Aaltonen, J., Hohti, H., Jylhä, K., Karvonen, T., Kilpeläinen, T., Koistinen, J., Kotro, J., Kuitunen, T., Ollila, M., Parvio, A., Pulkkinen, S., Silander, J., Tiihonen, T., Tuomenvirta, H. and Vajda, A.: ” Heavy rains and floods in urban areas” (in Finnish), Finnish Environment Institute 31/2008, Helsinki, 123 p.

Parallel Plate Based Measuring System for the ConTec Viscometer – Rheological Measurement of Concrete with D_{max} 32 mm

Jon E. Wallevik
Dr.ing., Senior research engineer
Innovation Center Iceland
Arleynir 2-8
IS-112 Reykjavik
Iceland
E-mail: jon.w@nmi.is

ABSTRACT

The purpose of the ConTec viscometers is to retrieve information about the rheological properties of the cement based material in terms of fundamental physical quantities. Assuming Bingham behavior, this means retrieving the yield stress and plastic viscosity. In particular, the ConTec BML Viscometer 3 and its successor, namely the ConTec Viscometer 5, are designed to measure such properties of the fresh concrete, with maximum aggregate size up to about 22 mm in diameter. The aim of the current work is to report an ongoing development of a new viscometric system for the ConTec Viscometer 5, which is in part based on the parallel plate system. The purpose of this new system is to be able to measure the rheological properties of the fresh concrete with larger aggregate size, or up to 32 mm (or even more), without having to increasing the quantity of the test sample too much. The current article reports the ongoing development of this device, here named the Coplate 5 – Mark III.

Key words: Rheology, Very large aggregate size, Viscometric development, Numerical simulation.

1. INTRODUCTION

The current project dates back to late 2001/early 2002, where the Coplate 5 (Mark I) geometry was being considered [1]. There, the aim was to reduce a so–called barrier restraint made by the coaxial geometry and thus reduce gravel migration made by such phenomenon [1]. At that time, this new geometry was designated as the C3P2–system, which is an acronym for Cone, Coaxial Cylinders and Parallel Plate–system (see [1]; Section 10.3.7). Here, the designation “Coplate 5” will be used instead of C3P2 [2]. In this work, the Mark III version of Coplate 5 system is reported and the numerical software used for the flow simulation of this version is the VVPF 1.02, in which most of it was developed in the late 2001/early 2002.

Traditionally, the ConTec viscometers [3] consist of a rotating outer cylinder and a stationary inner cylinder that measures torque. For the Bingham model, the torque values T [Nm] are time independent, only changing as a function of rotational frequency f_o [rps] of the outer cylinder.

For such a case, one can connect the measured torque values with one straight line. The slope of such line H_{cylinder} and its point of intersection with the ordinate G_{cylinder} can be converted into fundamental physical quantities, namely plastic viscosity μ and yield stress τ_0 through the well–known Reiner–Riwlin equation [4] (see also [1]; Section 3.3). However, with the Coplate 5 system, which consists of an entirely different viscometric geometry, no algebraic equation of the same type as the Reiner–Riwlin equation can be formed. The workaround this problem is a subject of the current article.

2. SIMULATION OF FLOW FOR THE COPLATE 5 – MARK III

The Coplate 5 device (Mark III) is shown in Fig. 1. The whole top unit consists of protruding vanes, where its edge consists of a cone–coaxial–paralell plate shaped tip. The space between each protruding vanes are such to accommodate for the presence of 32 mm (or larger) aggregates. The (black) bucket is wider and less deep relative to what is traditionally used for the ConTec viscometers (i.e. the Coplate bucket has a larger radius and smaller height). The bucket consists of protruding vanes (or ribs) both at the wall boundary (i.e. at the sides) as well as at the bottom plate of the bucket.

Figure 1 – The Coplate 5 system – Mark III. All interior of the bucket (black) as well as the whole top unit (grey) consists of protruding vanes to avoid slippage. Fig. 2 shows the relative position of these two units during a rheological test.

For a viscoplastic material, it is assumed that the material is held in the space between the vane blades so that the material and the vanes together behave like a rigid solid. Experimental observation supports this assumption and is in accordance with the findings made in [5,6,7]. Hence, any attempt to investigate the flow between the vane blades is not done in this work. By the above-mentioned approach, it is the test material that will form the viscometric geometry. That is, it is the extremities of the vanes in the bucket and of the whole top unit that defines the solid boundary. This approach leads to a larger cohesion (or stickiness) between the geometry (i.e. the top unit and the bucket) and the test material in-between and therefore reduces the danger for slippage.

As shown in Fig. 2, it is the whole top unit that is submerged into the concrete and registers torque T. At the same time, the bucket (black color) rotates at predetermined rotational frequencies f_o. Since the atmospheric air does not apply any stress to the concrete surface, the traction $\mathbf{t}$ at that boundary has to be set as zero. This results in the boundary condition $\partial\mathbf{v}/\partial z = 0$, where $\mathbf{v}$ is the velocity and z is elevation (see [1], Section 8.3.1). This is the same as the full-slippage boundary condition. Since all solid boundaries (i.e. top unit and bucket) consist of

protruding vanes, the condition at these borders are safely set as no–slip. In some rheometers [8], the full–slippage condition is assumed to be valid at solid boundaries by applying smooth walls. This is dangerous as different concrete batches will have different degree of stickiness on a smooth surface and thus in effect, create a variable degree of slip, which will change the assumed flow (for further readings, see [1], Section 10.3.4).

By enforcing the no-slip boundary condition with protruding vanes as is done in this work (see Fig. 1), one can be confident that the imposed boundary condition made in the numerical simulation corresponds to what is present during the actual measurement of fresh concrete. Unfortunately, this setup generates a rather complex flow behavior, resulting in that an algebraic equation cannot be formed to convert the measured data into fundamental physical quantities, for example to the yield stress τ_0 and plastic viscosity μ. That is, a new type of "Reiner–Riwlin"–equation cannot be obtained for the Coplate 5 system. Therefore, an alternative approach to this must be made, explained shortly.

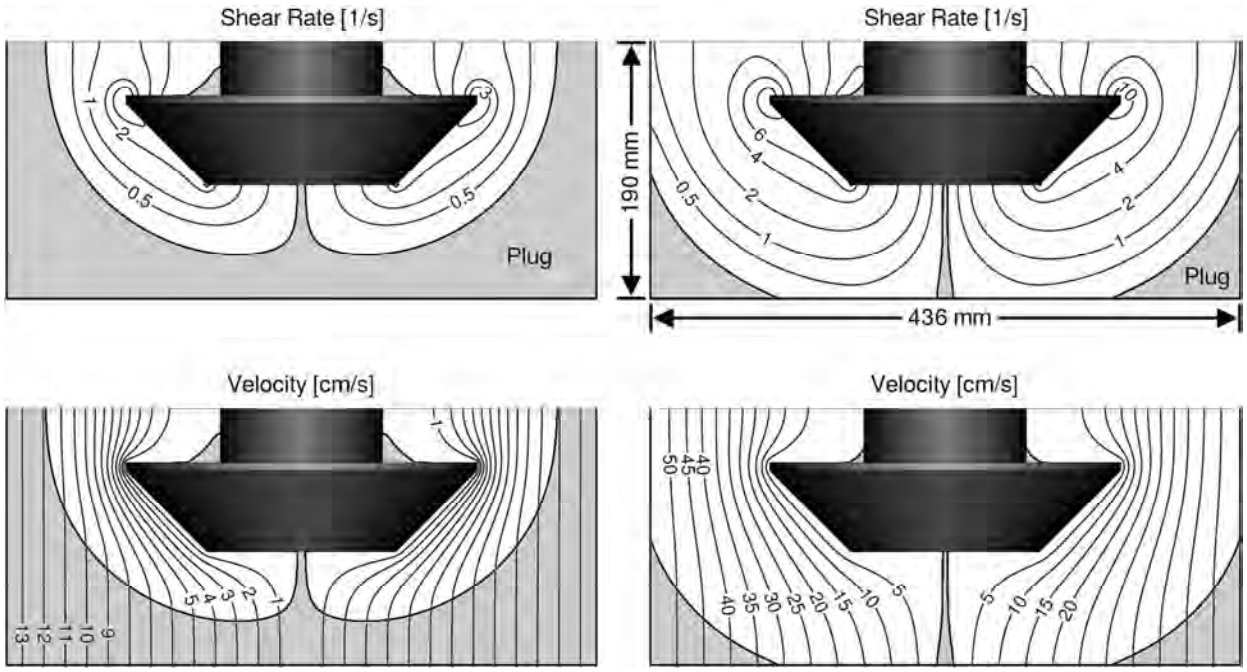

Figure 2 – Example of simulation results by VVPF 1.02, with τ_0 = 120 Pa and μ = 80 Pa·s. To the left, the rotational frequency is f_o = 0.1 rps, while to the right it is f_o = 0.4 rps. Dimensions are relative to the extremities of the protruding vanes/ribs (c.f. Fig. 1).

As mentioned before, the simulation software used here is the Viscometric–ViscoPlastic–Flow 1.02, or VVPF 1.02. The version 1.0 is almost the same as 1.02, in which the former can be freely downloaded from www.vvpf.net. The software is written in Fortran 90 [ANSI X3.198–1992; ISO/IEC 1539–1:1991 (E)]. Since there is already an extensive information available about the software (i.e. the mathematics, boundary conditions, solution area and so forth), it is not repeated here. The information is available in [1], namely in Chapter 7, Section 10.3.7 and Appendix A.3, and can be obtained from www.diva-portal.org. In short, the software VVPF 1.02 calculates the flow by using the Newton's second law (see [1], Page 16), assuming viscoplastic material behavior. Here, the Bingham model is used since it is commonly agreed that the fresh concrete can with good accuracy be considered as such [9,10,11,12]. But other types of viscoplastic models can also be used in VVPF 1.02, like the Herschel-Bulkley model or the modified Bingham model [13]. Strictly speaking, the numerical framework is in 2D,

meaning that the active coordinates are height z and radius r. However, since cylindrical coordinate system is applied, the θ–direction is also implicitly active to account for the circular geometry of the Coplate 5 system. Thus, a "semi 3D" framework is utilized. The governing equation and constative model in such system is shown in [1], Section 7.2. The results produced by the software VVPF have been demonstrated to be accurate. First of all, the numerical results produced by the software have been tested against known solutions existing in the literature (for coaxial cylinders- and parallel plates case). Also, issues like consistency, convergence, numerical convergence and stability have been dealt with, to verify a good numerical quality. For further information, see [1], pp.163-164, pp.177-203, p.258.

In Fig. 2 are shown examples of simulation results. These applies for the case of τ_0 = 120 Pa and μ = 80 Pa·s. For the two illustrations to the left, the rotational frequency is f_o = 0.1 rps, while to the right it is f_o = 0.4 rps. The larger plug zone (i.e. rigid body rotation) should be noted in the left illustrations relative to the right one. That is, the effect of plug is included in the overall analysis.

The measured rheological data by the Coplate 5 are the G and H values with the physical units of Nm and Nm·s, respectively. These are generated by measuring the applied torque T on the top unit (gray color in Fig. 1) at different rotational frequencies f_o of the bucket (black color in Fig. 1), starting from 0.4 rps down to 0.1 rps, in several steps. The measured torque values are curve fitted by linear regression with a straight line. The resulting slope is the H value and its point of intersection with the ordinate is the G value.

As mentioned before it is not possible to form an algebraic equation that can convert the above G and H values over to fundamental physical quantities, in this case to the yield stress τ_0 and plastic viscosity μ. However, an alternative route is possible to this consisting of doing series of simulations in such manner that the G and H values can be mapped over to the yield stress τ_0 and plastic viscosity μ. More precisely, for given values of yield stress τ_0 and plastic viscosity μ, number of four simulations are made at f_o = 0.1, 0.2, 0.3 and 0.4 rps. These four simulations will give four different torque values T_1, T_2, T_3 and T_4, respectively (applied on the whole top unit). Thereafter, one can curve fit these torque values with one straight line, in which the slope is H and the point of intersection with the ordinate is G. Thus, with one such set of simulations, a correlation is made between a specific values of yield stress τ_0 and plastic viscosity μ over to specific G and H values. By repeating this step for wide variety of yield stresses τ_0 and plastic viscosities μ, one can generate a systematic map between $\tau_0 - \mu$ and $G - H$. Example of such is shown in Fig. 3.

In this work, the simulations are divided into two parts, namely a *low yield series* and a *medium yield series*. For the former, the yield stress τ_0 is changed stepwise from 0, 20, 40,... up to 200 Pa (11 cases). For each such case, the plastic viscosity μ is changed in steps from 20, 40,... up to 180 Pa·s (9 case). For each single case of yield stress τ_0 and plastic viscosity μ, four simulations are performed at different rotational frequencies f_o (namely at 0.1, 0.2, 0.3 and 0.4 rps, c.f. the above text). Thus, the total number of simulations done for the low yield series is $11 \cdot 9 \cdot 4 = 396$. For the medium yield series, the yield stress τ_0 is increased from 200, 240,... up to 600 Pa (11 cases). For each such case, the plastic viscosity μ is changed in steps from 20, 60,... up to 180 Pa·s (5 cases), which means $11 \cdot 5 \cdot 4 = 220$ simulations. Thus, the total number of simulations is $396 + 220 = 616$.

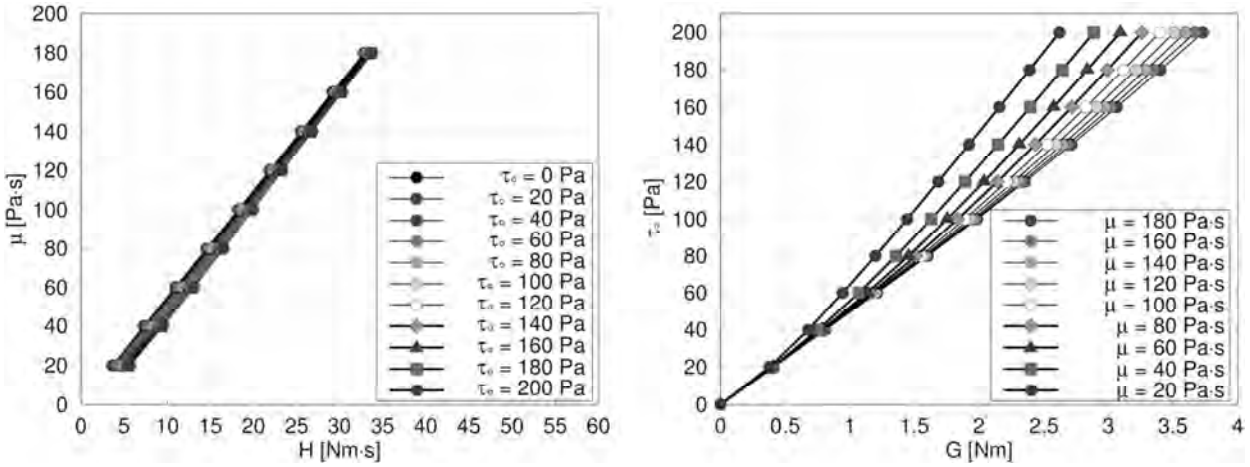

Figure 3 – Mapping of G and H values to yield stress τ_0 and plastic viscosity μ.

Manually starting and stopping each simulation 616 times, as well as making the necessary analysis for each case, would be too time consuming and costly. Therefore, a script file was written in Python (www.python.org) that did most of this automatically. In Fig. 3, the simulation results for τ_0 between 0 to 200 Pa and μ between 20 to 180 Pa·s, is shown (i.e. the low yield series). The (roughly) one–to–one relationship between μ and H obtained in the left illustration is important. Without this, it is difficult to get a plastic viscosity μ value from the measured H value and thus a yield stress τ_0 from the measured G value, thereafter. A better explanation of the procedure is given in the next section.

3. EXPERIMENTAL

Several tests have been made with the Mark III version of the Coplate 5 system. These are of different mortar batches D_{max} = 8 mm, as well as of different concrete batches, either with the (nominal) maximum aggregate size D_{max} of 16 mm or of 32 mm. As shown in Fig. 4, for each rheological test, two ConTec Viscometer 5 devices are used, placed side by side. One has the Coplate 5 system mounted on (shown in the left illustration of Fig. 4), while the other has the coaxial cylinders system mounted on (the right illustration). Thus, during the comparison tests, the exactly same batch, at the exact same age (i.e. time from water addition), is tested. The aim of the project is having the two devices giving the same rheological results in terms of fundamental physical quantity, namely in terms of yield stress τ_0 and plastic viscosity μ.

As an example of experimental result from the Coplate 5 (of concrete with D_{max} = 16 mm), measured values are H = 14.9 Nm·s and G = 2.38 Nm. The process of converting these into plastic viscosity μ and yield stress τ_0 is shown in Fig. 5: The starting point is in Fig. 5a, in which the measured value H = 14.9 Nm·s is allow to intersect the main line which then intersects into Fig. 5b, giving μ = 78 Pa·s (the pre-mentioned main line is an average line of all the simulated lines of the left illustration). By using the value μ = 78 Pa·s, one can choose the relevant line in the right illustration shown with Fig. 5c. Thereafter starting with G = 2.38 Nm in Fig. 5d, crossing the relevant line, one ends with τ_0 = 137 Pa in Fig. 5e. Thus, the measured values H = 14.9 Nm·s and G = 2.38 Nm corresponds to μ = 78 Pa·s and τ_0 = 137 Pa in fundamental units.

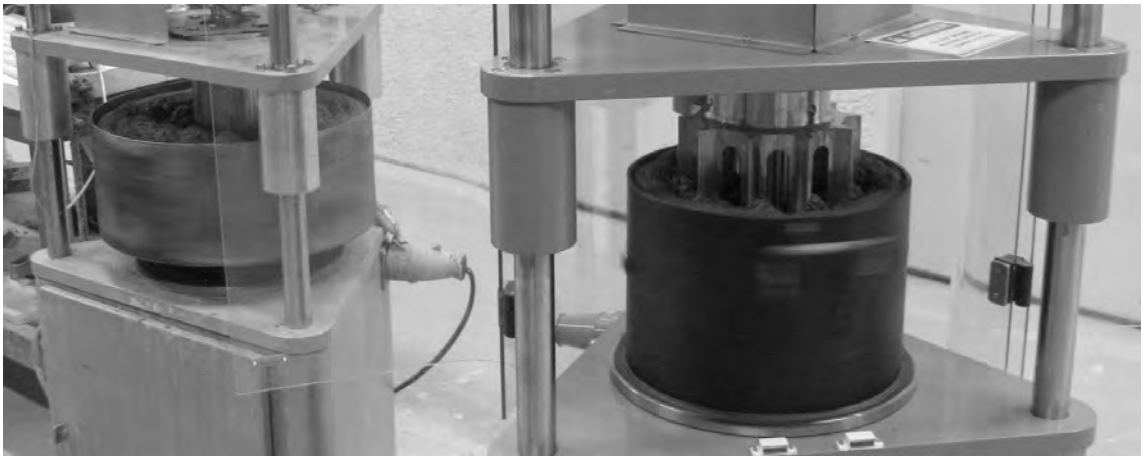

Figure 4 – Simultaneous testing of the Coplate 5 system (to the left) and of the coaxial cylinders system (to the right).

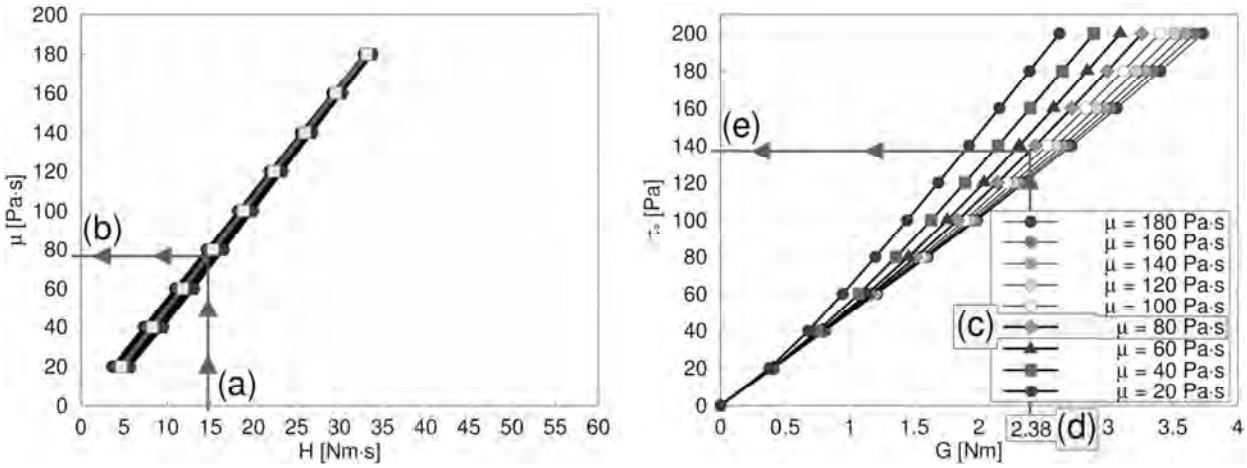

Figure 5 – Conversion of G and H into yield stress τ_0 and plastic viscosity μ (from Fig. 3).

If the obtained plastic viscosity value from Fig. 5b is between simulated points, say μ = 68.5 Pa·s, the corresponding yield stress τ_0 is found by linear interpolation of the data shown in the right illustration of Fig. 5.

One should note that when extracting the plastic viscosity μ from the H value (Fig. 5a-b), there is a certain degree of uncertainty involved. This is because all the simulated lines in the left illustration of Fig. 5 do not completely overlap one another. For the above example, the possible plastic viscosity values that can be extracted from H = 14.9 Nm·s is between about 70 to 83 Pa·s. One could use an iterative approach where the initial yield stress τ_0 = 137 Pa is used to choose a better plastic viscosity line in the left illustration of Fig. 5 (using the legend in the left illustration of Fig. 3), and repeat the operations Fig. 5a–e in such manner, several times. But such approach may or may not converge. This method is considered for future research.

During the comparison tests between the Coplate 5 and the coaxial cylinders system (c.f. Fig. 4), only mortar (with D_{max} 8 mm) and concrete (with D_{max} 16 mm) are tested. When testing concrete batches using maximum aggregate size of D_{max} of 32 mm, a parallel run with the coaxial cylinders system is not possible due to lack of sufficient space for the largest aggregates. Thus, when testing concrete with D_{max} = 32 mm, only the Coplate 5 system is applied. An example of mixing and testing of such is illustrated in Fig. 6. As shown in the left and center illustrations, the largest aggregates are of elongated shape (high aspect ratio), with one

dimension much larger than 32 mm. Thus in effect, a larger aggregate size than 32 mm is being used in this work.

Although no comparison can be made for large aggregate cases, such tests have an important purpose. With the previous version of the Coplate 5 system, namely the Mark II, the flow condition during a rheological test was such that the measurement was obviously unreliable, with largest aggregates bouncing of the viscometric bucket by some unwanted and extreme particle-particle interactions. The Mark II version of the Coplate 5 is basically the same as Mark I, except that the bucket has similar dimensions as shown in Fig. 1. During testing of the Mark II, it became clear that viscometric testing of concrete with very large aggregate size is not straightforward. Therefore, one of the test criteria of the current work is a "*smooth run*" during each viscometric test.

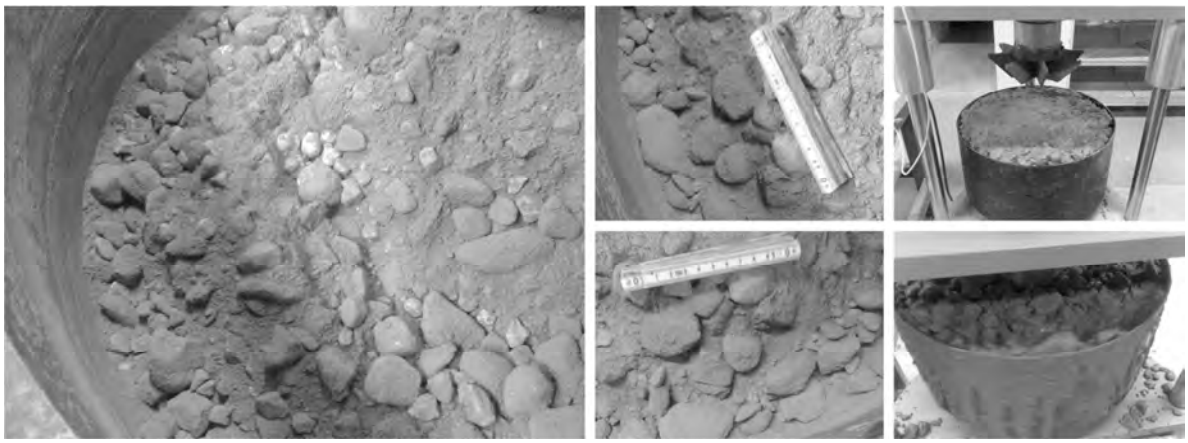

Figure 6 – Dry mixing of concrete using D_{max} = 32 mm (left and center) and testing of such in the Coplate 5 – Mark III, system (to the right).

Suffice to say, the flow condition with the current new geometry, namely the Mark III, showed a good flow condition and a *smooth run* in which the largest aggregates ($\geq$ 32 mm) participated in the flow as shown in the right illustration of Fig. 6 (just as one would observe for the 16 mm aggregates in the coaxial cylinders system). Example of measured values of the above concrete type are G = 7.5 Nm and H = 40.0 Nm·s, resulting in τ_0 = 449 Pa and μ = 202 Pa·s in fundamental units, which represents a rather unworkable concrete. A more flowable concrete of this type would consist of τ_0 = 179 Pa and μ = 58 Pa·s in fundamental units, which corresponds to the measured values G = 2.8 Nm and and H = 11.4 Nm·s.

4. RESULTS AND DISCUSSION

Fig. 7 shows experimental results of concrete ($D_{\max}$ = 16 mm) and mortar ($D_{\max}$ = 8 mm) during comparison tests between the Coplate 5 system and the traditional coaxial cylinders system. To reiterate, exactly the same batch at the exactly the same state is simultaneously tested in both systems. This is possible since two ConTec Viscometers 5 were available in the research, previously shown in Fig. 4.

For the left illustration of Fig. 7 (i.e. the yield stress), the correlation coefficient R^2 is 0.97 for the mortar, while 0.99 for the concrete. For the right illustration of Fig. 7 (i.e. the plastic viscosity), the correlation coefficient R^2 is 0.86 for the mortar, while 0.90 for the concrete. Thus in terms of correlation coefficient, and relative to the current available data, a good agreement is

obtained between the coaxial cylinders systems and the Coplate 5 system.

When doing a visual comparison, with the one-to-one line in mind shown in each illustration of Fig. 7, one can see that the Coplate 5 system is generally creating higher plastic viscosity values for concrete, while lower values for mortar. Still, the average difference in plastic viscosity between the two devices is only about 18%. The average difference for the yield stress is lower, or 10%. This last mentioned value is mostly due to the higher difference for the very high yield stress cases shown in the center of Fig. 7 (i.e. in the small incorporated figure). In terms of coaxial cylinders system (with the Reiner-Riwlin equation), these are τ_0 = 937 Pa and μ = 50 Pa·s for the first point and τ_0 = 1024 Pa and μ = 47 Pa·s for the second point. For these two points, the average difference in yield stress τ_0 between the Coplate- and coaxial system is 21%. This difference could be related to the fact that the Coplate 5 data processing includes the effect of plug (see Fig. 2), while the coaxial cylinders system (with Reiner-Riwlin) dose not. As explained in [1] (Section 3.5.3), for the latter device, if the effect of plug is not accounted for, it will result in lower yield stress than actual value as well as higher plastic viscosity than actual.

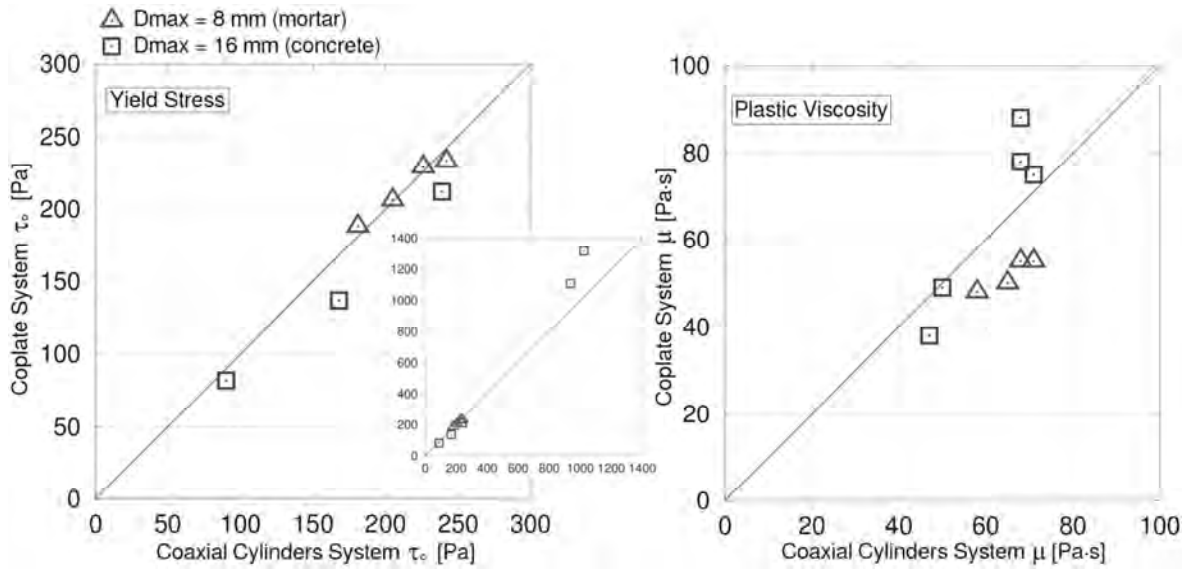

Figure 7 – Comparative test of the Coplate 5- and the coaxial cylinder system (see Fig. 4).

Another issue could contribute to the difference between the Coplate 5- and the coaxial cylinders system for the above-mentioned two high yield stress cases: The simulation of the medium yield series (Section 2) goes only up to 600 Pa. This means that higher yield stress values of the Coplate 5 system are obtained by extrapolating existing medium data series. Such, could introduce a certain error in the conversion between $G - H$ and $\tau_0 - \mu$. Therefore, increasing the simulated data set and generate a high yield series in the same manner as low yield- and medium yield series (explained in Section 2) is considered for future work.

4. CONCLUSIONS

By doing a series of numerical simulations, it is possible to generate a systematic map between $\tau_0 - \mu$ and $G - H$ for the Coplate 5 system (Mark III). With this, the measured data, G and H values can be converted into fundamental physical quantities, namely the yield stress τ_0 and plastic viscosity μ. The effect of plug flow is automatically included in the analysis, meaning that neither the obtained yield stresses nor the plastic viscosities are distorted by such flow

phenomenon.

Relative to the current set of measured data, almost the same rheological values are obtained for the Coplate 5 system as for the traditional coaxial cylinders system. More precisely, only about 10% difference (in the average) is registered for the yield stress τ_0, while 18% difference for the plastic viscosity μ. When considering other work of the same type [14], it is clear that the above difference is a minor one. However, as this research continues and the measured data set increases, this difference will likely change.

ACKNOWLEDGMENTS

This work is based on previous research done at the Norwegian University of Science and Technology (NTNU), sponsored by Borregaard LignoTech, Norway and the Research Council of Norway (NFR). The further development of the Coplate 5 system has been sponsored by the Housing Financing Fund (www.ils.is), Innovation Center Iceland (www.innovation.is) and ConTec Ltd. (www.contec.is).

REFERENCES

1. Wallevik, J.E., "Rheology of particle suspensions – fresh concrete, mortar and cement paste with various types of lignosulfonates", Ph.D. thesis, *Department of Structural Engineering, The Norwegian University of Science and Technology*, Trondheim, 2003, *http://ntnu.diva-portal.org/smash/record.jsf?pid=diva2:124984&rvn=1*
2. Wallevik, J.E., "Development of parallel plate-based measuring system for the ConTec Viscometer", *Proceedings of the 3rd International RILEM Symposium on Rheology of Cement Suspensions such as Fresh Concrete*, August 19-21, 2009, Reykjavik, Iceland, RILEM Publications S.A.R.L., ISBN: 978-2-35158-091-2.
3. *www.contec.is*
4. Reiner, M., "Deformation and flow; an elementary introduction to theoretical rheology" *H.K. Lewis & Co. Limited*, Great Britain, 1949.
5. Yan, J., James, A.E., "The yield surface of viscoelastic and plastic fluids in a vane viscometer", *J. Non-Newtonian Fluid Mech.* 70, 1997, 237 – 253.
6. Keentok, M., Milthorpe, J.F., O'Donovan, E., "On the shearing zone around rotating vanes in plastic liquids: Theory and experiment", *J. Non-Newtonian Fluid Mech.* 17, 1985, 23 – 35.
7. Barnes, H.A., Nguyen Q.D., "Rotating vane rheometry - a review", *J. Non-Newtonian Fluid Mech.* 98, 2001, 1 – 14.
8. Hu, C., de Larrard, F., Sedran, T., Boulay, C., Bosc, F., Deflorenne, F., "Validation of BTRHEOM, the new rheometer for soft-to-fluid concrete", *Mater. Struct.* 29:194, 1996 620 – 631.
9. Tattersall, G.H., Banfill, P.F.G., "The rheology of fresh concrete", *Pitman Books Limited*, Great Britain, 1983.
10. Tattersall, G.H., "Workability and quality control of concrete", *E & FN Spon*, London, Great Britain, 1991.
11. Tattersall, G.H., Bloomer, S.J., "Further development of the two–point test for workability and extension of its range", *Mag. Concr. Res.* 31:109, 1979, 202 – 210.
12. Domone, P.L.J., Yongmo, X., Banfill, P.F.G., "Developments of the two–point workability test for high–performance concrete", *Mag. Concr. Res.* 51:3, 1999, 171 – 179.

13. Feys D., Wallevik J.E., Yahia A., Khayat K.H., Wallevik O.H., “Extension of the Reiner-Riwlin equation to determine modified Bingham parameters measured in coaxial cylinders rheometers”, *Mater. Struct.* 46, 2013, 289 – 311.
14. Banfill, P.F.G., Beaupre, D., Chapdelaine, F., de Larrard, F., Domone, P., Nachbaur, L., Sedran, T., Wallevik, O.H., Wallevik, J.E., “Comparison of Concrete Rheometers: International Tests at LCPC (Nantes, France) in October, 2000 (NISTIR 6819)”, Editors: F. Ferraris and L. E. Brower, *National Institute of Standard and Technology (NIST)*, Gaithersburg, USA, 2001.

Carbonation Characterization of Mortar with Portland Cement and Fly Ash, Comparison of Techniques

Andres Belda Revert
M.Sc., PhD candidate
Norwegian University of Science and Technology (NTNU),
Department of Structural Engineering
Rich. Birkelandsvei 1 A, 7491. Trondheim
andres.b.revert@ntnu.no

Klaartje De Weerdt
PhD, Associate Professor
Norwegian University of Science and Technology (NTNU),
Department of Structural Engineering
Rich. Birkelandsvei 1 A, 7491. Trondheim
klaartje.d.weerdt@ntnu.no

Karla Hornbostel
PhD, Postdoctoral researcher
Norwegian University of Science and Technology (NTNU),
Department of Structural Engineering
Rich. Birkelandsvei 1 A, 7491. Trondheim
karla.hornbostel@ntnu.no

Mette Rica Geiker
PhD, Professor
Norwegian University of Science and Technology (NTNU),
Department of Structural Engineering
Rich. Birkelandsvei 1 A, 7491. Trondheim
mette.geiker@ntnu.no

Abstract

The aim of this paper is to investigate the applicability of selected techniques for the characterization of carbonation in mortar samples: pH indicators (phenolphthalein and thymolphthalein), thermogravimetric analysis, X-ray diffraction, analyses of thin sections and polished sections. The results obtained by the different techniques on two mortars (w/b= 0.55; Portland cement (CEM I) and Portland fly ash cement (CEM II/B-V)) exposed to accelerated carbonation (20^{o}C, 60% RH and 1.5% CO_2) were compared. Spraying with a pH indicator and treating the data by image analysis provides characterisation of the carbonation depth which is in agreement with the other investigated techniques and data on the spatial variation of the carbonation depth.

Key words: Carbonation, Portland fly ash cement, pH indicators, TGA, XRD, optical microscopy, SEM

1. INTRODUCTION

Carbonation-induced corrosion causes premature deterioration of reinforced concrete structures. Carbonation is the spontaneous reaction between the CO_2 present in the air and the cement paste. Carbonation causes, among others, a drop in the pH of the pore solution. Steel embedded in carbonated concrete is not passivated and may corrode [1].

Carbonation is a stepwise reaction which causes gradual changes in the cement paste. First CO_2 is dissolved in the pore solution and carbonic acid is formed. The carbonic acid reacts with the Ca ions from the different cement phases to form calcium carbonate (C$\underline{\text{C}}$). Portlandite (CH) is the first phase to react, followed by monosulphate and ettringite. Calcium silicate hydrate (C-S-H) starts to release calcium once CH is consumed [2]. Carbonation of C-S-H seems to follow two steps: first calcium from the interlayer and defect sites is consumed and once the Ca/Si ratio is 0.67, the calcium from the principal layers is consumed and amorphous silica gel is formed [3]. Additionally, unhydrated phases as alite and belite may carbonate [4].

Table 1 gives an overview of the techniques found in the literature to study carbonation in cementitious materials. The techniques are briefly described below.

The most common way to measure the carbonation depth in concrete is to spray a pH indicator on a freshly split surface and measure the depth at which a colour change takes place. Typically phenolphthalein (PHE) has been used (see e.g. EN 13295:2003 [5]). However, PHE was classified as potentially carcinogenic by the Norwegian Environment Agency in 2015 [6], and alternative indicators are being introduced. Thymolphthalein was observed to give similar results as PHE, see e.g. [7], or [8] where the same materials as used in the present paper were used.

Spraying with a pH indicator allows determination of the depth at which the pH of the pore solution changes in the range of the used pH indicator. If more detailed information is required the actual pH of the pore solution (PS) can be determined. The pH of the pore solution is usually measured on pressure extracted pore solution samples by the use of a pH electrode, see e.g. [9, 10]. McPolin et al. [11] measured the pH of the pore solution with a fibre optic sensor using based on sol-gel technology using either fluorescence life time measurements or absorbance measurements.

Carbonation can be characterized by thermogravimetric analysis (TGA) on homogenized profile ground samples. The monitoring of weight changes while heating up the samples allows the quantification of compounds with known thermal reaction such as the dehydroxilation of CH or the decarbonation of C$\underline{\text{C}}$. In the case of C$\underline{\text{C}}$ the decarbonation temperature varies depending on the polymorphs which are formed [12]. C$\underline{\text{C}}$ present in concrete arrives from different sources: the binder, the aggregates and carbonation.

Fourier-transform infrared spectroscopy (FTIR) allows detecting carbonation by studying the characteristic absorption frequencies of carbon-oxide bonds. Changes reflect the carbonation of CH to form C$\underline{\text{C}}$ [13, 14].

Table 1- Techniques used to detect changes due to carbonation in cementitious materials. Materials (Mat): C: Concrete, M: mortar, P: paste. Exposure: N: natural. Binder: Portland Cement (PC) or PC blends: FA: fly ash, MK: metakaolin, MS: microsilica, NP: natural pozzolan, S: slag. Abbreviations of the techniques are explained in the text. For overview, the techniques used in the present paper are also included [(*)].

First author and reference	Year	Mat	Binder		Exposure			pH in.	PS	TGA	FTIR	XRD	OM	SEM	TEM	MIP	ND	NMR MAS	γ–ρ	CA
			PC	Blend	T [%]	RH [%]	CO_2 [%]													
Schiessl [15]	1976	C	Not given		N (in- and outdoor)			x	x											
Tuutti [16]	1982	C, M	x	S	N (in- and outdoor)			x	x	x						x				
Litvan [17]	1986	C	x	S	N (in- and outdoor)			x		x						x				x
Parrott [18]	1989	C	Not given		N (in- and outdoor)			x		x										
Campbell [19]	1991	C	x	FA	23	50	0.03	x					x							
Papadakis [4, 20]	1991 1992	C, M	x	NP, FA	22, 30, 42	35-85	50	x		x						x				
Möller [21]	1994	C	Not given		20	30-60	0.03	x		x										x
Lo [13]	2002	C	x	-	21	-	2	x			x									
Chang [14]	2006	C	x	-	23	70	20	x	x	x	x	x								
Thiery [22]	2007	C	x	-	21	53	50	x		x									x	
Villain [23]	2007	C	x	-	20	53	45	x		x									x	x
Castellote [24, 25]	2008 2009	P	x	FA, MS	22	65	0.03, 10, 100	x		x		x				x	x	x		
Herrera [26]	2015	M	x	FA	28	60	50	x	x	x	x									
Herterich [27]	2015	P	x	FA, S	24	40, 55, 75	0.03			x	x	x			x			x		
Leemann [28]	2015	C, M	x	MS, S	20	57	4	x						x		x				
Sevelsted [3]	2015	P	Synthetic		-	100	0.03											x		
Wu [29]	2015	P	x	FA, S	20	75	3	x		x			x							
Shi [30]	2016	M	x	MK	20	57	1	x		x				x		x		x		
Belda [(*)]	2016	M	x	FA	20	60	1.5	x		x		x	x	x						

X-ray diffraction (XRD) allows the identification of crystalline phases such as CH and C$\underline{C}$ polymorphs. XRD applied to a crystalline material produces a pattern characterized by the peaks at varying intensities and diffraction angles, which are related to the crystal structures and enables its identification based on Bragg's law. When XRD is combined with Rietveld analysis the crystalline phases can be quantified [31]. Changes in crystalline phases due to carbonation can be detected.

Changes in the microstructure due to carbonation can be studied on thin sections by the use of optical microscopy (OM) with crossed polarized light. Carbonated areas appear opaline and brighter in colour, while non-carbonated areas appear in darker colours. [32] Additionally, changes in porosity can be observed by the use of fluorescent light in thin sections prepared with fluorescent dye [33].

Scanning electron microscopy with energy dispersive spectrometry (SEM-EDS) on polished sections can be applied to study carbonation of cementitious materials [34]. Differences in morphology and elemental composition can be investigated by studying the signals emitted by the electrons interacting with the atoms of the sample [30]. Changes in CH content and in the C-S-H composition due to carbonation can be investigated. However to observed changes in the C-S-H composition and morphology it is advised to use transmission electron microscopy (TEM) on ion-beam milled samples [27].

Mercury intrusion porosimetry (MIP) allows characterisation of the porosity. The connected pore volume and pore entry sizes can be characterized by MIP [35]. A non-wetting fluid (mercury) is intruded into the pore structure under increasing pressure. The intruded pore size is determined using the Washburn equation (assuming cylindrical pores) [36]. Changes in porosity due to carbonation can be investigated.

Magic-angle nuclear magnetic resonance spectroscopy (MAS-NMR) allows the identification of amorphous and crystalline phases. Depending on the nuclear-spin isotope studied, different phases can be quantified. If ^{29}Si is used, changes in the silicate chain structure of the C-S-H caused by carbonation can be investigated [37].

In addition to the above mentioned techniques, neutron diffraction (ND), see e.g. [24] or [38], and gammadensimetry (γ–ρ), see e.g. [23], have been used to study carbonation of cementitious materials. A discussion of the applicability of these methods is considered outside the scope of this paper.

Finally, chemical analysis (CA) has been applied to detect carbonation of cementitious materials: e.g. Litvan and Meyer [17] estimated the amount of C$\underline{C}$ by digestion in sulfuric acid and Möller [21] determined CH and bound CO_2 by acid digestion of ground powder dissolved in hydrochloric acid.

The aim of this paper is to investigate the applicability of selected techniques for the characterization of carbonation in mortar samples. Special emphasis is paid to the phase composition. The following techniques were investigated: pH indicators (phenolphthalein and thymolphthalein) were sprayed on freshly split samples, thermogravimetric analysis and X-ray diffraction were performed on homogenized profile ground samples, analyses of thin sections by optical microscopy and polished sections using scanning electron microscopy. The study is part of a larger project on the improvement of the carbonation resistance of low clinker blends and service life prediction, especially of fly ash blends.

2. EXPERIMENTAL

Figure 1 provides an overview of the applied experimental techniques and the sampling undertaken on the mortar prisms.

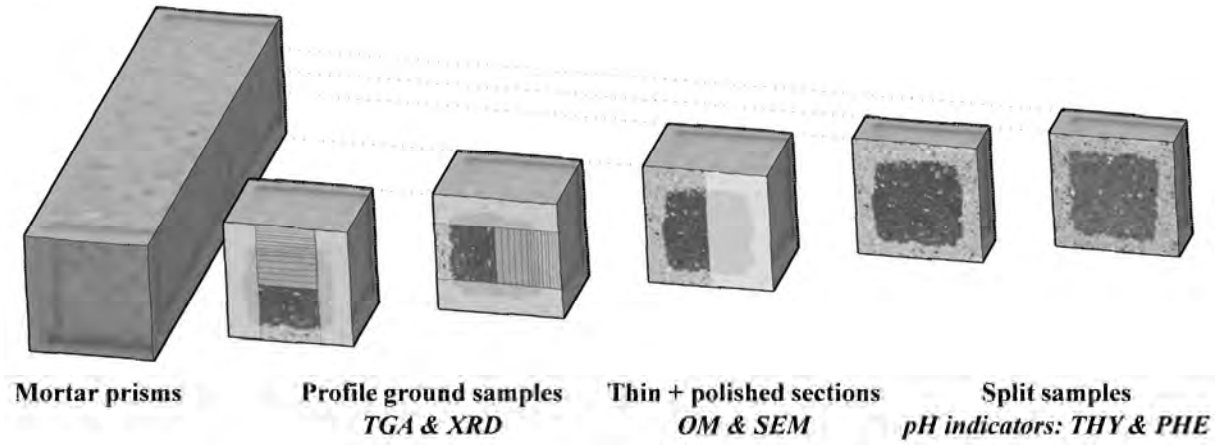

Figure 1- Overview of the used techniques and sampling on CEM I and CEM II/B-V mortar prism. The blue or pink area indicates the non-carbonated mortar identified by thymolphthalein or phenolphthalein.

2.1 *Material*

Mortar prisms 40 x 40 x 160 mm with two binders were investigated. The binders were: CEM I containing 4% limestone powder and CEM II/B-V containing 30% fly ash and 4% limestone powder. Table 2 presents the chemical composition of the binders determined by XRF. The mortar composition (water-to-binder ratio 0.55) was 450 g binder, 1350 g standard CEN sand (d_{max} 2 mm) and 247.5 g water per batch. The mortars were mixed and compacted according to EN 196 [39]. The prisms were stored in the moulds covered with a plastic wrap at 20°C for 24 hours after casting. After demoulding, the prisms were wrapped in plastic and stored at 20°C for 13 days in a sealed container.

Table 2- Chemical composition of the investigated binders determined by XRF [% by mass].

Compound	SiO_2	Al_2O_3	Fe_2O_3	CaO	MgO	SO_3	P_2O_5	K_2O	Na_2O
CEM I	20.4	4.8	3.4	61.7	2.2	3.5	0.2	0.9	0.5
CEM II/B-V	29.5	10.8	4.5	44.6	2	3.2	0.4	1.1	0.5

2.2 Exposure

Fourteen days after casting, the mortar prisms were exposed for four weeks to accelerated carbonation conditions: 20 ± 0.5°C, 60 ± 1.5% RH and 1.5 ± 0.1% CO_2. Note that the short curing period only allows for a limited degree of reaction of the fly ash [27].

2.3 *Experimental techniques*

2.3.1 pH indicators

Freshly split mortar surfaces were sprayed with PHE 1% and THY 1% solution. The solutions were prepared by dissolving 1 g of each indicator in 30 ml of deionized water and 70 ml of ethanol. Pictures were taken with a reflex camera fixed on a frame with constant light conditions. Carbonation depth was measured by image analysis using a colour thresholding principle. The differentiation of the carbonated zone and the non-carbonated zone, pinkish for PHE (pH <9.5) and blueish for THY (pH <10.5), was determined using different threshold

colour values depending on the indicator. The image analysis treatment comprised the following steps: scaling of the image, determining sample area and non-carbonated area, and measuring the carbonation depth. Thirty points were taken per side avoiding the corner effect (due to the ingress from two directions).

Additionally THY 1% was sprayed on a freshly dry cut surface instead of a split surface to allow optical microscopy investigation.

2.3.2 Thermogravimetric analysis

TGA was performed on homogenized profile ground samples. To study carbonation as a one dimensional phenomenon, the lateral sides (10 mm on each) were removed by dry cutting before profile grinding, see Figure 1. The right (R) and top (T) side were studied. The outer 0-1 mm step was omitted as different paste content was expected. The grinding step was 1 mm for the first 10 mm and 2 mm-step for the rest of the sample. The TGA was performed with a Mettler Toledo TGA/DSC 3+, on samples of approximately 300 mg loaded in aluminum oxide crucibles. The samples were heated from 40 to 900^{o}C at a rate of 20^{o}C/min while the oven was purged with N_2 at 50 ml/min. The weight loss of the samples was monitored as a function of the temperature. The amounts of CH and C$\underline{C}$ were calculated following equation (1) and (2):

$$CH\ \% = \frac{W_{400\,^{\circ}C} - W_{550\,^{\circ}C}}{W_{850\,^{\circ}C}} \cdot \frac{74}{18} \cdot 100\% \quad (1)$$

$$C\underline{C}\ \% = \frac{W_{550\,^{\circ}C} - W_{850\,^{\circ}C}}{W_{850\,^{\circ}C}} \cdot \frac{100}{44} \cdot 100\% \quad (2)$$

2.3.3 X-ray diffraction

Ground mortar samples from the carbonated area (depth 1-2 mm) were investigated by XRD. The powder was sieved (300 μm) and front loaded for analysis with a D8 DaVinci diffractometer from Bruker. The following parameters were used: angle range 7-55 $^{o}2\theta$, step width 0.01 $^{o}2\theta$, time per step 0.5 s, axial soller 2.5^{o}, rotation 30 min^{-1}, radiation 1.54 Å (Kα Cu) and generator 40/40 kV/mA.

2.3.4 Optical microscopy

Thin sections were studied by an optical microscope Nikon Eclipse LV 100 POL. CH and C$\underline{C}$ crystals were observed using crossed polarized light. Porosity changes due to carbonation were studied by comparing the intensity of the fluorescent light transmitted through the sample.

2.3.5 Scanning electron microscopy

Polished sections were investigated by a scanning electron microscope Quanta 400 ESEM from FEI, operated at high vacuum mode and accelerating voltage of 20 keV. Images were taken in back scatter electron (BSE) mode.

4. RESULTS

4.1 Terminology

Figure 2 introduces the used terminology and symbols applied in this paper:

- The carbonation depth ($x_{c,i}$) is the distance at location "i" from the outer surface inwards to which a colour change is observed on a freshly split sample sprayed with a pH indicator. The carbonation depth is described by the spatial variation:
  - Average ($\bar{x}_c$)
  - Median ($\tilde{x}_c$)
  - Range (δ_x)
- The carbonation front is the area/volume in which the measured property (e.g. pH, C$\underline{C}$ and CH content) changes due to carbonation. The carbonation front is described by its width (w_x)

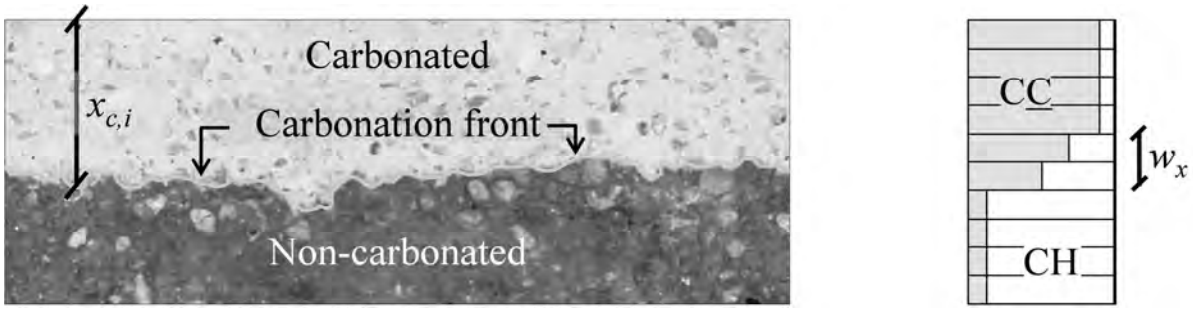

Figure 2- Used terminology to describe carbonation. Left: carbonated and non-carbonated mortar identified by pH indicator (THY); $x_{c,i}$: carbonation depth at location "i". Right: carbonation front characterized as change in CH and C$\underline{C}$ content determined using TGA; w_x: width of the carbonation front. Note that the width of the carbonation front depends on the measured property.

4.2 pH indicators

Carbonation depth estimated by the pH indicators show clear differences depending on the investigated side of the prisms: lateral and top sides showed similar carbonation depths, while the bottom side gave lower values. Similar observations were made on cut surfaces. Figure 3 illustrates the variation of carbonation depth across and along a mortar prism.

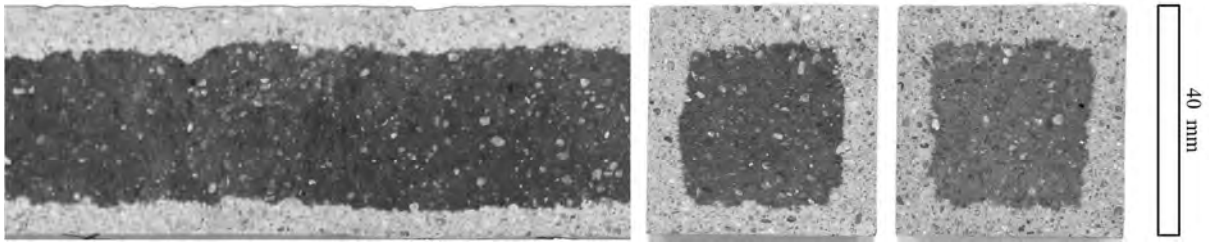

Figure 3- CEM II/B-V samples sprayed with pH indicators. Left: longitudinal section sprayed with TH. Middle: cross section sprayed with THY. Right: cross section sprayed with PHE.

Figure 4 presents the carbonation depth histograms for both mortars sprayed with THY. It can be observed that if the data is split into bottom side and the rest of the sides, then it tends to distribute as a normal distribution. In the case of the bottom side as the number of points is smaller the tendency is not as clearly observable as with the lateral and top side plot together. Data from the bottom sides are not included in this study for the comparison of the techniques.

Figure 5 illustrates the spatial variation of carbonation depth determined by the two pH indicators. Both PHE and THY showed clearly defined carbonation fronts and yielded similar

carbonation distributions. The range (δ_x) is comparable to the maximum grain size of the used aggregates (2 mm). As expected, the mortar with CEM II/B-V binder showed lower carbonation resistance compared to the mortar with CEM I. The values represent combined data from the lateral and top sides.

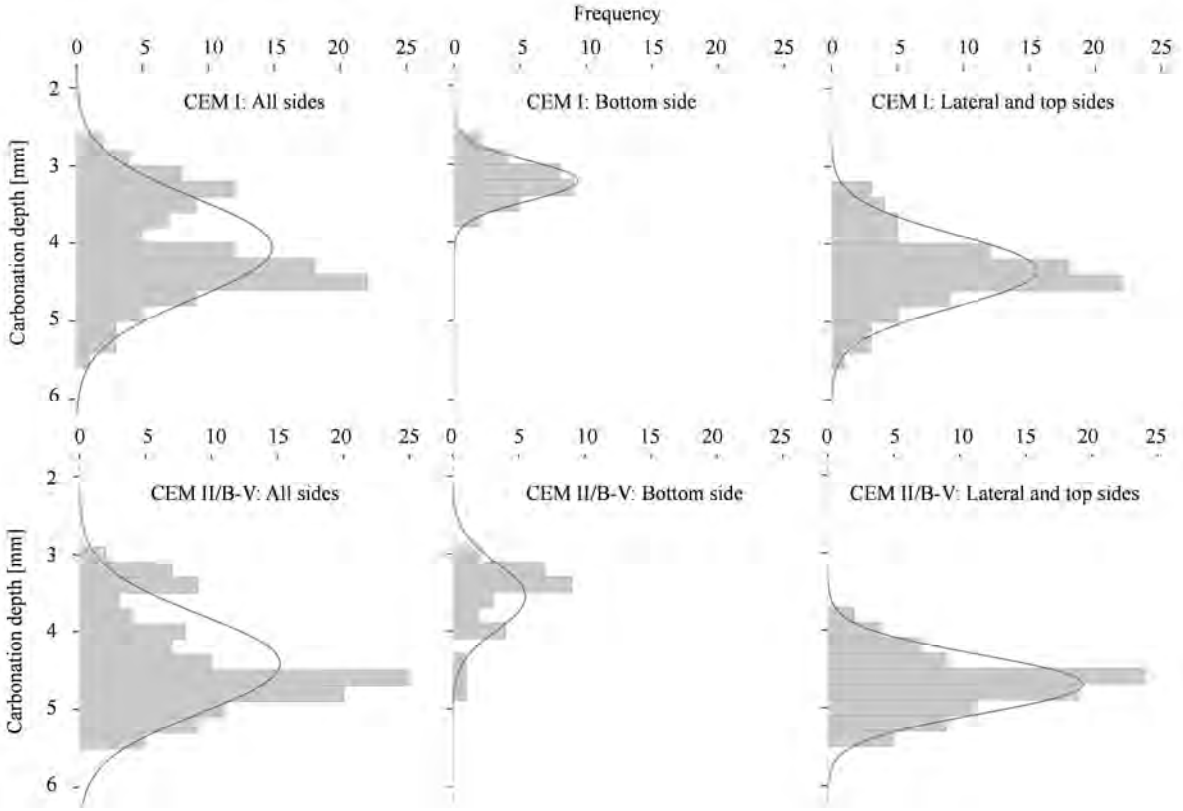

Figure 4- Histograms of CEM I and CEM II/B-V samples sprayed with THY. Left: all four sides. Middle: bottom side. Right: lateral and top sides.

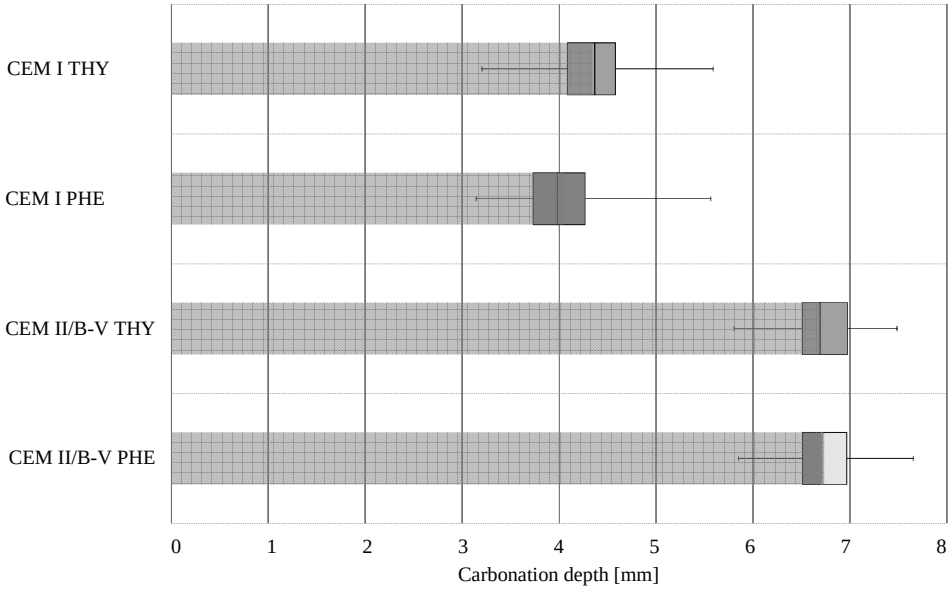

Figure 5- Spatial variation of carbonation depths: lateral and top sides of CEM I and CEM II/B-V mortar samples determined using THY and PHE. Boxes: values from the second to the third quartile and $\tilde{x}_c$, whiskers: δ_x, grey bars: $\bar{x}_c$.

4.3 Thermogravimetric analysis and X-ray diffraction

Figure 6 (left) presents an example of both mass loss and derivative curve for a non-carbonated sample (dark) and a carbonated sample (grey) determined by TGA. The carbonate peak for the carbonated sample (450-850 ^{o}C) presented different shoulders. One of the possible explanations could be the presence of different C$\underline{C}$ polymorphs. However, only calcite was observed by XRD. The broad range of decomposition temperatures for the C$\underline{C}$ can be attributed to variations in crystallinity, differences in participle size, and a large amount C$\underline{C}$ present e.g. [23, 12, 40].

Ground powder taken from the carbonated area (depth 1-2 mm) of both mortars was analysed by XRD (see Figure 6 right), in order to identify potential C$\underline{C}$ polymorphs. Three different polymorphs can be found in concrete: calcite, vaterite and aragonite [41]. Due to the presence of the sand in the ground mortar samples, the spectrum was dominated by quartz peaks, complicating the identification of other crystalline phases. Nonetheless, for both mortars, calcite was the main C$\underline{C}$ polymorph which was observed, while the presence of vaterite and aragonite could not be confirmed. No distinct diffraction peaks related to CH could be observed in the carbonated sample.

Figure 7 gives the derivative curves for the investigated depths from the right side of CEM II/B-V. The amounts of CH and C$\underline{C}$ determined by TGA on the different profile ground sections are shown in Figure 10. The typical error for the C$\underline{C}$ estimation was not larger than 0.4% points and 0.3% points for the CH estimation. The error of position is considered the grinding step; 1 mm for the first 10 mm and 2 mm for the rest of the sample.

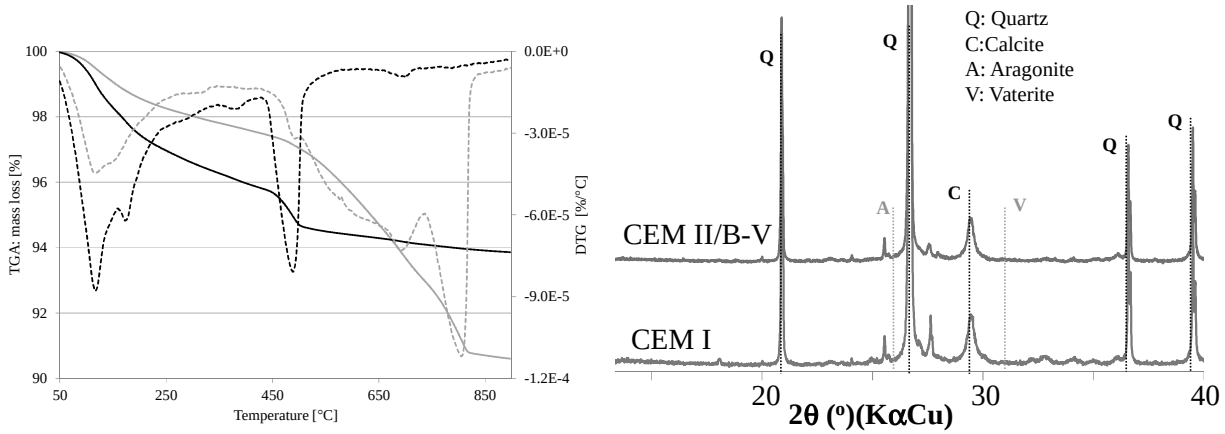

Figure 6- Left: weight loss in % of weight at 850 ^{o}C (TGA, solid) and differential weight loss (DTG, dotted) of non-carbonated sample, depth 12-14 mm (black), and carbonated sample, depth 1-2 mm (grey) of CEM I. Right: XRD pattern of the carbonated samples, depth 1-2 mm.

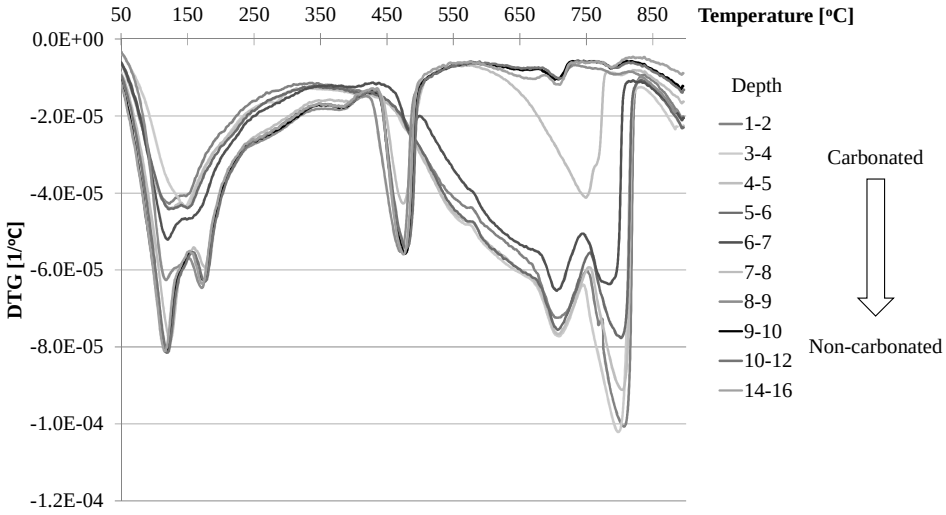

Figure 7- Differential weight loss (DTG) curves for sample CEM II/B-V right side at the different homogenized profile ground depths

4.4 Microscopy

Figure 8 presents the images taken by the optical microscope on cut sections (normal light) and thin sections (cross polarized light), and by SEM in BSE mode on polished sections. CO_2 penetrated from the top side inwards. Note that the images of the cut section give an overview of the carbonation front while the images of both the thin and the polished sections are focused on the transition from carbonated to non-carbonated mortar using higher magnification.

The normal light pictures demonstrate the sharpness of the front assessed by THY. In addition, the pictures show the spatial variation of the carbonation depth over the width of the samples and how the carbonation depth is affected by the presence of air voids and sand grains.

Under cross polarized light in the optical microscope, C$\underline{\text{C}}$ crystals were observed in the carbonated zone, rendering the paste opaline and brighter in colour. In the non-carbonated area, CH crystals were observed as bright and colourful spots in the darker surrounding sound paste. A relatively sharp transition from carbonated to non-carbonated paste was observed. In addition, the spatial variation of the carbonation front and the impact of aggregates are once more demonstrated. The range of the carbonation front determined by optical microscopy using cross polarized light is presented in Table 3.

Table 3- Carbonation depth range (δ_x) determined by optical microscopy.

	CEM I Top	CEM I Right	CEM II/B-V Top	CEM II/B-V Right
δ_x [mm]	4-5.5	3.5-4.5	6-7	6-7

Changes in the microstructure caused by carbonation were difficult to observe by the use of SEM. The absence or presence of CH indicates the position of the carbonation front. However, neither clear difference in grey tone nor morphology of hydrates could be observed between carbonated and non-carbonated paste. This is further discussed in [40]. However, Shi et al. [30] observed clear differences in the microstructure between carbonated and non-carbonated paste using SEM-BSE.

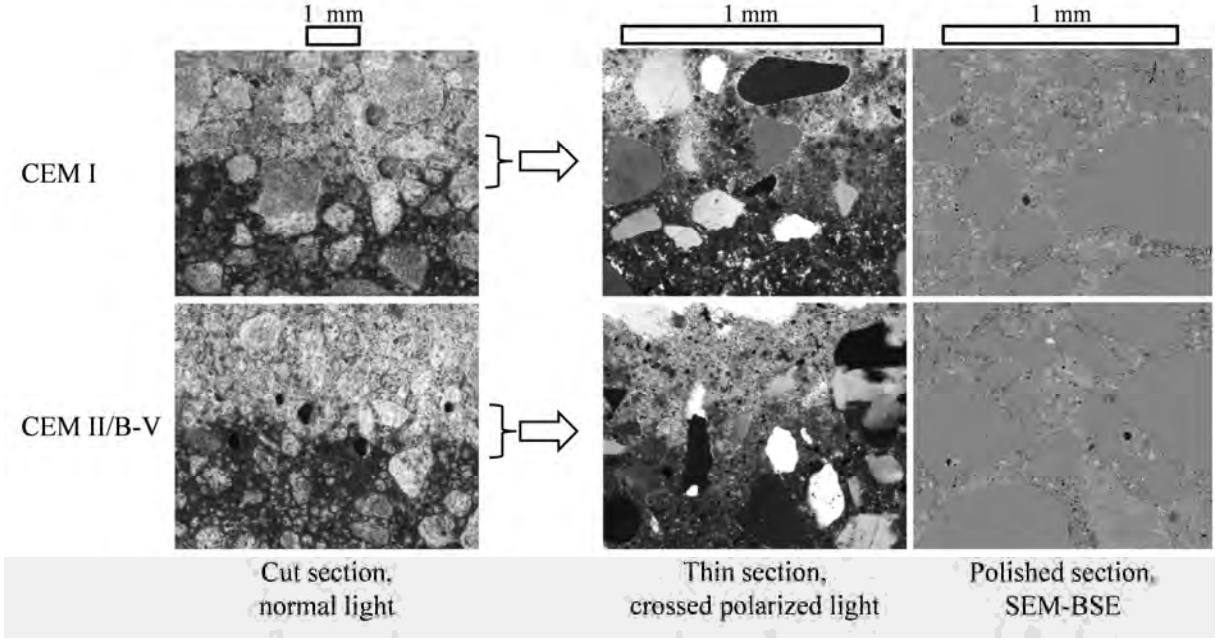

Figure 8 - Pictures taken by optical and scanning electron microscopy. Carbonation from the top side. Images of thin sections taken by Marit Haugen and images of polished sections taken by Ulla H. Jakobsen.

Figure 9 presents the images taken on the thin sections by the optical microscope using fluorescence light. The porosity, investigated using UV light transmitted through the fluorescent impregnated thin sections did not seem to be affected by carbonation for any of the mortars. The images indicated no major changes in porosity due to carbonation in any of the mortars. The darker spots observed in the thin section were due to the penetration of form oil and should not be mistaken for densifications. This is in disagreement with the expected change in porosity [1]. The w/b at 0.55 is considered at the limit to estimate changes porosity by the eye, for high w/b more sophisticated methods should be used [32, 33].

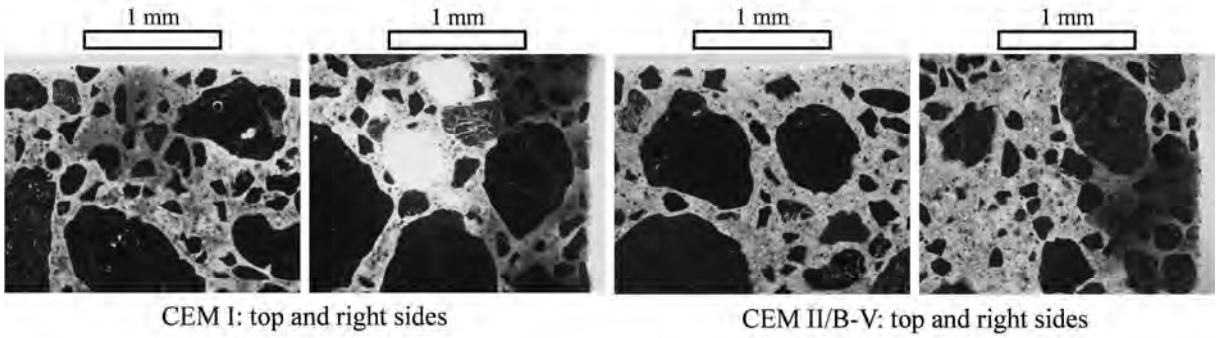

Figure 9- Pictures of carbonated mortar taken by optical microscopy with fluorescence light on the thin section. Images taken by Marit Haugen.

5. DISCUSSION

The carbonation characterization obtained by THY, TGA and optical microscopy are compared in Figure 10. For TGA, carbonation was characterized by a decrease in the CH content and an increase in the C$\underline{C}$ content. When comparing the results of the different techniques, the sampling process should be kept in mind. When profile grinding (as in the case of TGA), the content of the different phases is homogenized over the depth of the step (1 or 2 mm), thereby averaging the spatial variations. A split section (THY) or thin section, on the other hand, shows the spatial variation, but only represents a limited section of the mortar sample. Additionally, the comparison is also influenced by the spatial variation of carbonation in the longitudinal axes of the prism: each technique was applied to the same mortar sample, but on different sections (see Figure 1). From Figure 10, it can be seen that the carbonation depth determined by THY and the depth of CH depletion determined by TGA are in relatively good agreement when considering the impact of sampling. Using TGA an apparent gradual change of phases can be observed. For the CEM I mortar the width of the carbonation front determined by TGA can be explained by the spatial variation of the carbonation depth observed by THY, but could also be due to kinetics. For the CEM II/B-V mortar C$\underline{C}$ are formed at deeper depths. From Figure 10, it can also be seen that the carbonation depth determined by THY and optical microscopy are in relatively good agreement.

Chang and Chen [14] investigated concrete samples made with Portland cement with w/b=0.65 exposed to accelerated carbonation for 8 and 16 weeks (23^{o}C, 70% RH and 20% CO_2). They assumed that the carbonation depth determined by TGA was the depth where the C$\underline{C}$ content approached the bulk content of the non-carbonated material (which is deeper than the depth of CH depletion considered above). Using their definition the carbonation depth by TGA was for the investigated material and exposure found to be twice as deep compared to the one obtained with PHE. Shi et al. [30] compared PHE and TGA for mortars prepared with binders with calcined clay and limestone exposed to accelerated carbonation (20^{o}C, 57% RH and 1% CO_2). They also observed that C$\underline{C}$ were found deeper compared to the carbonation depth obtained by PHE, e.g. Portland cement mortar with limestone addition (30%) cured for 90 days showed after 90 days of exposure a carbonation depth of 8 mm determined by PHE while the plateau of the C$\underline{C}$ was found at a depth of 10 mm. Litvan and Meyer [17] observed that the C$\underline{C}$ approached the bulk content up to 15 mm inwards while the PHE colour changed was close to 5 mm in a Portland cement concrete exposed to natural carbonation for 20 years.

Comparing the TGA data for the two cements it can be observed that CH is contributing to carbonation to a larger extent in the CEM I mortar than in the CEM II/B-V mortar. The CO_2 binding capacity of the two cement types is discussed in a separate paper [40].

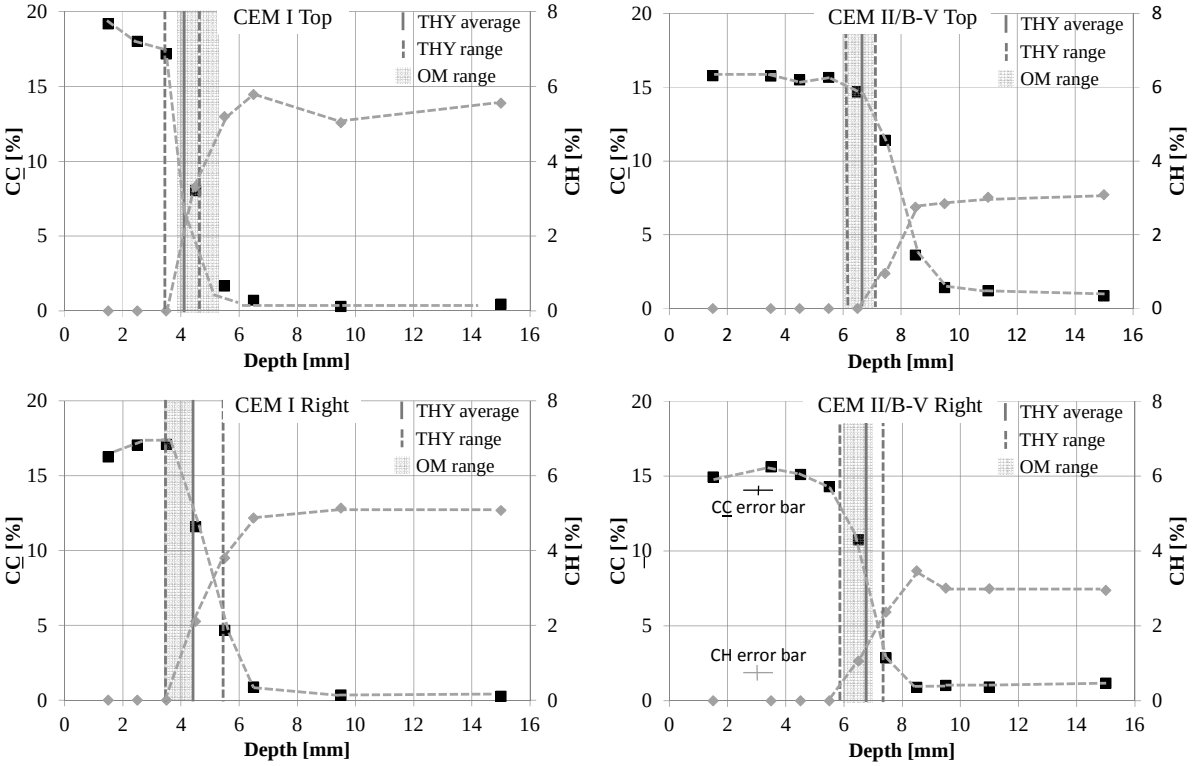

Figure 10- Carbonation characterization by the use of THY (continuous line: $\bar{x}_c$, dotted lines: δ_x), TGA (CC: squares, CH: diamonds) and optical microscopy (shady area: δ_x). The horizontal axis represents the depth (0 outer surface and positive inwards) while the vertical axis presents the CC content to the left and CH content to the right in each graph. Note the difference between the scales for CC and CH. The typical error for the CC estimation was not larger than 0.4% points and 0.3% points for the CH estimation. The error of position is considered the grinding step; 1 mm for the first 10 mm and 2 mm for the rest of the sample.

Table 4 presents a summary of the applicability of the techniques and sampling used to investigate carbonation in this study. The carbonation front seems to be steep for the examined mortars and exposure. Carbonation characterization using THY sprayed on a freshly broken surface was found to be well in agreement with the optical microscopy and thermogravimetric analysis. THY was found to be the most economic and simple technique to apply, which together with the image analysis gives statistical information for service life design.

Table 4 - Comparison of the investigated techniques. Brackets: limited information.

Technique	Measured property	Spatial variation of carbonation depth	Width of the carbonation front	Cost - Complexity
pH indicator	pH (threshold)	Yes	[Yes]	Low
TGA	CH, CC	No	Yes	Med
XRD	CH, CC polymorphs	Not investigated		Med
OM	Porosity, phases	Yes	Yes	High
SEM	Porosity, phases	[Yes]	[Yes]	High

When using carbonation data for probabilistic modelling of service life, statistical data are required. Maage and Smeplass [42] proposed to use a normal distribution for carbonation depth in connection with service life prediction. The statistical treatment of the carbonation depths determined by THY (see, Figure 4) suggests that carbonation depths are distributed in two groups for the tested materials and exposure. It was found that if lateral plus top side were plot together and the bottom side separated, each of the groups presented a normal distribution. Greve-Dierfeld and Gehlen [43] also suggested a normal distribution to be used for the carbonation depths, but including all four sides of the sample.

6. CONCLUSIONS

The following conclusions were found:

- The carbonation depth determined by the pH indicator and optical microscopy and the depth of CH depletion determined by TGA are in relatively good agreement when considering the impact of sampling.
- TGA results showed gradual changes in CH and CC. The wider width of the carbonation front detected with TGA compared with the narrower width found using the other techniques can be explained by the observed spatial variation of the carbonation depth averaged in ground samples, but could also be due to kinetics. For the CEM II/B-V mortar, a broader width of the carbonation front is observed compared to CEM I mortar.
- SEM did not allow clear identification of the carbonation depth for the examined material and exposure.
- Using a pH indicator coupled with image analysis provides statistical information on the spatial variation of the carbonation depth
- Carbonation depths in the same sample formed two normally distributed groups of data. Lateral and top sides presented higher values than bottom side.

7. FURTHER RESEARCH

In the continuation of this project, the propagation period will be studied by the use of electrochemistry measurements on embedded steel using the same binders for both accelerated and natural carbonation.

8. ACKNOWLEDGEMENTS

The authors acknowledge the Norwegian Research Council for facilitating the research (NFR project no. 235211/O30: LAVKARBSEM) and the financial support provided by the partners of the LAVKARBSEM project: Heidelberg Technology Center GmbH, Mapei AS, Norbetong AS, Norcem AS, NTNU, Rambøll Engineering AS, SINTEF Byggforsk avd Trondheim, Skanska Norge AS, Spenncon AS. Also, the authors would like to acknowledge Marit Haugen (SINTEF) and Ulla Hjorth Jakobsen (DTI) for their assistance with microscopy, and Tone Østnor (SINTEF) for the assistance with TGA.

9. REFERENCES

[1] Bertolini, L., Elsener, B., Pedeferri, P., Redaelli, E. and Polder, R., "Chapter 5: Carbonation-induced corrosion," in *Corrosion of Steel in Concrete*, Wiley-VCH Verlag GmbH & Co, Weinheim, Germany, 2013, pp. 79-91.

[2] Lagerblad, B., "Carbon dioxide uptake during concrete life cycle – State of the art," Report, Swedish Cement and Concrete Research Institute, Stockholm, 2006.

[3] Sevelsted, T. F. and Skibsted, J., "Carbonation of C–S–H and C–A–S–H samples studied by ^{13}C, ^{27}Al and ^{29}Si MAS NMR spectroscopy," Cement and Concrete Research, Vol. 71, 2015, pp. 56-65.

[4] Papadakis, V. G., Vayenas, C. G. and Fardis, M. N., "Fundamental modelling and experimental investigation of concrete carbonation," Materials Journal, Vol. 88, No. 4, 1991, pp. 363-373.

[5] EN 13295:2003: Products and systems for the protection and repair of concrete structures. Test methods. Determination of resistance to carbonation, 2003.

[6] Norwegian Environment Agency, 2015, http://www.miljodirektoratet.no/no/

[7] Yu, M.-Y., Lee, J.-Y. and Chung, C.-W., "The application of various indicators for the estimation of carbonation and pH of cement based materials," Journal of testing and evaluation, Vol. 38, No. 5, 2010.

[8] Belda, A., De Weerdt, K. and Geiker, M., "Carbonation front characterization pH color indicators," 35th Cement and Concrete Science Conference, Aberdeen, Scotland, 2015.

[9] Vollpracht, A., Lothenbach, B., Snellings, R. and Haufe, J., "The pore solution of blended cements: a review," Materials and Structures, 2015, pp. 1-27.

[10] Plusquellec, G., Geiker, M., Lindgård, J., Duchesne, J., Fournier, B. and De Weerdt, K., "Determination of the pH and the free alkali metals content in the pore solution of concrete: review and experimental comparison," To be submitted to: Cement and Concrete Research, In preparation.

[11] McPolin, D., Basheer, P., Long, A., Grattan, K. and Sun, T., "New Test Method to Obtain pH Profiles due to Carbonation of Concretes Containing Supplementary Cementitious Materials," Journal of Materials in Civil Engineering, Vol. 19, No. 11, 2007, pp. 936-946.

[12] Lothenbach, B., Durdzinski, P. and De Weerdt, K., "Chapter 5: Thermogravimetric Analysis," in *A Practical Guide to Microstructural Analysis of Cementitious Materials*, Ed(s) K. Scrivener, R. Snellings and B. Lothenbach, CRC Press, Boca Raton, United States, 2015.

[13] Lo, Y. and Lee, H. M., "Curing effects on carbonation of concrete using a phenolphthalein indicator and Fourier-transform infrared spectroscopy," Building and Environment, Vol. 37, No. 5, 2002, pp. 507-514.

[14] Chang, C.-F. and Chen, J.-W., "The experimental investigation of concrete carbonation depth," Cement and Concrete Research, Vol. 36, No. 9, 2006, pp. 1760-1767.

[15] Schiessl, P., "Zur Frage de zulässigen rissbreite und der erforder lichen betondeckung im stahlbetonbau- unter besonderer berücksichtigung der karbonatisierung des betongs," PhD thesis, Technical University of Munich, Berlin, 1976.

[16] Tuutti, K., "Corrosion of steel in concrete," PhD thesis, Swedish Cement and Concrete Research Institute, Stockholm, 1982.

[17] Litvan, G. G. and Meyer, A., "Carbonation of Granulated Blast Furnace Slag Cement Concrete During Twenty Years of Field Exposure," American Concrete institue, special publication, Vol. 91, 1986.

[18] Parrott, L. J. and Killoh, D. C., "Carbonation in a 36 year old, in-situ concrete," Cement and Concrete Research, Vol. 19, No. 4, 1989, pp. 649-656.

[19] Campbell, D. H., Sturm, R. D. and Kosmatka, S. H., "Detecting Carbonation," Concrete Technology Today, Vol. 12, No. 1, 1991.
[20] Papadakis, V. G., Fardis, M. N. and Vayenas, C. G., "Hydration and carbonation of pozzolanic cements," ACI Materials Journal, Vol. 89, No. 89, 1992, pp. 119-130.
[21] Möller, J. S., "Measurement of carbonation in cement-based materials," PhD thesis, Chalmers University of Technology, Göteborg, 1994.
[22] Thiery, M., Villain, G., Dangla, P. and Platret, G., "Investigation of the carbonation front shape on cementitious materials: Effects of the chemical kinetics," Cement and Concrete Research, Vol. 37, 2007, pp. 1047-1058.
[23] Villain, G., Thiery, M. and Platret, G., "Measurement methods of carbonation profiles in concrete: Thermogravimetry, chemical analysis and gammadensimetry," Cement and Concrete Research, Vol. 37, No. 8, 2007, pp. 1182-1192.
[24] Castellote, M., Andrade, C., Turrillas, X., Campo, J. and Cuello, G. J., "Accelerated carbonation of cement pastes in situ monitored by neutron diffraction," Cement and Concrete Research, Vol. 38, No. 12, 2008, pp. 1365-1373.
[25] Castellote, M., Fernandez, L., Andrade, C. and Alonso, C., "Chemical changes and phase analysis of OPC pastes carbonated at different CO2 concentrations," Materials and Structures, Vol. 42, 2009, pp. 515-525.
[26] Herrera, R., Kinrade, S. D. and Catalan, L. J. J., "A Comparison of Methods for Determining Carbonation Depth in Fly Ash-Blended Cement Mortars," Materials Journal, Vol. 112, No. 2, 2015, pp. 287-294.
[27] Herterich, J., Black, L. and Richardson, I., "Microstructure and phase assemblage of low-clinker cements during early stages of carbonation," 14th International Congress on the Chemistry of Cement Beijing, 2015.
[28] Leemann, A., Nygaard, P., Kaufmann, J. and Loser, R., "Relation between carbonation resistance, mix design and exposure of mortar and concrete," Cement and Concrete Composites, Vol. 62, 2015, pp. 33-43.
[29] Wu, B. and Ye, G., "Comparative studies of carbonation fronts of cement paste blend with SCMs," 3rd International conference of service life design for infrastructures, Zhuhai, China, 2016.
[30] Shi, Z., Lothenbach, B., Geiker, M. R., Kaufmann, J., Leemann, A., Ferreiro, S. and Skibsted, J., "Experimental and thermodynamic modeling studies on carbonation of Portland cement - metakaolin - limestone mortars," To be submitted to: Cement and Concrete Research, In preparation.
[31] Snellings, R., "Chapter 4: X-Ray Powder Diffraction," in *A Practical Guide to Microstructural Analysis of Cementitious Materials*, Ed(s) K. Scrivener, R. Snellings and B. Lothenbach, CRC Press, Boca Raton, United States, 2015.
[32] Jakobsen, U. H., Personal comunication: "Carbonation characterization by optical microscopy," 2016.
[33] Jakobsen, U. H., Laugesen, P. and Thaulow, N., "Determination of Water-Cement Ratio in Hardened Concrete by Optical Fluorescence Microscopy," American Concrete institue, special publication, Vol. 191, 1999.
[34] Scrivener, K., Bazzoni, A., Gassó, B. M. and Rossen, J. E., "Chapter 8: Electron Microscopy," in *A Practical Guide to Microstructural Analysis of Cementitious Materials*, Ed(s) K. Scrivener, R. Snellings and B. Lothenbach, CRC Press, Boca Raton, United States, 2015.
[35] Berodier, E., Bizzozero, J. and Muller, A. C. A., "Chapter 9: Mercury Intrusion Porosimetry," in *A Practical Guide to Microstructural Analysis of Cementitious Materials*, Ed(s) K. Scrivener, R. Snellings and B. Lothenbach, CRC Press, Boca Raton, United States, 2015, pp. 419-444.

[36] Washburn, E. W., "Note on a method of determining the distribution of pore sizes in a porous material," the National Academy of Sciences of the USA, 1921, pp. 115-116.
[37] Skibsted, J., "Chapter 6: High-Resolution Solid-State Nuclear Magnetic Resonance Spectroscopy of Portland Cement-Based Systems," in *A Practical Guide to Microstructural Analysis of Cementitious Materials*, Ed(s) K. Scrivener, R. Snellings and B. Lothenbach, CRC Press, Boca Raton, United States, 2015.
[38] Galan, I., Andrade, C., Castellote, M., Rebolledo, N., Sanchez, J., Toro, L., Puente, I., Campo, J. and Fabelo, O., "Neutron diffraction for studying the influence of the relative humidity on the carbonation process of cement pastes," Journal of Physics: Conference Series, Vol. 325, 2011.
[39] EN 196-1:2005: Methods of testing cement – Part 1: Determination of strength, 2005.
[40] Belda, A., De Weerdt, K., Hornbostel, K. and Geiker, M., "Investigation of the effect of partial replacement of Portland cement by fly ash on carbonation using TGA and SEM-EDS," International RILEM Conference on Materials, Systems and Structures in Civil Engineering, Lyngby, Denmark, 2016.
[41] Matala, S., "Effects of carbonation on the pore structure of granulated blast furnace slag concrete," PhD thesis, Helsinki University of Technology, Espoo, 1995.
[42] Maage, M. and Smeplass, S., "Third Workshop: Service Life Design of Concrete Structures From Theory to Standardisation," DuraNet, Tromsø, 2001.
[43] Greve-Dierfeld, S. and Gehlen, C., "Performance based deemed-to-satisfy rules," The Fourth International fib-Congress 2014, Mumbai, 2014.